Simulation of the imaging and detection properties of the eROSITA experiment on Spectrum-X-Gamma

DIPLOMA THESIS

of

Christian Schmid

performed at the

Dr. Remeis-Sternwarte Bamberg

(Astronomical Institute of the University of Erlangen-Nuremberg)

Sternwartstraße 7, 96049 Bamberg

supervised by

Prof. Dr. Jörn Wilms

August 2008

The image on the title page displays the configuration of the eROSITA telescope (Predehl, 2008b).

Abstract

The **e**xtended **RO**entgen **S**urvey with an **I**maging **T**elescope **A**rray (eROSITA) project is the German contribution to the X-ray satellite Spectrum-X-Gamma. It consists of an imaging instrument built from 7 individual Wolter telescopes, where each of them has its own CCD detector. During its flight the data from the satellite will be monitored by a **N**ear **R**eal **T**ime data **A**nalysis (NRTA) software, which is developed at the Dr. Remeis-Sternwarte in Bamberg. The NRTA will detect hardware problems and scientificly interesting phenomena like transient X-ray sources right after the transmission of the observation data from the satellite to the ground station.

In order to be able to test the code of the NRTA software before the launch of the satellite, a simulation for the eROSITA telescope was developed in the course of this work. It uses realistic X-ray source distributions to generate X-ray photons with an adequate algorithm. The photon reflection by the mirror system and the subsequent detection with the CCD detector are implemented according to realistic models using, e.g., a simulated **P**oint **S**pread **F**unction (PSF) and a detector specific **R**edistribution **M**atrix **F**ile (RMF). Additional detector features like split events or pileup are also included. The final output of the simulation is an event list file with a format similar to the future output of the real telescope.

Event lists for different scenarios like transient objects or detector defects can be generated by the simulation and used as input for the NRTA. Therefore, the simulation is a powerful testing tool, that can still be extended with several additional features. It can be also used to study, e.g., the impact of the telescope motion during the all-sky survey on the measured data.

Contents

Chapter 1

Introduction

The eROSITA telescope is an X-ray telescope, which will scan the entire sky to obtain a comprehensive catalog of astronomical X-ray sources. In this context this chapter provides a short introduction to the scientific and technical background of X-ray astronomy.

1.1   X-ray astronomy

At the early stages of astronomy the universe was observed in optical light emitted from stars of reflected from planets or similar objects. In the 20th century the observation of additional wavelengths in the infrared or radio band and in the high energy domain of X-rays and γ-rays became technically possible. According to their physical background, particular regions of the universe might look very different in these energy ranges. Many new scientific results emerged from the new radiation detection methods (Carroll & Ostlie, 1996).

Observing the universe at very short wavelengths of X-rays and γ-rays, i.e., photon energies above 0.1 keV, makes it possible to investigate high energetic phenomena such as supernovae, black holes, **A**ctive **G**alactic **N**uclei (AGN) or galaxy clusters (Aschenbach et al. 1998, Charles & Seward 1995). In the case of the latter three kinds of objects a lot of mass is concentrated in a finite volume, which results in a very strong gravitational potential. This potential has enough power to heat the surrounding matter up to X-ray temperatures. The emerging radiation typically has very short wavelengths. Additionally the K-shell transition of most chemical elements also lies in the range of X-ray energies (Dmitriev et al., 2005). As these transitions usually produce strong lines, they can be observed quite well even over large distances and provide information about the emitting material.

A big disadvantage of visible light is its absorption by dust and gas clouds in the universe. In contrary the very short and the very long wavelengths can penetrate these obscuring clouds (Dmitriev et al., 2005). Due to this property they can provide very deep insight into the universe. Therefore, the research in global properties of the universe, like cosmological investigations or the search for dark matter, can gather information from X-ray observations.

Among the current astronomical issues particularly the quest for dark matter is a popular scientific goal. In this field of interest the mass distribution in the universe and several cosmological constants play an important role. Many astronomers hope to find out more about these unknown quantities by investigating large-scale cosmological objects like galaxy clusters, which create diffuse X-ray radiation. Therefore, one of the destinations of many current X-ray missions are surveys of clusters and super-clusters (Squires et al. 1996, MPE, et al. 2007, Dmitriev et al. 2005).

Apart from the diffuse light emitted by galaxy clusters there are many different compact ob-

jects generating short wavelength radiation. The most popular among them are X-ray binaries consisting of a compact object, like a neutron star or a black hole, and a companion star "feeding" the compact object (Carroll & Ostlie 1996, Charles & Seward 1995). Usually the companion fills its Roche-lobe, i.e., it is extended to such a degree, that matter can be transferred to the compact object. As the latter one has a very deep gravitational potential, a lot of energy is released by this process. In fact mass accretion is the most efficient physical energy creation processes (Wilms, 2002). The accretion of matter with mass m onto a black hole with the Schwarzschild radius

$$R_S = \frac{2GM}{c^2} \tag{1.1}$$

releases an energy up to

$$\Delta E_{acc} = \frac{GMm}{R_S} = \frac{1}{2}mc^2 \tag{1.2}$$

i.e., theoretically about 50% of the rest mass can be released as energy. Of course, there has to be some radiation production mechanism, otherwise ΔE_{acc} would be transformed into kinetic energy without any X-ray emission. According to a closer mathematical analysis the fraction of released energy depends on the rotation of the compact object. For a maximum rotating black hole it can be up to 40% of the rest mass. In comparison to that the fusion of hydrogen to helium only has an efficiency of 0.7% (Wilms, 2002).

A further X-ray emitting phenomenon are AGN (Wilms, 2006). These are high-mass black holes in the center of galaxies, which accrete matter of up to several solar masses per year. Due to angular momentum conservation the matter forms an accretion disk instead of directly falling onto the black hole. According to the current scientific models a very hot corona envelopes the accretion disk. The gas atoms in the corona perform inverse compton scattering with the photons emitted from the disk, i.e., they transfer energy to the photons. This mechanism creates a power law spectrum of X-ray photons.

Compact objects with accretion disks are usually located at very large distances from the Earth, so they can be observed as point like X-ray sources in contrary to galaxy clusters, which are extended sources with diffuse emission. Previous X-ray surveys (see Sec. 1.3) have shown, that the major part of the **C**osmic **X**-**R**ay **B**ackground (CXRB), which was observed by the first X-ray missions as diffuse X-ray radiation originating from all directions of the sky (Giacconi et al., 1962), can be resolved into discrete sources. Most of them have been identified as AGN (Brandt & Hasinger, 2005). It is supposed that a comprehensive survey of AGN can reveal new information about the evolution of the universe.

1.2 X-ray telescopes

It turns out that the atmosphere of the Earth is quasi-opaque for high energetic electromagnetic radiation in the energy domain of X-rays and γ-rays (Aschenbach et al. 1998, Carroll & Ostlie 1996, Charles & Seward 1995), as shown in Fig. 1.2. Although this fact is quite advantageous for the health of any living creatures on this planet, it complicates the observation of the corresponding astronomical sources with ground based instruments.

The only way to detect X-ray light from the ground is to measure its interaction with molecules in the upper parts of the atmosphere. The Cherenkov light produced by these processes can, e.g., be observed by the **M**ajor **A**tmospheric **G**amma-Ray **I**maging **C**erenkov (MAGIC) telescope on La Palma, Canarian Islands (Petry & The MAGIC Telescope Collaboration, 1999). Another well-known telescope built for this particular part of astronomical science is the **H**igh **E**nergy **S**tereoscopic **S**ystem (H.E.S.S.) in Namibia (Bernlöhr et al., 2003). But the observation
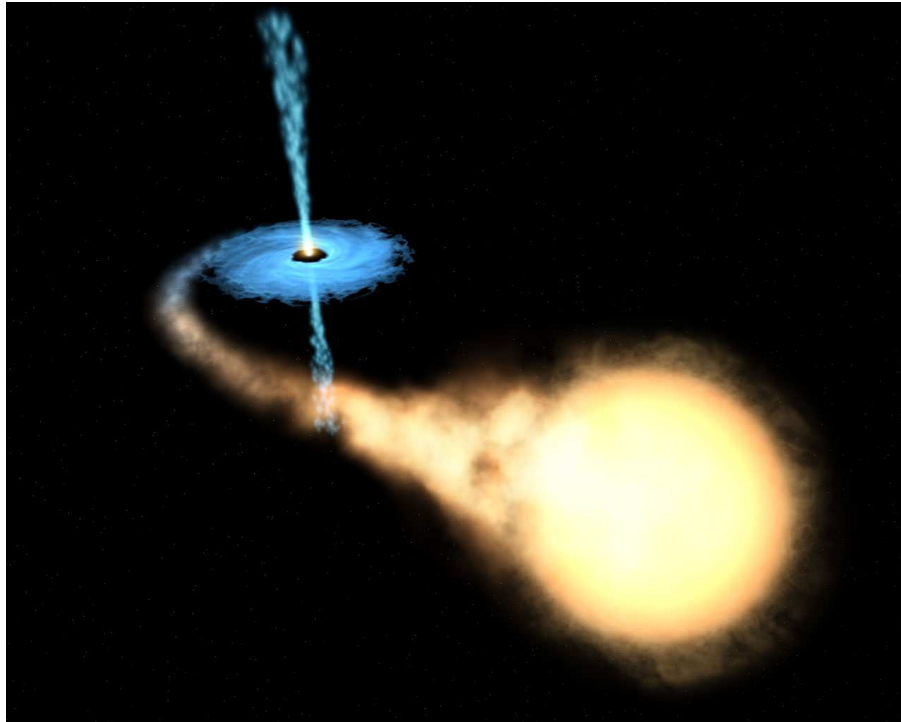
Figure 1.1: Microquasar accreting matter from a companion star: due to angular momentum conservation the matter is not falling on the compact object in a straight line, but forms an accretion disk (artist's view, *http://www.spacetelescope.org*).

of Cherenkov light is only applicable for very high photon energies of the order of several GeV, i.e., in the domain of hard γ-rays.

In order to avoid atmospheric absorption, during the early stages of X-ray astronomy detectors were mounted on rockets and launched a few hundred kilometers into the upper atmospheric layers. Of course, due to the quite short flights only snapshot measurements were possible with this method. For long term observations, most X-ray experiments are performed on satellites today with a more or less static orbit around the Earth.

Apart from the atmospheric absorption a further problem in high energy astronomy is the fact that X-rays and γ-rays cannot be focused by conventional optical methods such as lenses or mirrors. Due to their quasi-constant index of refraction in most materials they simply penetrate the lens or mirror without being deflected. Therefore, it is quite difficult to build an imaging telescope for this high energetic radiation.

Basically there are two common methods used for X-ray telescopes on satellites (cf. Wilms 2008). The first possibility, which is also realized for eROSITA, are the so-called *Wolter telescopes* proposed by Wolter (1952). They are based on the total reflection of X-ray photons on a metal surface like gold under a very small angle of incidence. In order to obtain an adequate light collecting area the imaging system is built from several mirror shells assembled inside of each other. The individual mirror shells actually are a combination of a paraboloid and a hyperboloid focussing the light, which originates from a particular point source, onto a spot in the focal plane.

Each mirror shell has a particular weight, so the number of individual mirrors cannot be too large, as the entire telescope still has to be launched into space. To achieve good optical performance, the quality of the mirrors has to fullfill high standards, which complicates the manufacturing. Additionally the focal length of a Wolter telescope tends to be of the order of several meters, whereas the space available on satellites is very limited.
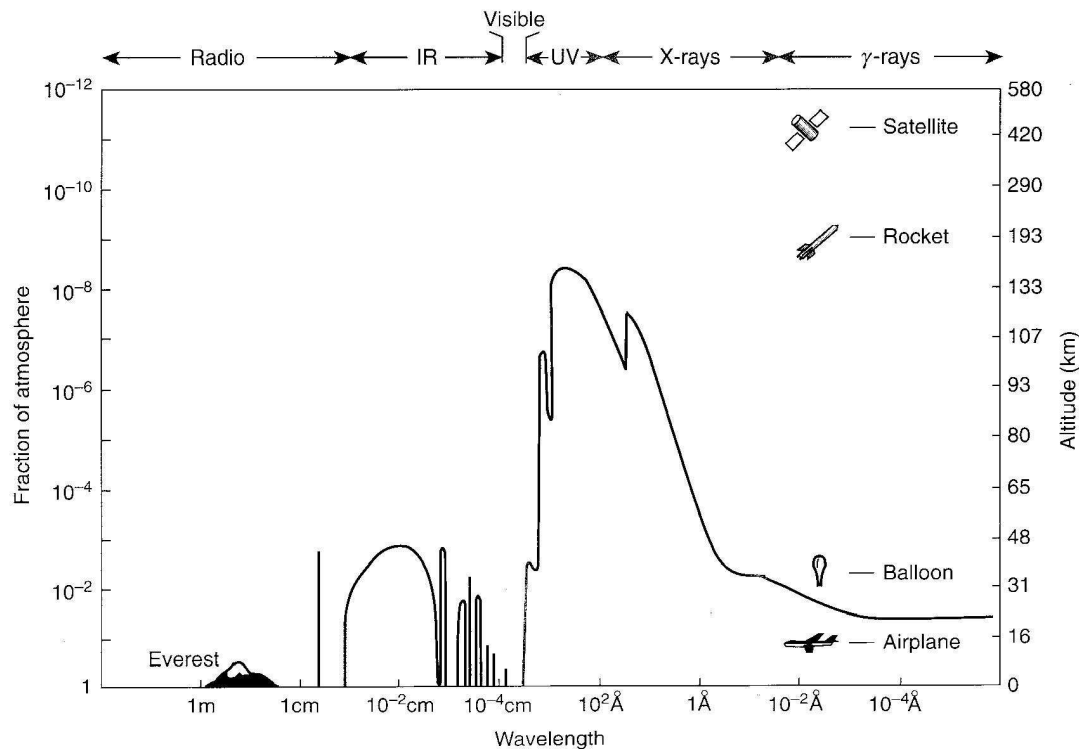
Figure 1.2: Absorption of radiation by the atmosphere: the line indicates the height in the atmosphere at which half of the cosmic electromagnetic radiation is absorbed. For visible light the atmosphere is transparent, whereas X-rays and γ-rays are almost completely absorbed (Charles & Seward, 1995).

Apart from telescope weight and dimension problems Wolter telescopes are only applicable for quite low photon energies of up to about 10 keV, because higher energetic photons would require very long focal lengths of more than 10 m. Therefore appropriate telescopes are difficult to be mounted on satellites. Additionally the **F**ield **O**f **V**iew (FOV) of a Wolter telescope is usually quite narrow, of the order of only a few degrees. All in all Wolter telescopes represent a possible and common technique to build an imaging system for soft and intermediate X-rays, but the production of the necessary optics is quite challenging.

The second approach to determine the direction of an X-ray source is to put a mask with a particular pattern of transparent and opaque pixels in front of a CCD detector, measure the resulting shadow pattern, and obtain the direction of the incident photons from the shift of the shadow pattern on the detector with respect to the mask pattern, as indicated in Fig. 1.4. From the mathematical point of view the shadow is the result of the convolution of the source function with the mask function, thus the position of the sources can be determined from the measured image data by applying adequate mathematical deconvolution methods, which is, e.g., explained in Groeneveld (1999).

These so-called *Coded-Mask telescopes* are capable of higher photon energies than Wolter telescopes and usually have a very wide FOV of up to $\sim$ 15°. They also do not bring along the problems of long focal lengths, but their angular resolution is worse. As this kind of telescopes is based on a completely different imaging technology than the Wolter technique, which is used for eROSITA, there will be no further information given in this text. For more details about
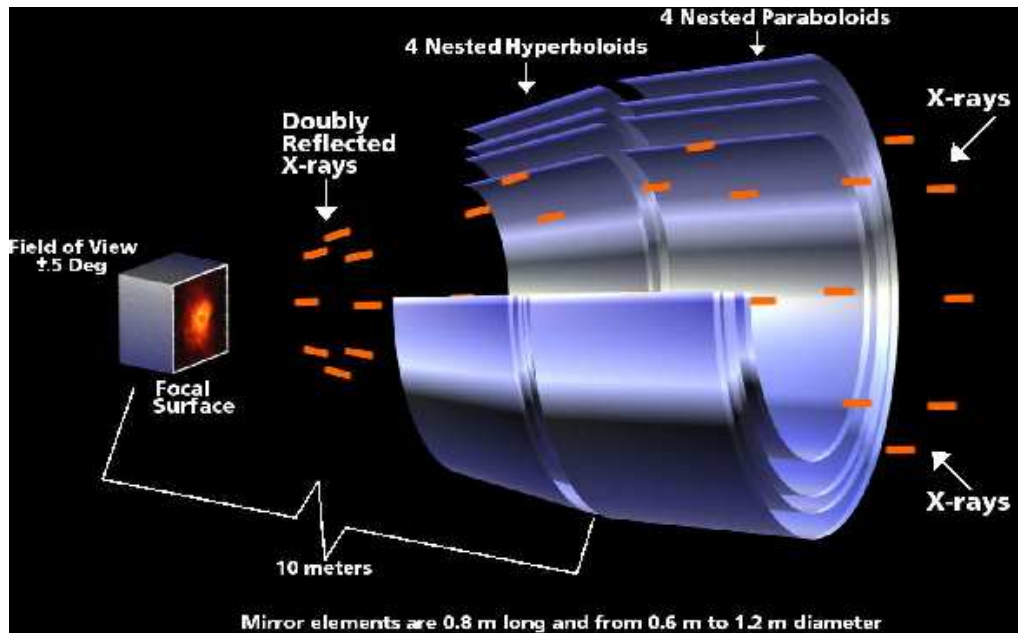
Figure 1.3: Focussing of X-rays under grazing incidence in a Wolter telescope by double reflection on a paraboloid and a hyperboloid (numbers for Chandra observatory, image from NASA/CXC/SAO, *http://chandra.harvard.edu/*).

Coded-Mask telescopes see, e.g., Groeneveld (1999).

Imaging instruments for soft or medium radiation energies are usually operated with CCD detectors. In comparison to other X-ray radiation detectors like proportional counters they have a very good spatial and temporal resolution. Apart from the optical quality of the mirror system the detector resolution has the biggest influence on the telescope resolution. Therefore, CCDs are much more convenient for imaging telescopes than proportional counters (Fiorucci et al., 1990).

In terms of the energy resolution CCDs exhibit no disadvantages in comparison to other detectors. For eROSITA, with a **F**ull **W**idth at **H**alf **M**aximum (FWHM) of 140 eV at 5.9 keV, the resolution is even up to $\Delta E / E \approx 2.4\%$ (Meidinger, 2008). The quantum efficiency of this detector is very good with values of $\geq 90\%$ for the photon energy range from 0.3 keV to 11 keV.

The main disadvantage of CCD detectors are their temperature requirements. Usually they have to be cooled down to $\sim -100°C$, so a complex cooling system is necessary to provide the required temperatures. For eROSITA the operating temperature of $-80°C$ is achieved by a combination of variable-conductance heat pipes and two radiators. The temperature is kept stable by a *latent cold storage unit* (Fürmetz, 2007), which is based on a chemical substance with melting temperature close to $-80°C$. The substance is in equilibrium with a frozen and a liquid phase, so variations in thermal energy are absorbed by the latent heat at the phase transition.

Although the energy resources on satellites are usually quite limited, the cooling problem can be solved by adequate methods. Due to the advantages of their good spatial and energy resolution, and due to their small size most X-ray instruments for the soft and intermediate energy range, including eROSITA, use CCDs for radiation detection.

1.3 X-ray missions

The first astronomical X-ray experiments had to be mounted on rockets or balloons in order to be launched into the upper parts of the atmosphere for avoiding the absorption of the radiation by the
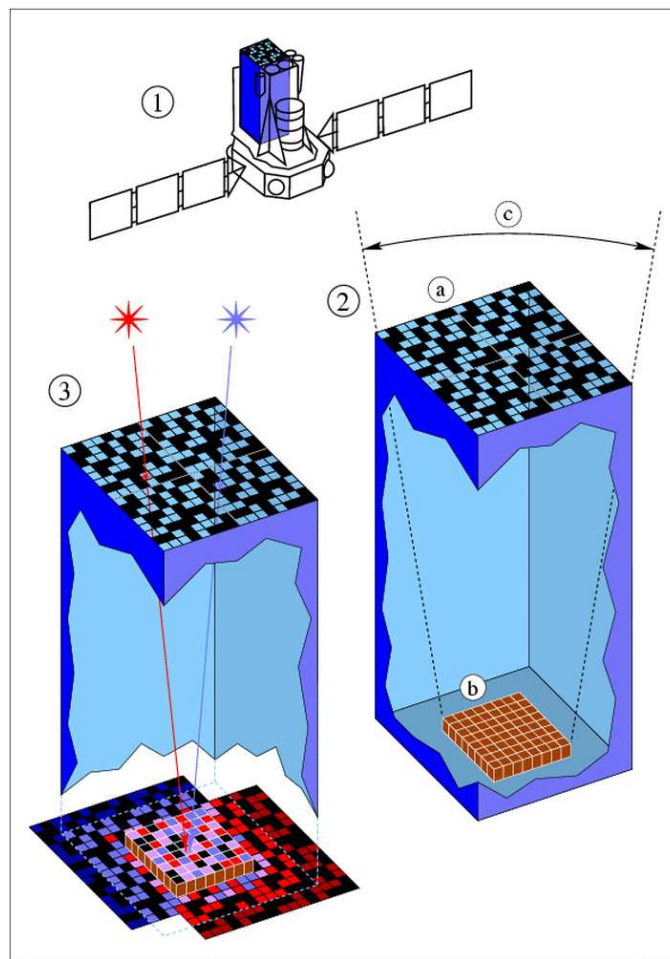
Figure 1.4: Technique of Coded-Mask telescopes (ISDC/Univ. Geneva, *http://isdc.unige.ch/Outreach/Data/ibis.gif*): the incident X-ray photons are partly absorbed by a mask with a particular pattern resulting in a shadow pattern on the CCD detector. The direction of the X-ray source can be reconstructed from the shift of the shadow pattern with respect to the mask.

atmosphere (Wilms 2008, Charles & Seward 1995). Their initial goals were the observation of X-rays emitted by the Sun. During a rocket flight aimed to detect fluorescent radiation from the Moon, a bright galactic X-ray binary and the CXRB were discovered by Giacconi et al. (1962). Later missions revealed a high degree of isotropy in the CXRB, which resulted in the suggestion that the corresponding sources have to be extragalactic (Brandt & Hasinger, 2005).

One of the milestones in X-ray astronomy was the satellite **RO**entgen **SAT**ellite (ROSAT) launched to a 580 km orbit in 1990. The primary destination of this experiment, which is based on a Wolter telescope, was an all-sky survey in the soft energy range from 0.1 keV to 2.4 keV to obtain an X-ray source catalog for the entire sky. During its survey the satellite discovered 105 924 sources in total (Voges et al., 2000). ROSAT was able to resolve 75% of the CXRB into discrete sources with limiting fluxes down to $\sim 10^{-15}$ erg cm^{-2} s^{-1}, where most of them have been identified as AGN with a sky density of $\sim 780 - 870$ deg^2 (Brandt & Hasinger, 2005). It is commonly supposed that almost the entire CXRB is created by emission from discrete sources, but in order to verify this statement more sensitive observations have to be performed.

According to observations of the spectrum of the CXRB, which has a maximum at about

$30 - 40$ keV (Marshall et al. 1980, Brandt & Hasinger 2005, MPE, et al. 2007), most AGN must be heavily obscured by gas and dust in the center of the galaxies. Therefore it is important to observe the universe in the intermediate and hard X-ray regime, as high energetic photons above 2 keV can penetrate these clouds.

The three satellites ESA's **X**-ray **M**ulti-**M**irror Mission **Newton** (XMM-Newton) (Jansen et al., 2001), NASA's *Chandra* (Weisskopf et al., 2000), both launched in 1999, and JAXA's *Suzaku* (Mitsuda et al., 2007), launched in 2005, are the currently most important X-ray telescopes. They can perform observations in the intermediate energy range of ≤ 10 keV and have focal lengths of the order of 7.5 m, 10 m, and 4.75 m respectively. Opposite to ROSAT they are designed for pointed observations of particular small sections of the sky. One of the most common surveys is the *Chandra Deep Field-North*, a 2.0 Ms exposure in a region with low intra-galactic absorption. Although XMM-Newton and *Chandra* are quite suitable for deep pointed observations, their instrumental layout is not adequate for wide field surveys, which are necessary to perform statistics of X-ray sources.

In order to provide a larger sample of sources for statistical examinations the ROSAT catalog should be enlarged by the later ABRIXAS mission (cf. MPE, et al. 2007). Unfortunately this satellite lost its main battery immediately after its launch in 1999 due to an error in the technical design, and therefore could never be operated in scientific mode. The successive mission ROSITA was proposed in 2002 as a module on the ISS, but further investigations revealed that the contamination in the direct neighborhood of the space station is too high for this kind of telescope. In April 2003 a proposal for the mission **D**ark **U**niverse **O**bservatory (DUO) was submitted to the NASA, but after initial selection for a phase A study, the final implementation was rejected for financial reasons. Despite of this setback, the technology of the DUO CCDs developed during the analysis study, can be used for the current eROSITA detectors.

Chapter 2

eROSITA

Basically eROSITA is a successor to ROSAT in terms of performing an all-sky survey in the X-ray regime. This chapter provides a short overview of the eROSITA mission.

2.1 Mission design

The eROSITA mission consists of an X-ray telescope for photon energies in the range from 0.5 keV to 10 keV. It is developed under the control of the **M**ax-**P**lanck-Institut für **E**xtraterrestrische **P**hysik (MPE) in Garching in cooperation with the **I**nstitute for **A**stronomy and **A**strophysics **T**übingen (IAAT), the **A**strophysical **I**nstitute **P**otsdam (AIP), the Sternwarte Hamburg, and the Dr. Remeis-Sternwarte Bamberg (Astronomical Institute of the University of Erlangen-Nuremberg), and represents the German contribution to the Russian scientific satellite Spectrum-X-Gamma (Predehl et al. 2006, Predehl et al. 2007).

2.1.1 Targets

In the first years of its flight eROSITA will perform an all-sky survey of the X-ray sky in the low and intermediate energy band from 0.5 keV to 10 keV. By this observation, the source catalog obtained from the survey of the earlier ROSAT mission, will be extended to the intermediate energy band. As the radiation of most X-ray sources is absorbed by gas and dust in the galaxies, these obscured sources can only be observed at very short wavelengths. Therefore the extension of the ROSAT soft-energy survey to the eROSITA survey is an important aspect of this mission.

Additionally the sensitivity of eROSITA is at least 10 times higher than the sensitivity of the earlier ROSAT mission (see Fig. 2.1). Therefore, a large number of new sources will probably be found in the course of this survey. According to estimates (MPE, et al., 2007) the eROSITA survey will discover up to 3.2 million AGN in the energy band from 0.5 – 2 keV and about 100 000 galaxy clusters. In comparison to the 105 924 sources in the RASS-FSC this will be a much larger sample for statistical investigations. Especially from the number of galaxy clusters, astronomers hope to gather information about dark matter and important cosmological constants.

The eROSITA telescope is the successor to ABRIXAS, which failed due to technical problems in space, ROSITA, which abandoned because the environment of the space station proved inadequate for X-ray astronomical experiments, and DUO, which was rejected by NASA for financial reasons following a successful phase A study. Although all of these forerunners were not successful, technical know-how from the development and engineering of the instruments can be reused for the construction of eROSITA. For example, the inner 27 mirror shells are the same as in the ABRIXAS telescope, so the mandrels built by Carl Zeiss, can be replicated easily. The detector chips result from the further development of the XMM-Newton and DUO CDD detectors,
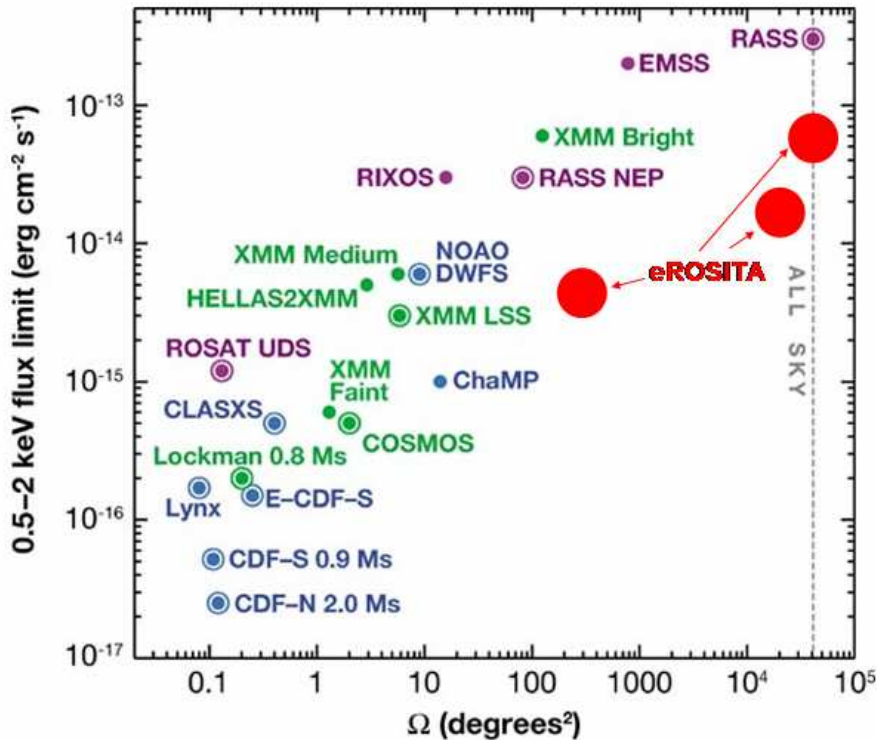
Figure 2.1: Comparison of several X-ray missions with respect to their flux limit and observed solid angle (Dmitriev et al., 2005). Like ROSAT the eROSITA mission will perform an all-sky survey. But the achieved sensitivity will be much better. Besides the all-sky survey some additional observations of smaller sections of the sky are planned for eROSITA.

thus a considerable amount of money and time can be conserved, in comparison to a completely new design.

2.1.2 Spectrum-X-Gamma

The Russian satellite Spectrum-X-Gamma provided by the Russian space agency Roscosmos, is a platform for several X-ray and γ-ray measurement devices (Predehl et al. 2006, Predehl et al. 2007, Dmitriev et al. 2005). Among them eROSITA is the major scientific instrument. In the initial design of the satellite further X-ray devices have been designated, namely the wide field X-ray monitor *Lobster* as contribution from the UK, the Russian coded-mask telescopes *ART*, and the international collaboration *SXC*. The arrangement of the several instruments on the satellite platform is displayed in Fig. 2.2. According to the current status, some of these instruments, like, e.g., Lobster, may have been taken out of the mission.

As on the one hand eROSITA is the biggest instrument on the satellite and on the other hand the simulation of its measurement process is in the focus of this diploma thesis, the satellite itself might sometimes also be referred to as eROSITA in this text. But of course this is actually only the name of the particular telescope as a part of the Spectrum-X-Gamma mission.

The launch of Spectrum-X-Gamma was originally planned to be at the end of 2011 from Baikonur or Kourou (MPE, et al., 2007). As possible launchers several types of the Russian Soyuz rocket are taken into account (Dmitriev et al., 2005). The subsequent transfer to its orbit will be performed using a FREGAT payload assist module. The orbital parameters of the initially
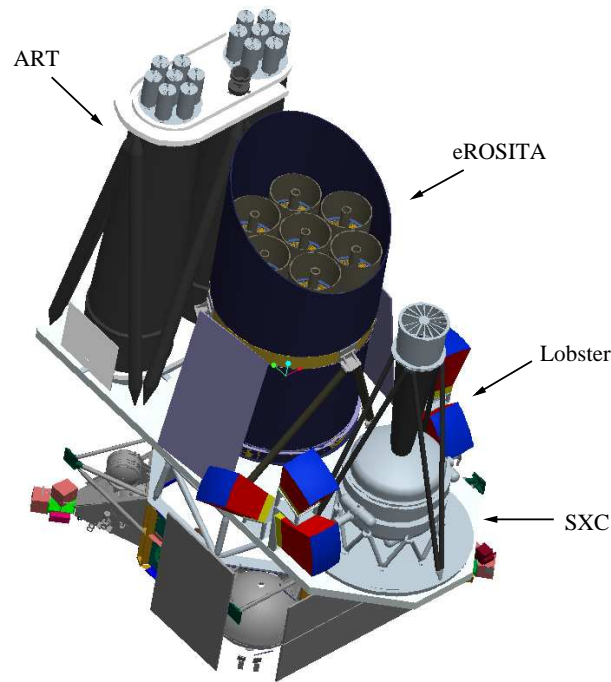
Figure 2.2: Satellite layout of Spectrum-X-Gamma according to Predehl (2008b). eROSITA is the major instrument on the satellite.

Table 2.1: Orbital parameters of the Spectrum-X-Gamma satellite according to Dmitriev et al. (2005).

altitude	600 km
inclination	29°
orbital period	96 min
maximum shadow duration	35 min

intended operation orbit of Spectrum-X-Gamma are listed in table 2.1.2.

2.1.3 Survey geometry

The FOV of the eROSITA telescope has a diameter of 61.9′ (MPE, et al., 2007). In order to perform the intended all-sky survey, the satellite has to scan the sky in individual strips. Afterwards the measured data from these bands can be combined to obtain an all-sky map. Due to several restrictions on the telescope pointing direction, like, e.g., forbidden regions around the Sun, the Earth or the Moon, and additional scientific aspects the survey geometry has to be designed in detail.

According to the original mission definition, the satellite will have a circular orbit in an altitude of 600 km and with an inclination of $i = 29°$. For this low orbit the gravitational potentials of the Sun, the Moon or other planets apart from the Earth can be neglected. Due to the oblateness of the Earth, the orbital plane will be precesssing around the Earth's rotational axis, i.e., the right ascension of the satellite's ascending node is not fixed in time. This aspect of orbit perturbations is analyzed in Sec. 5.2.7. According to Eq. (5.72) the change of the right ascension of the ascending
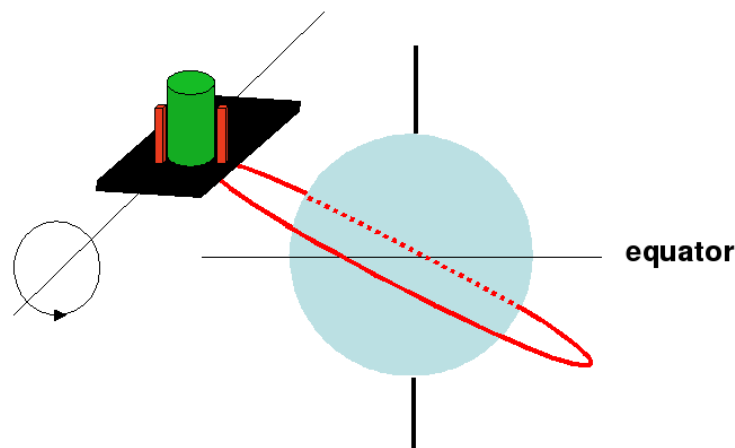
Figure 2.3: Rotation of the satellite around its scan axis during one orbit revolution (Fürmetz & Friedrich, 2008).

node is of the order of

$$\left(\frac{d\Omega}{dt}\right)_2 \approx -6.3° \text{ day}^{-1} \tag{2.1}$$

i.e., the orbital plane is precessing around 360° in about 57 days, and the orbit precession can be used in order to scan the entire sky in strips intersecting at the survey poles.

Additionally to its motion around the Earth the satellite has to rotate around its intrinsic scan axis, as displayed in Fig. 2.3. This rotation has to be performed in such a way that the telescope pointing axis is moving along the scan strips. During one orbit revolution the satellite in principle performs a complete rotation around the scan axis.

The telescope should not point directly into the Sun, the Earth or the Moon (see Fig. 2.4), as these bright X-ray sources would destroy the CCD detectors. This requirement results in several restrictions on the pointing geometry. In fact the prohibited regions around these objects are even larger than the objects themselves in order to prevent stray light from falling on the detector. According to Fürmetz & Friedrich (2008) the telescope pointing axis may only point into directions, that are at least 16° away from the Earth's horizon.

Additional requirements on the satellite's attitude emerge from the need for power supplied by the solar panels and the demands of the cooling system. The solar panels must have a particular solar aspect angle in order to provide the necessary electrical power, whereas the cooling system has to guarantee the CCD detectors' operation temperature of −80°C and, therefore, has to get rid of the redundant thermal energy. The latter can only be released by the radiators if they point into a region of the sky, which contains no close and warm objects like, e.g., the Earth or the Sun. An extensive study of the eROSITA's thermal budget has been performed by Fürmetz (2007).

Considering all these requirements on the satellite's attitude, an inversion of the scan rotation is necessary in time intervals of about 30 days (Fürmetz & Friedrich, 2008). The scan geometry for the entire sky is therefore not as simple as in the previously mentioned naive approach of the neighboring strips, which is only valid for short intervals. In fact the inversion period also depends on the actual season.

As a consequence of the survey geometry the observational exposure of the telescope is longer at the survey poles, i.e., at both intersection points of the scan strips. In these regions the detection probability for very faint sources is much higher than in the remaining sky. In order to take an advantage of this particular property, the survey poles will be located in a region of special
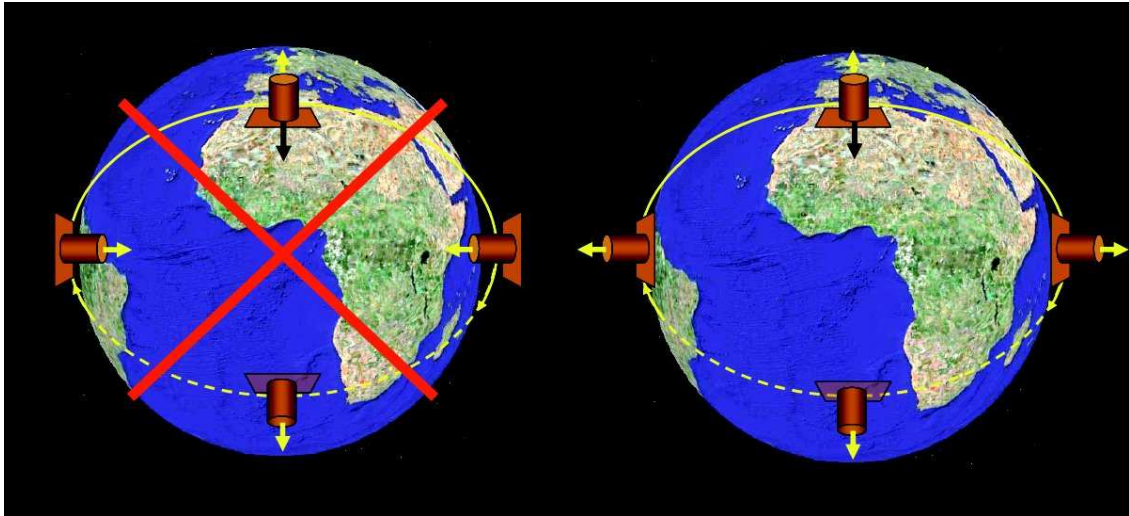
Figure 2.4: Restrictions on the scan direction with scan axis perpendicular to the orbit plane: the left scenario if forbidden, because the telescope would look directly onto the Earth (Fürmetz, 2007).

scientific interest.

It was decided to set up eROSITA's survey geometry in such a way that the survey poles lie in the neighborhood of the galactic poles, because this region has the lowest absorption by galactic dust and therefore guarantees a deep glance into the universe (Predehl et al. 2006, Predehl et al. 2007). Within the galactic plane the X-ray absorption is so high, that a deep exposure at the ecliptic poles, which lie in this region, would be wasteful. It is not possible to put the survey poles directly at the galactic poles due to orbit and attitude restrictions like, e.g., the need for power supply by the solar panels and the prohibition of pointing in the direction of the Sun (Fürmetz, 2007). For this reason the compromise displayed in Fig. 2.5 was chosen for the mission. In this scenario the survey poles are 30° away from the galactic poles, but this is still quite suitable to obtain deep insight into the universe.

2.2   Telescope

The X-ray telescope eROSITA consists of seven individual and parallel aligned sub-telescopes of type Wolter-I, i.e., each mirror shell is a combination of a paraboloid with a hyperboloid (Wolter, 1952). The mirrors are coated with gold and focus the incident high energy photons onto a CCD detector, where they create a charge cloud, which can finally be measured.

2.2.1   Layout

The seven telescope subsystems are identical and aligned in parallel direction, and can therefore be used individually. Each mirror system has its own detector in contrary to the former ABRIXAS mission, where one detector CCD was located at the common focus of the seven slightly tilted mirror systems. In the eROSITA configuration, due to this redundancy concept, if one or several telescopes fail, the remaining can be operated without modifications.

The basic configuration of eROSITA with the seven sub-telescopes is shown in Fig. 2.6. Of course, apart from the mirror system and the CCD detectors there are many additional items in the telescope structure. The most important can be found in the following list.
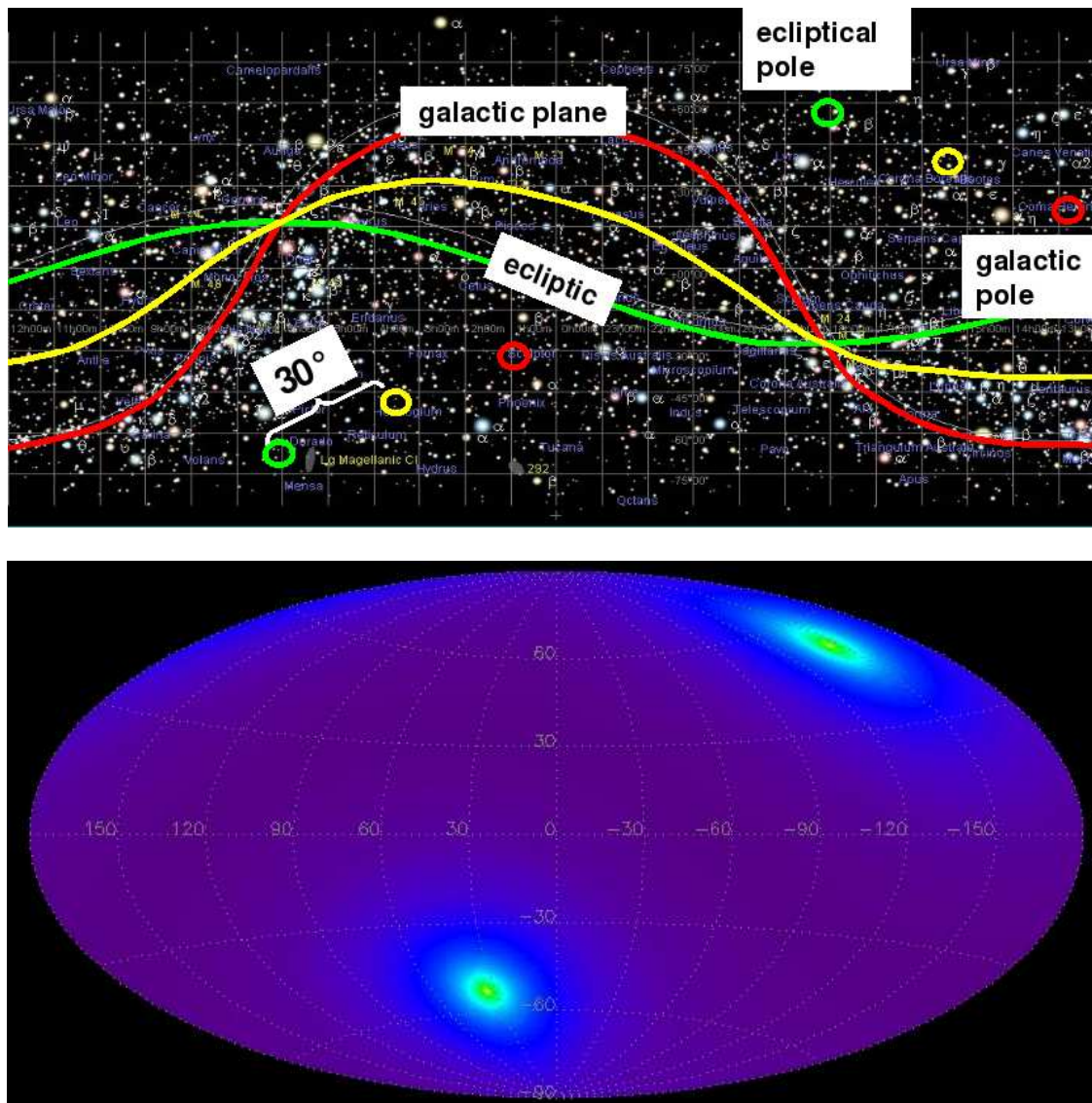
Figure 2.5: The survey poles of the eROSITA all-sky survey are tilted with respect to the ecliptic plane in order to achieve more exposure time at regions close to the galactic poles, as there is lower absorption (adapted from Fürmetz & Friedrich 2008). The yellow line in the upper sketch represents the scan equator of the eROSITA survey, and the two yellow circles are the survey poles. In the lower sketch the two bright spots indicate the higher exposure at the survey poles.

- **Optical bench:** All elements of the telescope have to be installed on the optical bench, in order to have fixed distances between the mirrors and detectors. The corresponding structure has a hexagonal shape and is connected to the satellite via a hexapod, which guarantees the necessary protection against deformations.

- **Electronic boxes:** The detector and measurement processing electronics for each sub-telescope are contained in an individual box.

- **Cooling system:** To provide the $-80°$C for operating the CCD detectors, a complex cooling system with variable-conductance heatpipes, two radiators, and a stabilizing buffer, based on the latent heat at the phase transition of a particular chemical substance, is mounted at the bottom of the optical bench.

- **Sun shield and mirror baffles:** A big sun shield and 600 mm long baffles in front of the individual mirror systems prevent optical and X-ray stray light from falling on the detector.

- **Contamination shield:** The way between the mirror systems and the detectors is surrounded by a tube to avoid contamination of the detector.

- **Telescope cover:** To prevent contamination during the transport and satellite launch, the telescope has a cover, which is opened in space by the force of two springs.

- **Star trackers:** The pointing direction of the telescope in orbit is determined from the position of well-know stars, which are observed in optical light.

In the following the main items of the telescope, which are important for the simulation, are described in detail.

2.2.2 Mirror system

The telescope consists of 7 Wolter-I telescopes (Wolter, 1952), each having 54 mirrors and its own CCD detector (Predehl et al. 2007, Dmitriev et al. 2005). The mirrors are assembled inside of each other and integrated in a spider wheel as shown in Fig. 2.7, where the largest shells have a diameter of 360 mm. The focal length of the mirror system is 1 600 mm.

The individual eROSITA mirror systems are designed in a similar way as in the former ABRIXAS mission, where each sub-telescope consisted of 27 mirror shells. For eROSITA 27 additional shells with larger diameters have been added, in order to have a larger photon collecting area with twice as many shells. The chart in Fig. 2.8 shows that the effective area of eROSITA is much higher than the effective area of ROSAT and even that of XMM-Newton in the energy range from $0.2 - 2.5$ keV, thus the telescope should be able to detect additional and so far unknown faint sources in the specified range of low and intermediate photon energies.

Of course, the mirrors have to be manufactured very precisely, and the alignment of the different shells on the wheel spider is also a challenging task. The thickness of the mirror shells lies in the range from 0.2 mm to 0.4 mm, and the entire mirror system has a length of 300 mm. The mirror production for eROSITA is performed by the companies *MediaLario* and *Carl Zeiss* (Predehl et al., 2007). The latter have already produced the mirror shells for the ABRIXAS mission, and therefore have the necessary know-how for the mirror manufacturing.

The mandrels from ABRIXAS are still available and can be reused for the inner 27 shells of eROSITA, which means a considerable reduction of the production costs. A mandrel is a negative form of a mirror shell, which consists, e.g., of nickel. During the mirror production the mandrel is evaporated first with gold, to create the reflection layer, and afterwards with nickel, to create the supporting structure. After the evaporation, the shell is released from the mandrel and finally polished, to achieve best optical performance. The entire technique is very challenging and takes up to the order of months for a single mirror shell. By this complicated method it is possible to manufacture such large mirrors with the required accuracy.

The mirror integration into the wheel spider and the optical quality of the individual shells both have a large effect on the performance of the telescope. All deviations from the perfect alignment might result in a degradation of the PSF (see Sec. 4.2.4). The total angular resolution of the telescope, i.e., considering mirror and detector deviations, should be of the order of $< 15''$ at a photon energy of 1 keV (Predehl et al. 2007, Dmitriev et al. 2005). Therefore many effort is needed for the manufacturing of the optical system.

Figure 2.6: Configuration of eROSITA. Left: mirror systems and pn-CCD detectors surrounded by Cu proton shields. Right: final telescope configuration with Sun shield, mirror baffles, telescope tube, heat radiators etc. (Predehl, 2008b).

2.2.3 Detectors

The eROSITA detectors are composed of backside illuminated pn-CCDs and are basically designed according to the concept of the XMM-Newton **E**uropean **P**hoton **I**maging **C**amera (EPIC) pn CCD (Strüder et al., 2001) and the ABRIXAS detector respectively (Dmitriev et al. 2005, Predehl 2008a, Meidinger et al. 2007, Meidinger 2008). The specified energy band of the telescope ranges from 0.5 keV up to 10 keV with a quite good energy resolution. At the MPE there have already been some tests with the DUO CCD, which has similar properties as the eROSITA detector. The FWHM at the energy 5.9 keV is 140 eV (Meidinger et al., 2007). The quantum efficiency of the detector is $\geq$ 90% in the operational energy range, as presented in Fig. 2.9.
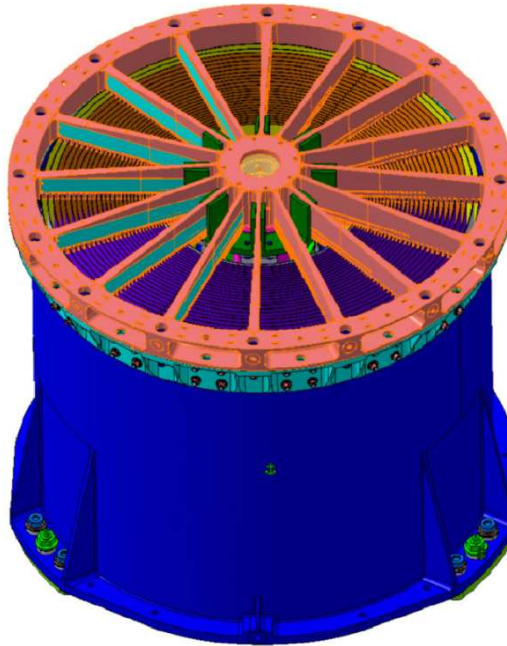
Figure 2.7: Mirror system of eROSITA consisting of 54 shells nested inside of each other and mounted in a wheel spider (Friedrich, 2008).

Each of the 7 frame store pn-CCD detectors is located in the focal plane of the mirror system and has 384×384 pixels, a size of $28.8 \times 28.8 \, \text{mm}^2$, and a $450 \, \mu\text{m}$ thick sensitive layer, i.e., each pixel has a width of about $75 \, \mu\text{m}$ (Meidinger, 2008). Because of the quite small pixel size, the fraction of split events (see Sec. 4.2.5) cannot be neglected. The entire detector array covers the FOV, which has a diameter of $61.9' \approx 1°$, so each detector pixel corresponds to $\sim 10''$ (MPE, et al., 2007).

The pn-CCD detector is operated at $-80°$C, whereas the detector housing, which basically consists of a copper proton shield, has a temperature of $\sim 20°$C. Therefore, the detector cooling and the telescope's thermal budget is quite challenging. Detailed information about the thermal concept can be found in Fürmetz (2007).

The detectors are frame store CCDs, i.e., the charge created by photons is collected in the detector pixels during an integration time of $50 \, \text{ms}$. At the end of this period the entire charge is moved out of the pixel array to a separate storage within a very short time of $200 \, \mu\text{s}$ (Meidinger et al., 2007). Then the actual readout process is performed on the frame store area by the three CAMEX chips, where each of them has 128 signal processing channels. Due to that technique the pixel array is quasi immediately available again for measuring incoming photons, while the collected charges are read out from the frame store. Using this technique only a few photons get lost, if they hit the detector during the time span of the charge transfer to the frame store. The total fraction of the out of time events is estimated to be of the order of $\sim 0.4 \, \%$ (Meidinger, 2008). With an integration time of $50 \, \text{ms}$ the camera takes 20 frames per second.

Due to the finite size of the detector pixels of $75 \, \mu\text{m}$ and an assumed charge cloud size of the order of some μm, the charge cloud created by a single photon event might be partitioned among several neighboring pixels, resulting in a particular fraction of split events in the measured data (cf. Sec. 4.2.5). For larger CCD pixels this fraction would be smaller or could even be neglected, but for the specified eROSITA detector it is necessary to perform a split analysis on the measured data.
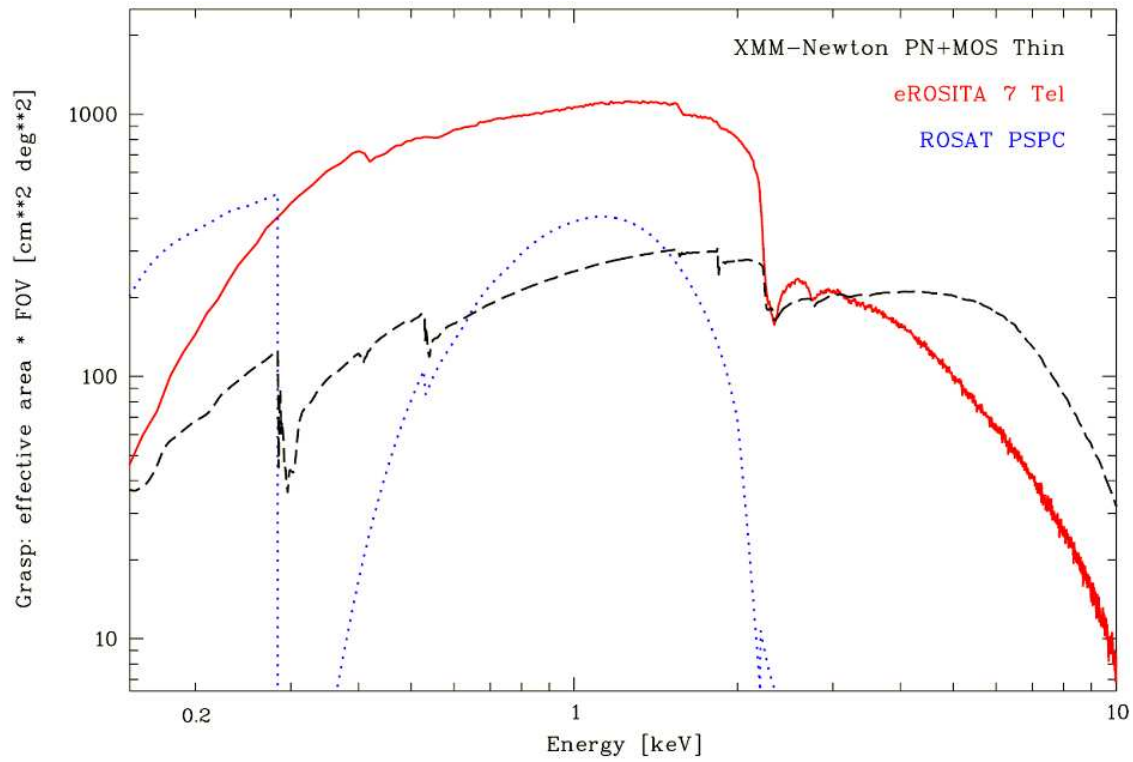
Figure 2.8: Effective area of eROSITA in comparison to ROSAT and XMM-Newton (Hasinger, 2008): the effective area of eROSITA will be much larger than for ROSAT. In the low energy range it will even exceed the effective area of XMM-Newton.

2.2.4 Technical data

To provide a quick overview, the most important technical data of the eROSITA telescope are summarized in table 2.2.4.
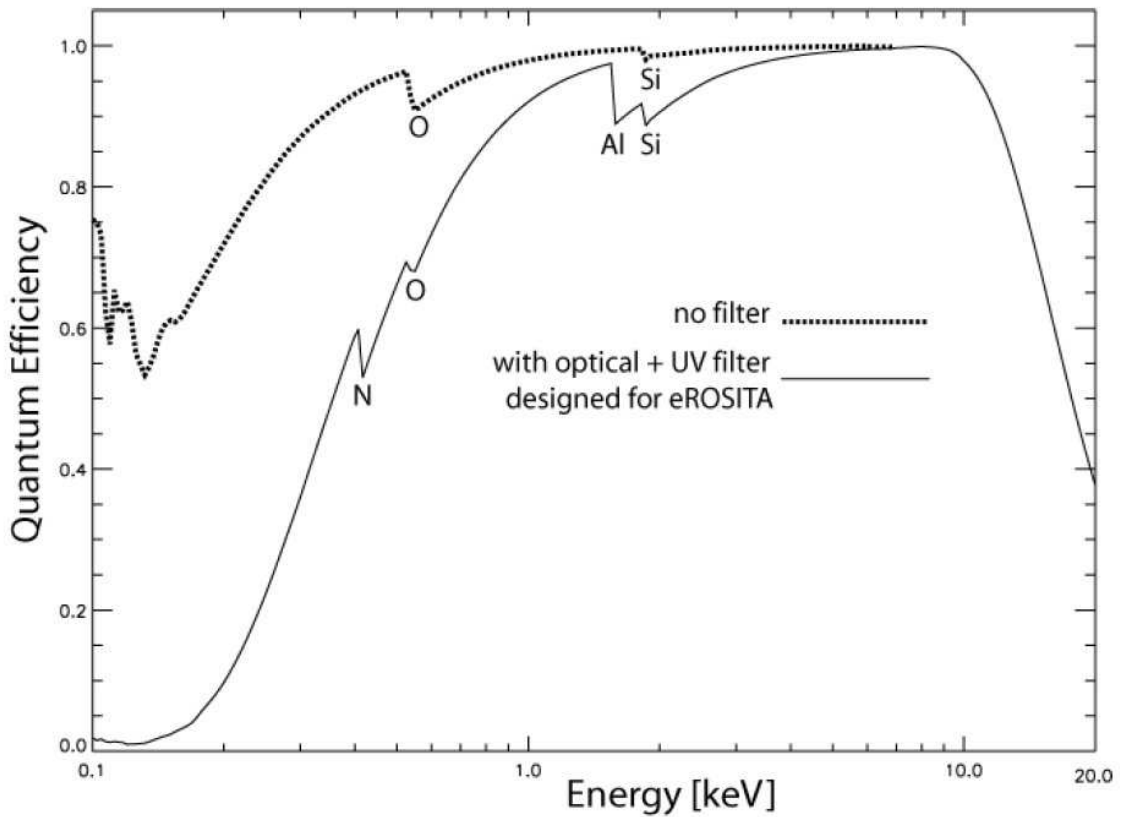
Figure 2.9: Quantum efficiency of the eROSITA CCD according to Meidinger (2008). Without any filter the efficiency is ≥ 90% in the specified energy range of the telescope.

Table 2.2: Technical specifications of the eROSITA telescope according to Dmitriev et al. (2005), Predehl et al. (2007), Friedrich (2008), Meidinger (2008).

mirror	7 Wolter-I optics with 54 shells each
mirror diameter	358 mm
mirror length	300 mm
mirror material	nickel
mirror coating	gold
FOV diameter	61.9′
focal length	1.600 mm
angular resolution	< 15″
detector	pn-CCD (384×384 pixels)
detector size	$19.2 \times 19.2 \, \text{mm}^2$
energy range	$0.5 - 10 \, \text{keV}$
energy resolution	140 eV at 5.9 keV
readout mode	frame store
integration time	50 ms
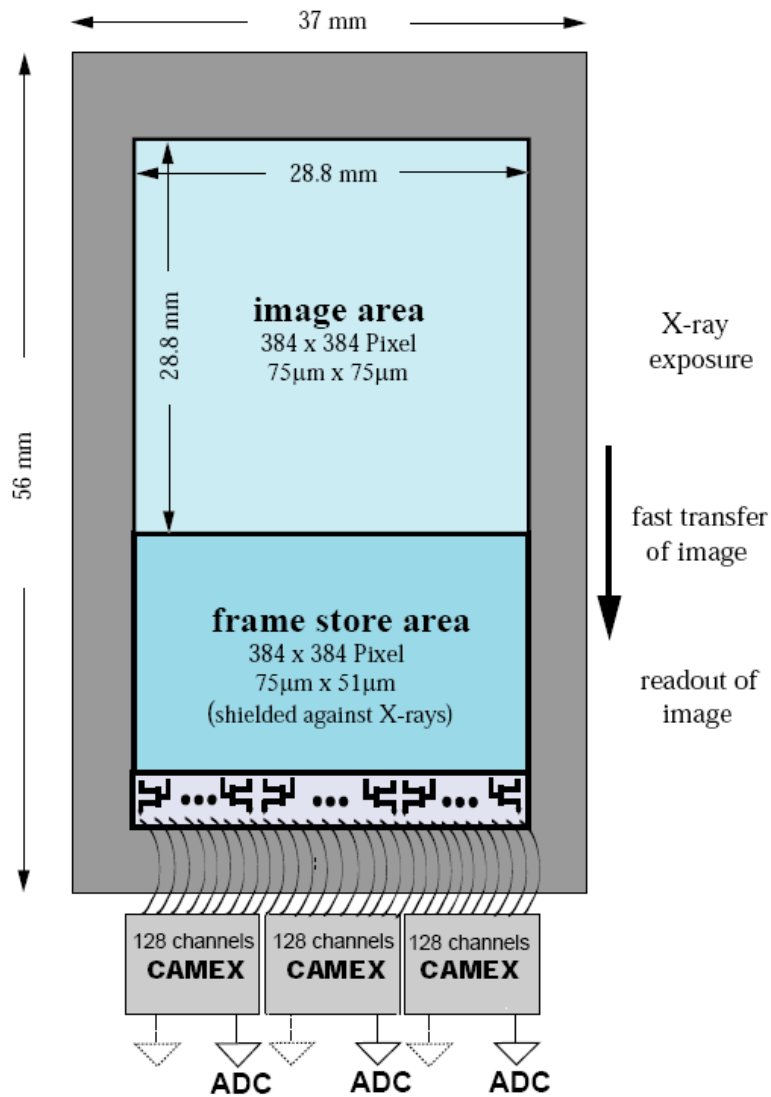
Figure 2.10: Frame store pn-CCD concept for eROSITA (Meidinger, 2008): the charges in the semiconductor material, which are created by the incident photons, are stored in the CCD pixels until the end of the current integration period (50 ms). Then all charges are shifted to the frame store area within a very short time of several μs, so the image area is ready again for the detection of further photon events. During the integration time the charges from the previous frame, which are now in the frame store, are read out by 3 CAMEX chips.

Chapter 3

Software

This chapter describes context of the software implementation of the eROSITA simulation package. The program code follows the current standards in order to guarantee portability and compatibility of the simulation.

3.1 Near Real Time Analysis

An important aspect of the eROSITA mission, which is mainly developed at the Dr. Remeis-Sternwarte in Bamberg, is the setup of the NRTA of the measured data. During the all-sky survey, this particular software especially searches for hardware problems, like bad pixels, and for transient objects, like γ-ray bursts, in the observed event lists. This analysis is performed quite soon after the download of the data from the satellite to the ground station. On the one hand, by this method problems with the telescope can be detected in time and the integrity of the scientific data is guaranteed. On the other hand, short-term objects can be noticed almost immediately after their first observation (cf. Wilms & Kreykenbohm 2008). Then, in case of scientific interest, it might be possible to take a closer look at them using different X-ray telescopes, which are more convenient for pointed observations.

The NRTA is developed as a part of the **S**cience **A**nalysis **S**oftware **S**ystem (SASS) and is implemented in collaboration with teams at the MPE and the AIP. The NRTA software itself is written in Bamberg, especially by Dr. Ingo Kreykenbohm. In order to test the implemented algorithms, the measurement process of eROSITA has to be simulated, as real data will not be available before the satellite's launch. The goal of this diploma thesis is the design of a realistic simulation of the telescope measurement process. The generated event lists can be used as direct input to the NRTA pipeline instead of the real satellite data.

3.2 HEAsoft and file formats

The **H**igh **E**nergy **A**stronomy **s**oftware (HEAsoft) suite provided by NASA consists mainly of the following three parts:

- **XANADU:** scientific analysis software like XSPEC.

- **FTOOLS:** library of several programs for operations on **F**lexible **I**mage **T**ransport **S**ystem (FITS) files (see Sec. 3.2.2) providing a common user interface.

- **HEAdas:** FITS operation programs with same interface as FTOOLS, but newer and build around a different core.

The simulation developed in the course of this work is designed according to the standards of **H**igh **E**nergy **A**stronomy **d**ata **a**nalysis **s**ystem (HEAdas) (Arnaud, 2008) in order to provide an intuitive user interface and common code layout. According to these standards, the entire software for the simulation is written in ANSI C. With this choice a maximum of portability and compatibility to other software packages is guaranteed.

The code layout of HEAsoft programs follows particular standards, e.g., concerning the parameter input via **P**arameter **I**nterface **L**ibrary (PIL) (Sec. 3.2.1) or the error handling strategy. In order to produce a portable and readable code, the simulation program was designed similar to original HEAsoft tools. One aspect, which was not retained, is the handling strategy for runtime errors using *goto* commands, which should be avoided in higher-level applications (Dijkstra, 1968). The critical statements are surrounded by a loop instead, which is run only once. In case of an error the loop can be interupted with a *break* command. This way of code implementation is considered to be much better structured and more stable than the solution using *goto*.

The HEAsoft suite provides different libraries to implement a user interface, file access, or random number generation. The most important items used in the simulation are listed in the following.

3.2.1 PIL

As pointed out above, the entire simulation consists of several sub-programs. Each of them has its own set of input parameters like filenames of input and output files, orbital elements, time parameters, or telescope configuration data. For example, the width of the FOV can be set manually to different values in order to keep the entire simulation portable to other telescope setups.

There are different possible ways to obtain the program parameters at start up: they could be read from the command line at each program call or be stored in a file. The **P**arameter **I**nterface **L**ibrary (PIL), developed by the ISDC, is a powerful tool to handle program parameters. It provides a flexible mixture of different parameter input methods from a file or from the command line.

The required or optional parameters are defined by the programmer in a central file, setting the format of the parameters, the possible range, and default values. The user can either set the specified parameters as command line arguments at the program call, or the PIL will ask for the necessary values during runtime. For each parameter it is possible to use the value from the previous program call, which is stored as default. There is also a possibility to define optional parameters, which are set to their default value, if the user does not explicitly enter another value.

All in all the PIL provides a simple interface to read required and optional parameters from within a C-program. The format and range of the individual parameters is automatically checked. For filename parameters it is even possible to constrain the input to existing files. Using the PIL, the programmer does not have to care about the way, how the parameters are actually entered by the user.

Because of its simple handling the PIL is commonly integrated in many high energy astronomy software packages. The FTOOLS and HEAtools use this library to read their program parameters. Therefore, the PIL is also used in all elementary parts of this simulation, in order to provide a common user and developer interface.

Detailed information about the PIL, the C programmers user interface, and the required format for parameter files is given in the PIL user's manual (Borkowski, 2002).

3.2.2 FITS

The **F**lexible **I**mage **T**ransport **S**ystem (FITS) defined by NASA and IAU is a common file format to store different kinds of scientific data in high energy astronomy. Most software packages like
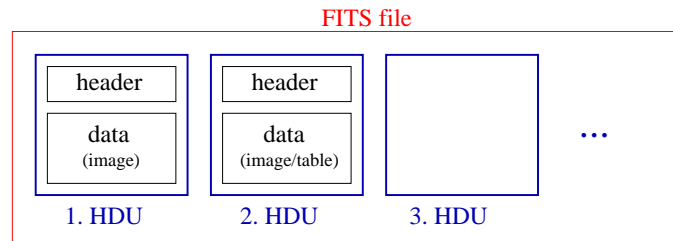
Figure 3.1: Schematic layout of FITS file containing several HDUs.

FTOOLS and HEAdas work with this file format. As a consequence almost all data sets in high energy astronomy are stored in FITS files.

A FITS file consists of one or more HDUs, where each of them represents either an image or an ASCII or binary table, except from the primary **H**eader and **D**ata **U**nit (HDU), which in any case contains a (possibly) empty image (see Fig. 3.1). The header provides the structure of the data set and important information about the origin of the data. The name of the telescope, hardware settings, or the time of the observation are encoded in standardized header keywords. Usually there are also comments about the data format or a history of previously applied software tools stored in the headers. Therefore, header information is essential to process and interpret the scientific data stored in the data unit.

There are several restrictions on the number of bytes for the headers as well as a list of required header keywords. This detailed information will not be listed in this context, but can be found in the FITS definition Hanisch et al. (2001).

Additionally there are several standard layouts for common types of FITS files containing, e.g., event lists or spectra. The simulation software is designed according to these standards in order to guarantee compatibility to other software packages.

3.2.3 CFITSIO

The CFITSIO is a library containing routines for easy read and write access to FITS files from C or Fortran programs. It allows the programmer to access FITS files by calling the relevant routines without caring about the actual file format specifications. Because of its simple handling the CFITSIO library is the standard FITS file interface used in HEAdas. The manuals for C (HEASARC, 2007) and Fortran programmers are available at the **H**igh **E**nergy **A**strophysics **S**cience **A**rchive **R**esearch **C**enter (HEASARC) website (*http://heasarc.nasa.gov/fitsio/fitsio.html*).

As the simulation software is developed according to the HEAsoft standards, the different data for input and output is mainly stored in the FITS format using the routines of the CFITSIO library.

3.3 Simulation program

All programs of the simulation package are written in ANSI C according to the HEAdas standards (Sec. 3.2). The main part among the individual programs is the actual simulation software *measurement*, which basically performs the following tasks:

- scanning process of the telescope over the celestial sphere

- generation of photons for the individual sources from the specified source models

- imaging and measurement of the photons according to the telescope model
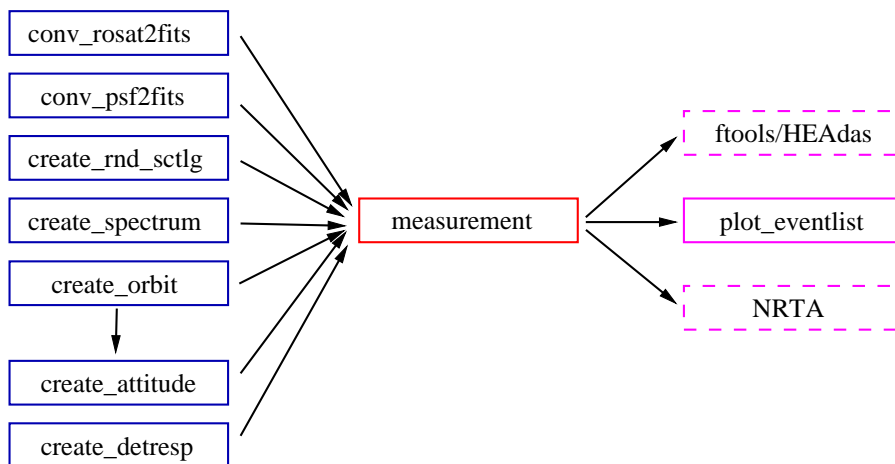
Figure 3.2: Cooperation of the individual sub-programs of the simulation software package: the tools on the left side generate the necessary input data for the measurement simulation. Of course, some of these tasks can also be perform by different software packages. Particularly the orbit and attitude files or the source spectra may originate from a different source. The event list resulting from the simulation can be evaluated with the programs on the right side of the sketch, including programs from the simulation package, some FTOOLS or HEAdas software, and the NRTA software.

An overview of the relevant sub-programs of the simulation software package is given in Fig. 3.2.

3.3.1 Input data

The simulation program *measurement* needs several kinds of input data, such as the orbit and attitude information or the source catalogs and source spectra, to perform the actual measurement. These data partly have to be converted from the respective file formats to an adequate format for the simulation, partly it is actually created by sub-programs. The simulation software package contains several tools to manage the input data for the simulation:

- **conv_rosat2fits:** This tool converts the RASS-FSC (Sec. 4.1.1) from the published ASCII file format to a FITS file, which can be read by the simulation software *measurement*.

- **conv_psf2fits:** The PSF data generated by Peter Friedrich's simulation of the eROSITA mirror system are available in several ASCII files containing lists of photon events (see Sec. 4.2.4). These files have to be converted to FITS files with the information about the PSF, i.e., the photon reflection probabilities for specific energies and off-axis angles.

- **create_rnd_sctlg:** Additionally to the ROSAT data the simulation uses a large set of faint sources, which are randomly distributed on the celestial sphere with a particular flux distribution (Sec. 4.1.2). The generation of this catalog is performed by this application.

- **create_spectrum:** The simulation requires a spectrum for the individual sources in the source catalog. The spectra can be either created by professional spectral analysis software like XSPEC or by this tool of the software package.

- **create_orbit:** At the moment, when this simulation was developed, the eROSITA mission was at such an early stage of development that no proper orbit files for the satellite were available. Therefore, realistic orbits actually had to be calculated in order to be able to

perform the simulation. As pointed out in Chap. 5, the exact calculation of the satellite's orbit is quite challenging, if higher order perturbation terms are included. This part of the simulation is separated and handled by a sub-program that produces orbit files in FITS format, containing the position and velocity of the satellite at particular time intervals.

- **create_attitude:** Additionally to the orbit data the simulation also needs the satellite's attitude information in order to determine the viewing direction of the telescope. As these data were also not available at this early stage in mission development, a simple algorithm was written to create attitude files based on the assumption that the satellite looks straight away from the center of the Earth. In that case the telescope axis is equivalent to the line connecting the center of the Earth with the satellite. This condition fixes two of the three attitude angles. The third angle is determined according to the condition that the solar panels should collect as much sunlight as possible and are aligned in an appropriate direction.

- **create_detresp:** This tool creates a detector response matrix that can be used in order to test the simulation.

As this simulation was developed some years before the launch of eROSITA, some parameters and important satellite or telescope data such as orbit files were not available. Therefore, the necessary data had to be created as realistically as possible in order to obtain sensible results from the simulation.

3.3.2 Measurement simulation

With the basic input data, which are created by the previously mentioned tools, the main program *measurement* can be run to simulate the satellite's actual flight and measurement process. The output is an event list of the measured photons, containing the time, when the photon was detected, the detector pixel, and the **P**ulse **H**eight **A**mplitude (PHA) value of each individual photon. The quantity PHA is a measure for the electronic signal in the detector and is given in detector specific PHA channels. As the simulation also creates split events (Sec. 4.2.5), a single photon might result in several event list entries with correspondingly lower PHA values.

3.3.3 Analysis tools

One of the main targets of the simulation is the generation of a realistic event list as input data for the NRTA software. Apart from that it is also useful to be able to analyze the output data in order to verify the simulation. Therefore, there are also some tools to evaluate the event list FITS file and to create human readable or visualized data from the simulation output. The *plot_eventlist* tool, e.g., creates images of the detector array from the individual photon events. Each image contains all measured events during one integration period. The output format are *png* image files.

3.3.4 Testing facilities

Apart from the actual simulation software there are several additional tools for testing and verifying the data generated by the former tools. The main programs in this context are:

- **plot_psf:** This is a tool to visualize the PSF that is used for the simulation.

- **test_light curve:** Creates light curves from **P**ower **S**pectral **D**ensity (PSD)s according to the algorithm described in Sec. 4.2.2.

- **test_tle_output:** Implements access to NORAD **T**wo **L**ine **E**lement (TLE) data (Sec. 4.3.7).

- **test_distrndsources:** Verifies the proper distribution of the random source catalog, which is created to simulate faint sources and the CXRB (Sec. 4.1.2).

Chapter 4

Simulation

This chapter provides detailed information about the main simulation parts starting with the generation and handling of source catalogs and describing the implementation of the measurement simulation. The calculation of the satellite's orbit is treated separately in Chap. 5, as the simulation does not require this particular program, but could also use orbit and attitude data from a different source.

The simulation is a contribution to the development of the NRTA, which is written in the X-ray group of the Dr. Remeis-Sternwarte in Bamberg. The NRTA on the one hand observes the integrity of the detector during the satellite's flight, i.e., it checks the incoming data for failed pixels or other technical problems. By this way the current status of the telescope and, therefore, of the measured data can be guaranteed. On the other hand the NRTA software is checking the observation data during the all-sky survey for evidence of transient objects like γ-ray bursts.

As the satellite will not be launched until 2011, there will be no real scientific data measured on orbit available in the next few years. The NRTA should be working without problems from the beginning of the satellite's mission, so it has to be completed and tested in advance. In order to try out different measurement scenarios during the development of the code, there has to be a source of realistic observation data as input for the corresponding NRTA tools. Therefore, this simulation is implemented under the aspect of performing a realistic measurement of X-ray photons, which originate from different sources and are observed according to the intended scanning process. The resulting event files follow the format of the actual measurement data.

As the simulation works with flexible source and detector input data, it can be easily adapted to create appropriate test data for the NRTA. It is possible to set a detector pixel to producing physically unreasonable output. With correct implementation the NRTA should be able to detect this pixel failure. In order to check the recognition algorithm for transient objects, a bright new source could be added to the existing source catalog. In this way event lists for the different relevant scenarios for the NRTA can be generated by the simulation.

In order to guarantee realistic observation output, the simulation is implemented according to the actual measurement procedure of the satellite. The satellite is moving on a proper orbit with the telescope axis pointing right away from the center of the Earth. The mirror system is modelled according to simulated PSF data and the simulation of the CCD detector follows the currently known technical data. Due to the high flexibility of the simulation at later steps in the development of eROSITA new data like, e.g., a more precise model of the PSF or RMF, can be inserted easily.
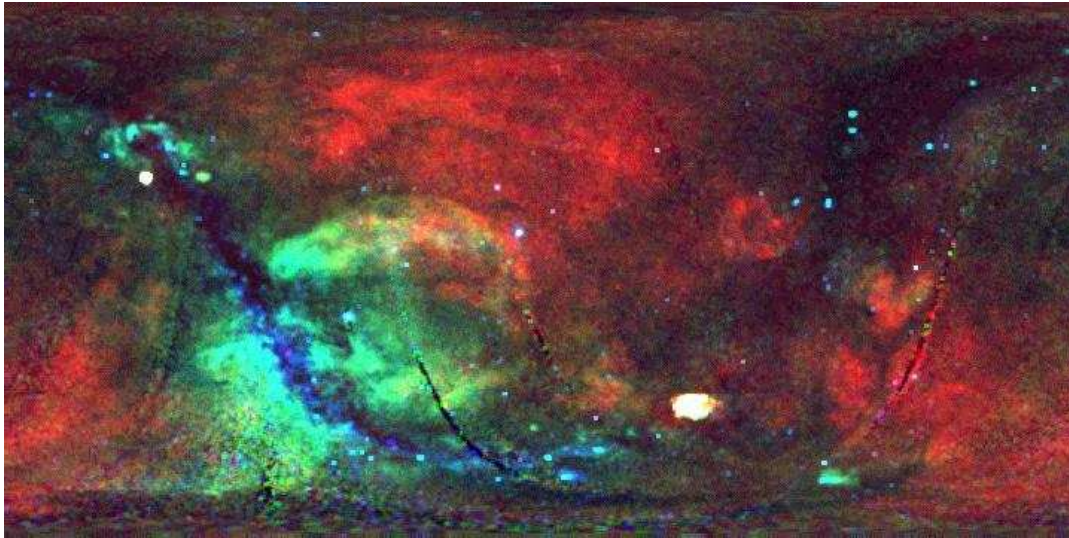
Figure 4.1: Color-coded image of the ROSAT All-Sky Survey (*red* for low, *green* for intermediate, and *blue* for high X-ray energies. The blue line represents the galactic plane with some bright spots, which are mainly caused by X-ray binaries. There are also dark absorption clouds visible close to the galactic center in the left part of the picture.
(*http://www.xray.mpe.mpg.de/cgi-bin/rosat/rosat-survey*).

4.1 Source catalogs

In order to obtain a realistic distribution of astronomical X-ray sources in the sky, two different source catalogs were chosen as input for the simulation. On the one hand the **F**aint **S**ource **C**atalog (FSC) of the ROSAT all-sky survey is taken as a basic set of already known sources. But as eROSITA is implemented to detected much more sources than ROSAT with fainter source fluxes, an additional number of weak sources is used for the simulation.

According to Brandt & Hasinger (2005) most X-ray sources detected so far are AGN, i.e., point sources. In the current version the simulation deals only with point sources, as it is quite challenging to develop physically realistic models for extended sources like galaxy clusters. This will be done at a later development step of the simulation.

4.1.1 ROSAT All-Sky Survey

In order to provide realistic sources for the simulation program, the FSC from the **R**OSAT **A**ll-**S**ky **S**urvey (RASS) (performed in 1990) was chosen as input. This catalog is available for download as ASCII file on the website of the MPE (Voges et al., 2000). It consists of 105 924 sources observed in the energy band from 0.1 to 2.4 keV. A visualization of the RASS is displayed in Fig. 4.1.

Using the RASS-FSC as input makes it possible to test the simulation on the actual X-ray sky. All sources contained in this source catalog should be detectable by eROSITA. In order to make the RASS-FSC usable for the simulation program, the ASCII file containing the source data has to be converted to FITS format (Sec. 3.2.2). This conversion is performed by the software tool *conv_rosat2fits*, which was developed in the course of this diploma thesis.

4.1.2   Random sources

The eROSITA mission as a further all-sky survey is developed to be more sensitive than ROSAT and to observe the X-ray sky at higher photon energies, in order to discover additional, so far unknown sources. Therefore, it is not sufficient to use the RASS-FSC as input for the eROSITA simulation, as this contains only sources brighter than the ROSAT flux limit. An additional source catalog is created with sources distributed randomly over the celestial sphere according to a physically meaningful energy flux distribution. This algorithm is particularly used to complete the RASS-FSC with very faint sources below the ROSAT threshold.

According to earlier X-ray surveys and especially deep extragalactic observations with *Chandra* and XMM-Newton summarized in Brandt & Hasinger (2005) the integrated number counts of sources vs. the source energy flux (i.e., the number of sources with a flux $> S$ is plotted vs. S) exhibit a power law shape with a particular slope depending on the observed energy band and on the brightness of the sources, as shown in Fig. 4.2. Actually the source distribution can be described by two power laws with $\alpha_f \approx -0.5$ for faint sources and $\alpha_b \approx -1.6$ for bright sources. The break flux is about $10^{-14}\,\mathrm{erg\,cm^{-2}\,s^{-1}}$ and $10^{-15}\,\mathrm{erg\,cm^{-2}\,s^{-1}}$ for the low and high energy band respectively.

As the universe is assumed to be isotropic, the source distribution will probably be the same in the remaining sky as in the examined deep fields, apart from some statistical fluctuations. This particular shape of the source flux distribution can be taken as basis to create additional sources for the measurement simulation, similar to the approach for the Simbol-X simulator described in Puccetti et al. (2008).

In order to obtain a similar power law source flux distribution as observed in the deep fields, a Monte Carlo algorithm, applicable for non-uniformly distributed random numbers (Deák 1990, p. 68ff., Gould et al. 2006, p. 429ff.), was used to create source fluxes according to a proper power law index α extending the faint end of the RASS-FSC. The resulting integrated source distribution for a sample of 100 000 sources and a power law index $\alpha = -0.5$ is shown in Fig. 4.3 and matches the observed distribution for faint sources in Fig. 4.2.

An additional Monte Carlo algorithm was used to distribute the created sources on the celestial sphere, assuming isotropy in the large-scale X-ray universe. As shown in Fig. 4.4 for a sample with 10 000 sources, the algorithm works quite well, since there is no obvious bias in the spatial source distribution.

As deep X-ray surveys have resolved the main part of the CXRB into discrete sources (Brandt & Hasinger, 2005), the random distribution of a sufficient number of very faint sources should be suitable to simulate this kind of background radiation. The random source catalog completes the RASS-FSC with very faint sources to obtain a realistic X-ray sky, which can be used as a sample for the simulation program. Apart from the random source catalog with faint sources, no further model was used for the CXRB at the current stage of the simulation development.

4.2   Measurement process

The simulation is designed according to the real measurement process of the telescope. A sketch of the main steps in the simulation of the all-sky survey is given in Fig. 4.5. On the execution of the code mainly these tasks are performed in a loop over the requested period.

The main part of the measurement process is the creation and procession of individual photons. Fig. 4.6 displays the photon processing routine, which is applied to each individual photon, and the detector readout. Detailed information about the important steps of this process will be given in this section. Basically for each photon the following simulations have to be performed: first there is a simple check, whether the source that has emitted the photon is actually inside the FOV.

Figure 4.2: Source distribution observed in deep field surveys: the integral number counts to source flux exhibit a power law shape according to Brandt & Hasinger (2005).

If this is not the case, the photon cannot be seen by the telescope. If it is inside the FOV, the reflection in the mirror system is determined using the PSF model. Some photons may get lost in the mirror system, the others are reflected to particular detector pixels. The charges created by interaction with the semiconductor material are collected in the detector pixels during one readout cycle. The charge creation and storage may be affected by split events or pileup.

At the end of the integration period the charges are shifted to the frame store and read out

Figure 4.3: Source distribution for $100\,000$ faint point sources created by the Monte Carlo algorithm with a power law index $\alpha = -0.5$: the generated power law matches the observed faint-end source flux distribution shown in Fig. 4.2. The bright sources are taken from the RASS-FSC. The random source algorithm only creates the faint end extension of the ROSAT catalog, so the distribution is only one power law with index $\alpha = -0.5$, as the break to the second power law is at a higher flux of $\sim 10^{-14}\,\mathrm{erg\,cm^{-2}\,s^{-1}}$.

from there. Each charge cloud results in a detector specific PHA signal. The relation between photon energy and charge cloud respectively and the PHA channel is described by the RMF model. Finally the time of the detector readout, the detector pixel, and the PHA channel for each event are written to an event list.

4.2.1 Source selection

One of the numerically challenging problems in the simulation of eROSITA's scanning process over the sky is the determination of sources that currently lie within the **F**ield **O**f **V**iew (FOV). As the simulation deals with a great number of sources (according to the expectations eROSITA will discover about 3.2 million AGN), it is worth thinking of an efficient algorithm to select these sources out of the whole catalog with adequate numerical effort.

As previously mentioned (Sec. 2.1.3), the real telescope will be operated with a complicated pointing strategy in order to shift the survey poles to the desired position close to the galactic poles. In a first approach the simulation currently deals with a simplified pointing strategy, where the telescope axis is aligned through the satellite and the center of the Earth, as attitude files for the complex survey geometry are not available so far. In the simplified scenario the right ascension and declination of the telescope axis are equivalent to the current position of the satellite.

In order to check, whether a source of known right ascension θ_s and declination δ_s is within the FOV, with the telescope axis pointing in the direction (θ_t, δ_t), it is useful to calculate the Cartesian coordinates of the corresponding points $\mathbf{r}_s^0$ and $\mathbf{r}_t^0$ on the unit sphere. The position of the source in relation to the direction of the telescope axis can be determined easily by evaluating
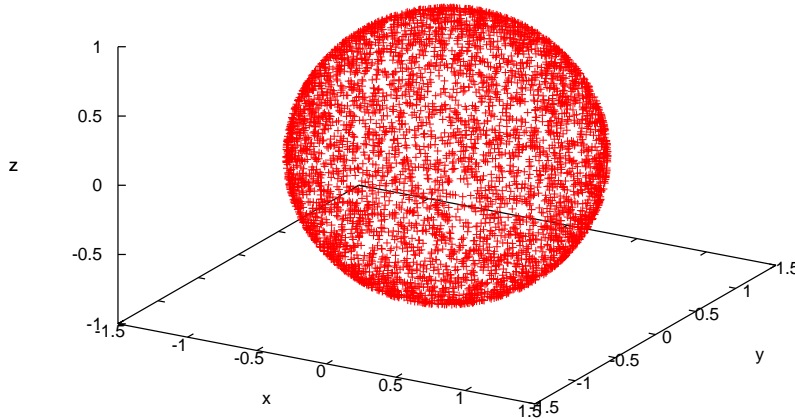
Figure 4.4: Positions of randomly generated point sources on the celestial sphere: the sources are distributed homogeneously on the sphere, i.e., the isotropy of the X-ray sky on large scales is fullfilled.

the scalar product:

$$\cos(\delta) = \mathbf{r}_s^0 \cdot \mathbf{r}_t^0 \begin{cases} \geq \cos\left(\frac{\phi}{2}\right) & \text{inside the FOV} \\ \text{else} & \text{outside the FOV} \end{cases} \tag{4.1}$$

where ϕ is the angular diameter of the FOV and δ the so-called off-axis angle. Assuming a circular FOV, this method can be used for a fast check, whether a source or an individual photon lies within the FOV, and to determine its off-axis angle δ (angle between source direction and telescope axis).

Although the evaluation of the scalar product requires less computational power, the scanning of the entire source catalog involves an order of 10^6 scalar products. The particular orbit of the satellite and the scanning geometry of the telescope reveal a possibility to select a limited number of sources from the entire catalog for a definite time interval of about one revolution. During that period only a limited number of sources along the path of the telescope axis over the sky might be visible. In the current simplified scanning geometry these possibly visible sources lie within a band around the sky along the satellite's orbit. The remaining sources cannot come into the FOV and therefore can be neglected in the scanning process.

To complement this idea, at the beginning of the simulation the entire catalog has to be sorted once in order to obtain all sources within the specified band along the orbit. After this preselection only a subset of all available sources has to be scanned at each simulation time step to determine the currently visible sources. As the number of sources in the preselected catalog is only a fraction of the entire number of sources, this method can save significant amounts of computer power, because the FOV check is a basic and often repeated part of the simulation during the scanning process.

As the orbit and the attitude may change over time due to perturbation effects (e.g., the orbital plane is precessing around the Earth's axis as mentioned in Sec. 5.2.7), the preselected catalog has to be updated after a finite time interval. It is important to determine an adequate update period and a proper angular width β of the preselection band along the orbit. Especially because of short

time loop over entire observation simulation

```
┌─────────────────────────────────────────────┐
│  ┌───────────────────────────────────────┐  │
│  │  source preselection                  │  │
│  │  updated once per orbit revolution    │  │
│  └───────────────────────────────────────┘  │
│                     │                        │
│                     ▼                        │
│  ┌───────────────────────────────────────┐  │
│  │  light curve generation for sources   │  │
│  │  close to the FOV                     │  │
│  └───────────────────────────────────────┘  │
│                     │                        │
│                     ▼                        │
│  ┌───────────────────────────────────────┐  │
│  │  photon generation for sources        │  │
│  │  inside the FOV according to source   │  │
│  │  spectrum and light curve             │  │
│  │  for an interval of ~ 2 s             │  │
│  │  (FOV check each 50 ms)               │  │
│  └───────────────────────────────────────┘  │
│                     │                        │
│                     ▼                        │
│  ┌───────────────────────────────────────┐  │
│  │  scan time–ordered photon list for    │  │
│  │  this interval (~ 2 s)                │  │
│  │    ➤ photon processing                │  │
│  │    ➤ detector readout each 50 ms      │  │
│  └───────────────────────────────────────┘  │
└─────────────────────────────────────────────┘
```

Figure 4.5: Schematic layout of the simulation of the all-sky survey: at the beginning a preselection of the source catalog with respect to the current telescope pointing and the motion of the telescope axis is performed in order to reduce the number of considered sources. For each source close to the FOV a light curve is created using a particular Monte Carlo algorithm. For sources that already have a light curve the latter step is skipped. If the source is within the FOV, photons are generated for an interval of approximately 2 s in advance according to the given light curve and source spectrum, and are stored in a time-ordered list. During the photon generation the search for sources inside the FOV from the preselected source catalog is updated each 50 ms. (The telescope axis moves about 1.2 detector pixels during that time.) After the photon generation the time-ordered list is scanned and individual photon events are simulated according to the available imaging and detector models (PSF, detector response etc.). The events are read out from the detector in intervals of 50 ms and stored to the event list output file. Finally this simulation cycle is repeated from the beginning, whereas the preselection of the source catalog is performed only once per satellite orbit revolution.

periodic variations of the satellite's orbit (Sec. 5.2.8) the band should be wider than the FOV, e.g., twice its angular diameter ($\beta = 2\phi$). Assuming a bandwidth $\beta \approx 2°$ the preselected source catalog on average contains only about 2% of the entirely available sources. The update time for the preselected source catalog could possibly be of the order of the satellite's orbital period, i.e., 96 min.

For the simplified survey geometry the check, whether a source from the catalog lies within the preselected catalog, is almost as simple as the FOV check itself. If $\mathbf{v}_t^0$ is the unit vector in the telescope's direction of motion, the scalar product can be used to determine the angle between the source direction and the normal vector $\mathbf{n}^0$ of the plane defined by the middle of the preselection
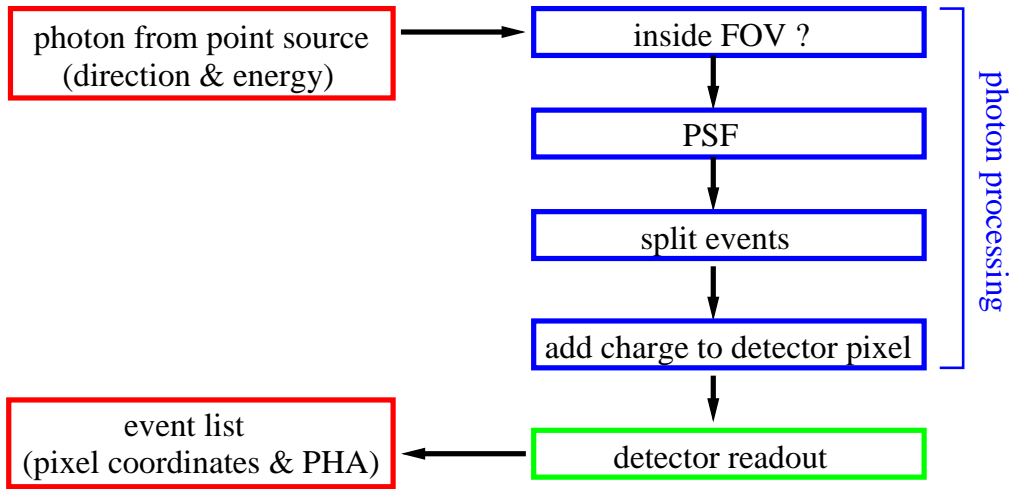
Figure 4.6: Photon processing routine: For sources close to the FOV the simulation generates photons according to the source spectrum and the available light curve. For each photon there is a check, whether it is within the FOV. In that case the photon reflection by the mirror system is modelled with an appropriate algorithm resulting in the point, where the photon hits the detector. The detector model implements realistic features like split events, pileup, and the frame store mode, i.e., the pixels are read out each 50 ms. The charge clouds, created by the photons in the detector pixels during one frame store interval, result in specific PHA values. If the PHA value of a pixel is above a certain threshold, an event is registered, and the PHA value is stored in the event list together with the corresponding pixel coordinates and the time of the detector readout.
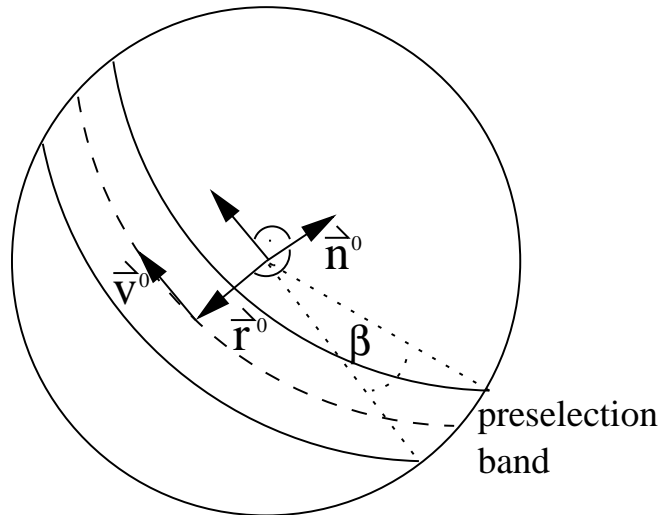
Figure 4.7: Preselection band: dealing with an order of several million sources requires an efficient algorithm to find the sources in the FOV. Instead of checking all available sources at each step of time, there is a preselection of sources along the path of the telescope axis over the sky.

band, which is equivalent to the orbital plane for the simplified survey geometry.

$$\mathbf{n}^0 = \mathbf{r}_t^0 \times \mathbf{v}_t^0 \tag{4.2}$$

$$|\mathbf{r}_s^0 \cdot \mathbf{n}^0| \begin{cases} \leq \cos\left(90° - \frac{\beta}{2}\right) = \sin\left(\frac{\beta}{2}\right) & \text{within the band} \\ & \text{else} & \text{outside the band} \end{cases} \tag{4.3}$$

Applying this method on the source catalog, the relevant sources for the current revolution can be selected in a numerically very efficient way. For a more complicated survey geometry, the source preselection algorithm has to be adapted.

4.2.2 Light curves

During the simulation of the telescope scan over the sky, the program monitors the preselected source catalog (Sec. 4.2.1). If a source comes close to the FOV, i.e., is less than twice the radius of the FOV away from the telescope axis, the simulation generates a light curve for this particular source, in order to have a source count rate for photon creation. The light curve is obtained from a PSD, which could basically be specified for each individual source. Mainly this mechanism is used in order to produce the red-noise typical for AGN, but it could also model the luminosity fluctuations of time-variable objects. In order to generate realistic time-variability in the light curves of the different sources, the simulation could use particular PSDs for the different sources in the source catalogs.

The light curves are created from the corresponding PSDs using a Monte Carlo algorithm introduced by Timmer & König (1995), which implements proper phase and amplitude randomization. The basic concept of this algorithm is to transform a PSD, like in Fig. 4.8, in an inverse Fourier transformation to obtain the light curve, which is shown in Fig. 4.9. **F**ast **F**ourier **T**ransformation (FFT) methods can be applied to reduce the amount of necessary calculation time.

In order to obtain a proper light curve with realistic variability, the PSD, i.e., the individual Fourier coefficients are multiplied with normal distributed complex random numbers. This method also guarantees on the one hand an amplitude randomization and on the other hand also a phase randomization, so there is no bias in the created light curves.

The PSD of an AGN can be modelled by a power law shape

$$P(f) \sim \left(\frac{1}{f}\right)^{\gamma} \tag{4.4}$$

with the power law index $\gamma \sim 1 - 2$ (Benlloch et al., 2001), which results in the typical red-noise. A sample power law with index $\gamma = 1$ is displayed in Fig. 4.8.

After the inverse Fourier transformation has been performed, the light curve has to be normalized to the desired **r**oot **m**ean **s**quare (rms) σ. The Monte Carlo algorithm is designed in such a way, that the first Fourier coefficient must be zero ($P(f = 0) = 0$) such that the mean count rate of the resulting light curve vanishes, and the desired mean count rate of the final light curve has to be added after the inverse Fourier transformation and the normalization.

According to Uttley & McHardy (2001) the rms observed in some flux-variable X-ray light curves is proportional to the mean count rate apart from some constant basic count rate. This relation can be used to determine the σ of the Monte Carlo generated light curve according to the corresponding source flux. The examination of *Cyg X-1*, a galactic black hole, and an X-ray source showing strong variability on timescales of seconds revealed a relation of the rms on the mean count rate and the mean observed source flux $\bar{S}$ respectively, which has the form

$$\sigma = k \cdot \bar{S} - S_0 \tag{4.5}$$

The proportionality factor is of the order or $k \approx 1/3$, whereas the zero-flux S_0 depends on the individual source. This value for σ can be used to roughly determine the required normalization for the light curves generated by the Monte Carlo algorithm, which have some inadequate initial rms. Therefore, the light curves have to be rescaled to obtain a physically meaningful value for σ.
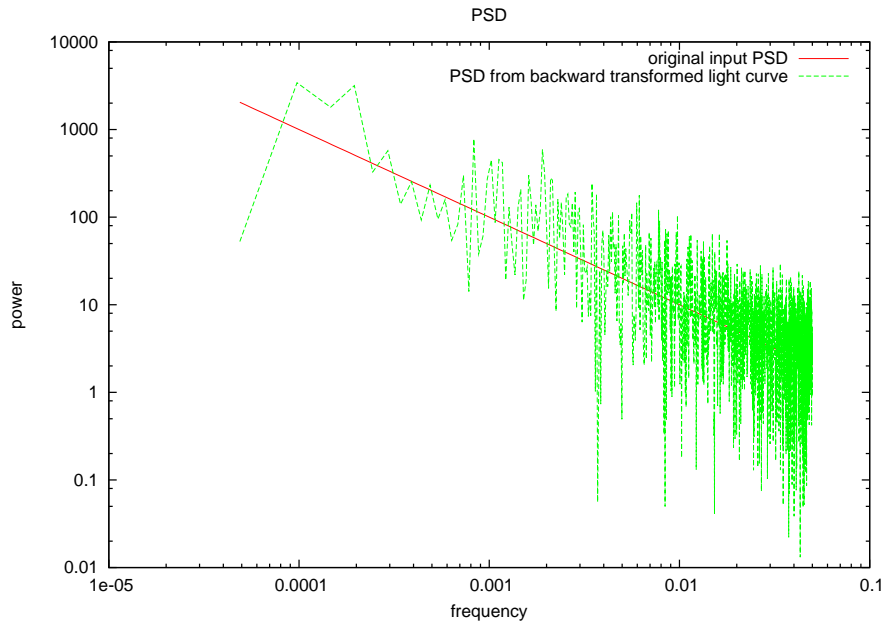
Figure 4.8: Sample PSD: power law shape with index $\gamma = 1$. The backward transformed PSD is obtained from the light curve in Fig. 4.9 by a common PSD determination tool, which is based on Fourier transformation. Basically the backward transformed PSD is the result of an inverse Fourier transformation applied on the original PSD followed by a Fourier transformation. The noise in this graph in contrast to the initial PSD originates from the particular generation of the light curve using the phase and amplitude randomization algorithm of Timmer & König (1995).

In order to verify the correct implementation of the light curve and photon generation algorithm, a long-time pointed observation of a point source with the light curve displayed in Fig. 4.10 was performed. The photon events in the resulting event list were binned in intervals of 1 s to obtain the measured light curve, which is also shown in Fig. 4.10. Obviously the observed simulation output data match the original light curve with respect to the major flux variations. There are some minor deviations for short-term variations, which are caused by statistical effects due to the limited number of detected photons, which are created according to a Poisson distribution. But in total the photon generation algorithm seems to work properly, as the Monte Carlo generated light curve was reproduced.

4.2.3 Photon creation

The current rate of photons coming from a particular source can be determined from the light curve of this source. The problem is the simulation of realistic photon arrival times. Of course, the individual photons will not arrive uniformly at the telescope with a fixed time difference, but they follow a Poisson distribution with a mean rate R, which is obtained from the current light curve bin (Martin, 2004, p. 68). Therefore, the time intervals between two successive photons can be determined according to an exponential distribution $\exp(R)$ with the probability density and probability distribution

$$f(\Delta t) = R e^{-R\Delta t} \tag{4.6}$$

$$F(\Delta t) = 1 - e^{-R\Delta t} \tag{4.7}$$
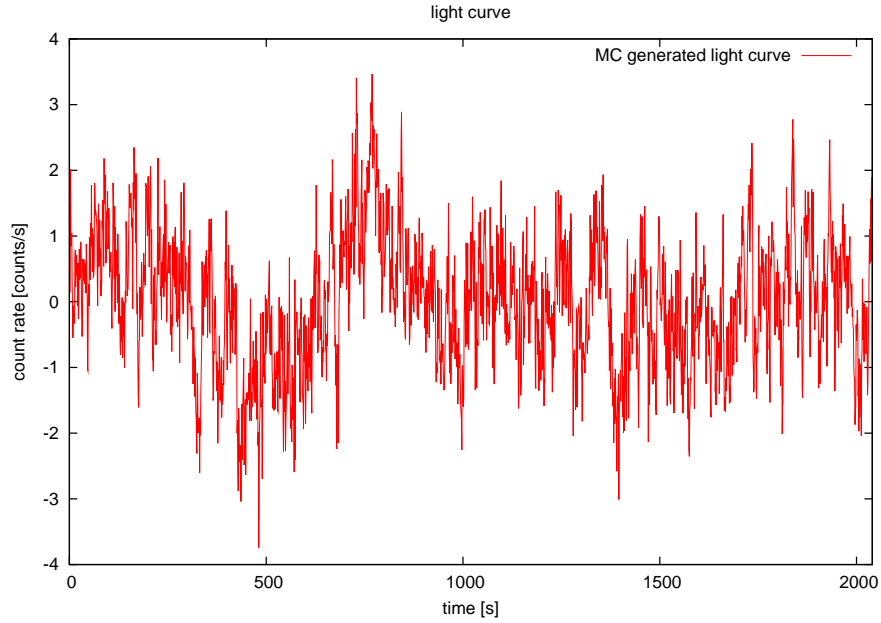
Figure 4.9: Light curve created from the input PSD in Fig. 4.8 using the phase and amplitude randomization algorithm introduced by Timmer & König (1995).
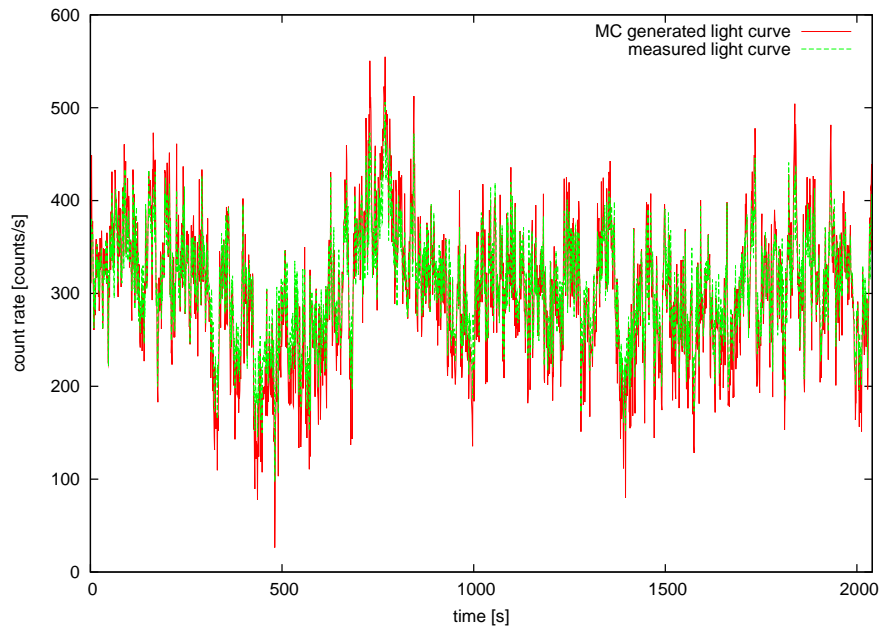
Figure 4.10: Monte Carlo generated light curve in comparison to the measured light curve obtained from photon detection in the measurement simulation: the two light curves are normalized to the same mean count rate.

According to the the *inversion method* (Deák 1990, p. 68ff., Gould et al. 2006, p. 429ff.), this exponential distribution can be obtained from the uniformly distributed random numbers x_i, which are created by the HEAdas random number generator, using the following transformation:

$$(\Delta t)_i = F^{-1}(x_i) = -\frac{1}{R} \ln(1 - x_i) \tag{4.8}$$

41
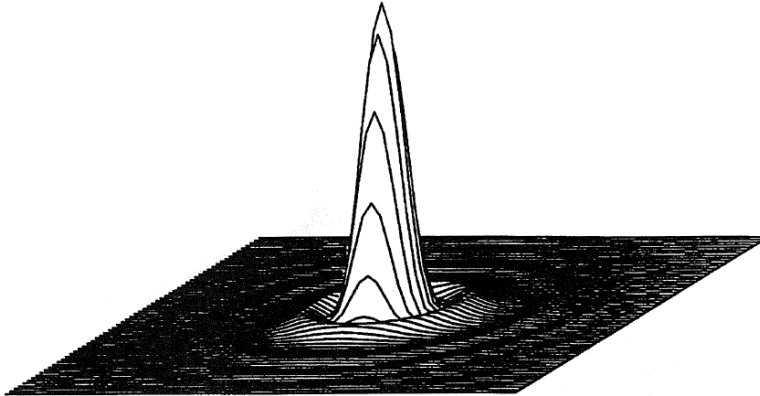
Figure 4.11: Example for a PSF: the plotted function represents the imaging probability for incident photons. Although the PSF is sharply peaked, it is usually not a real δ-function such that the resulting image will exhibit a smearing of the observed sources (Schroeder, 2000).

As the uniform random number distribution $\{x_i\}$ is equivalent to $\{1-x_i\}$, the time intervals between successive photon events can be also determined by the formula

$$(\Delta t)_i = -\frac{1}{R}\ln(x_i) \tag{4.9}$$

Additionally to the specification of the the arrival time, an energy has to be assigned to each incident photon according to the particular source spectrum. The spectral models are stored in PHA files, containing the probability density (i.e., a normalized count rate) for photons in the individual PHA channels (see Sec. 4.3.2). All spectra are read at program call and stored as cumulative probability distribution. At the creation of a new photon, its energy is chosen according to the corresponding source spectrum using the HEAdas random number generator.

By these two methods of creating the arrival time and the photon energy it is ensured that the simulated sources exhibit a proper physical behavior, as the emitted photons follow a realistic Poisson distribution on short timescales and exhibit the proper long term variability and a real spectrum.

4.2.4 Point Spread Function

The **P**oint **S**pread **F**unction (PSF) of an optical system describes the smearing of an observed point source by the imaging process. According to Schroeder (2000) it represents the normalized intensity (time averaged absolute square of the electromagnetic wave function) at a particular point in the image plane. Regarding light as individual photons, the PSF is the probability for each detector pixel to be hit by a given photon, which is coming from a source at a particular position **r** in the sky with the specific energy E. A possible shape of a telescope PSF for a source on the optical axis can be seen in Fig. 4.11.

Actually the PSF describes the spread of a point source caused by the optical imaging system. In the case of eROSITA this means that photons from a point source are not imaged to exactly one definite detector pixel, but there are several pixels in which the photon can arrive with a certain probability. In mathematical terms the image can be regarded as the convolution of the source function with the PSF (Fig. 4.12).

The PSF depends on the direction of the source and on the energy of the photon (Davis, 2001b). Usually the optical system has its best performance for sources on the optical axis with
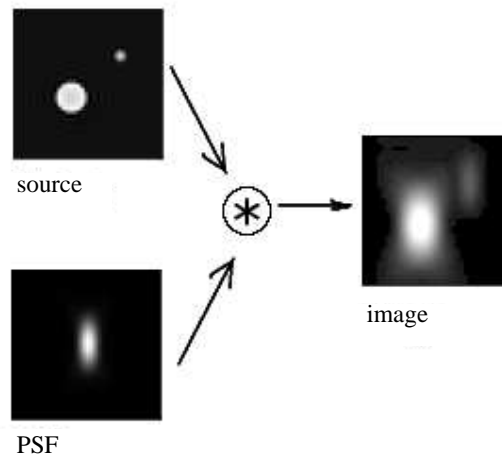
Figure 4.12: Convolution of a source function with a PSF results in the visible image: the sample PSF is not rotationally symmetric, but exhibits a larger spread in the y-direction. These properties can also be found in the image, where the point sources are mainly smeared in this direction. (*http://en.wikipedia.org/wiki/Point_spread_function*)

moderate photon energies. At higher energy and for sources close to the edge of the FOV the PSF peak becomes wider and less sharp.

Each individual mirror system of eROSITA is rotationally symmetric, so the PSF is a function of the off-axis angle δ and the photon energy E. Simulations of the PSF for different discrete values of δ and E, performed by Peter Friedrich (MPE), show that the smearing of the photons is of the order of ± 1 pixel for sources on the optical axis. At the edge of the FOV the spread is larger.

The measurement algorithm uses the PSF to determine the hitting position of the generated photons (cf. photon processing routine illustrated in Fig. 4.6). The explicit form of the PSF can be obtained by the simulation of the mirror reflection, which was performed by Peter Friedrich. His simulation generates X-ray photons for some particular energies and off-axis angles. The output are event lists, which can be used to obtain a discrete model of the PSF for these particular values E_j and δ_i.

The event lists created by the mirror simulation are converted to a more convenient format for the measurement simulation. Basically the single photon events are binned to the corresponding detector pixels. Then all entries of the resulting array are divided by the entire number of simulated photons. By this way one obtains the PSF in a more intuitive form: for each energy value E_j and off-axis angle δ_i one has an array with the individual entries representing the probability that an incident photon is reflected to the corresponding detector pixel. This array can be easily plotted as a discrete 2-dimensional function like in Fig. 4.11.

Of course, the source positions and energies of real photons are not limited to these discrete values, so an interpolation routine has to be applied to obtain a continuous PSF. Therefore the off-axis angle δ has to be determined for each photon using trigonometric relations. Then the best matching PSF is determined. Assuming that the PSF does not change too much for neighboring off-axis angles δ_i and energies E_j, for each continuous set of (δ, E) an interpolation by a step function is applied. For a photon with continuous values (δ, E) the closest available PSF with
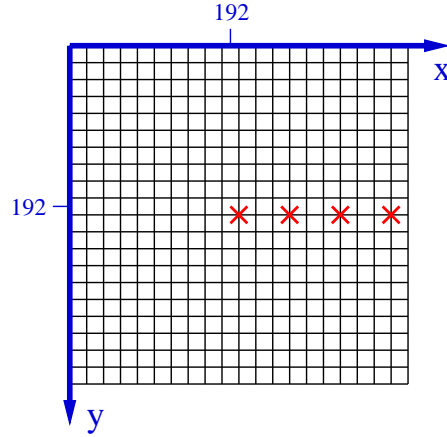
Figure 4.13: The PSF was calculated by a computer simulation for sources with different discrete off-axis angles δ_i (step size 5′).

(δ_k, E_l) is selected, where k and l are chosen in such a way that:

$$|\delta - \delta_k| = \min_{i \in [1;7]} (|\delta - \delta_i|) \tag{4.10}$$

$$|E - E_l| = \min_{j=1,2,3} (|E - E_j|) \tag{4.11}$$

The PSF has been simulated by Peter Friedrich so far, for the off-axis angles $\delta_i = 0′$, 5′, 10′, 15′, 20′, 25′, and 30′, and the photon energies $E_j = 1\,\mathrm{keV}$, 4 keV, and 7 keV. The sketch in Fig. 4.13 schematically displays the source location for the different off-axis angles δ_i.

Some examples of the simulation of the photon reflection by the mirror system are given in Figs. 4.14 – 4.19, where Figs. 4.14 – 4.19 in particular display the δ-dependence of the spot in the PSF. For large off-axis angles (which, in Peter Friedrich's simulation, are chosen in a direction parallel to the x-axis of the detector array) the photons are spread over a wider range than for $\delta \approx 0′$.

Each of the given plots shows the relevant section of the detector array, where the PSF is significantly greater than 0. The position of the detector section within the entire array can be concluded from the pixel coordinates in the figure. The height of the presented peaks describes the probability that an incident photon with the specified energy and off-axis angle is reflected to a particular detector pixel.

The eROSITA mirror system is designed for high precision imaging, so the sources close to the optical axis should exhibit almost no photon spread, and the corresponding PSF peaks for $\delta \approx 0′$ are quite sharp. At the borders of the FOV the focus peak becomes broader and the photons are spread over a wider area of pixels. Additionally the mirror reflectivity decreases, so the probability that an incident photon is measured in any pixel at all becomes smaller for bigger δ. Therefore the PSF for sources near the border of the FOV is quite flat in comparison to on-axis sources, which can be seen clearly comparing Fig. 4.19 to Fig. 4.14.

The higher the photon energy, the more photons get lost and are not focused on the detector by the mirror system, thus the eROSITA mirror system is only adequate for low and intermediate photon energies. This feature can be seen from the decline of the peak in the PSF for 1 keV in Fig. 4.14 to the peak for 7 keV in Fig. 4.16. The imaging probability for photons in dependence on their energy and off-axis angle is displayed in Fig. 4.20.
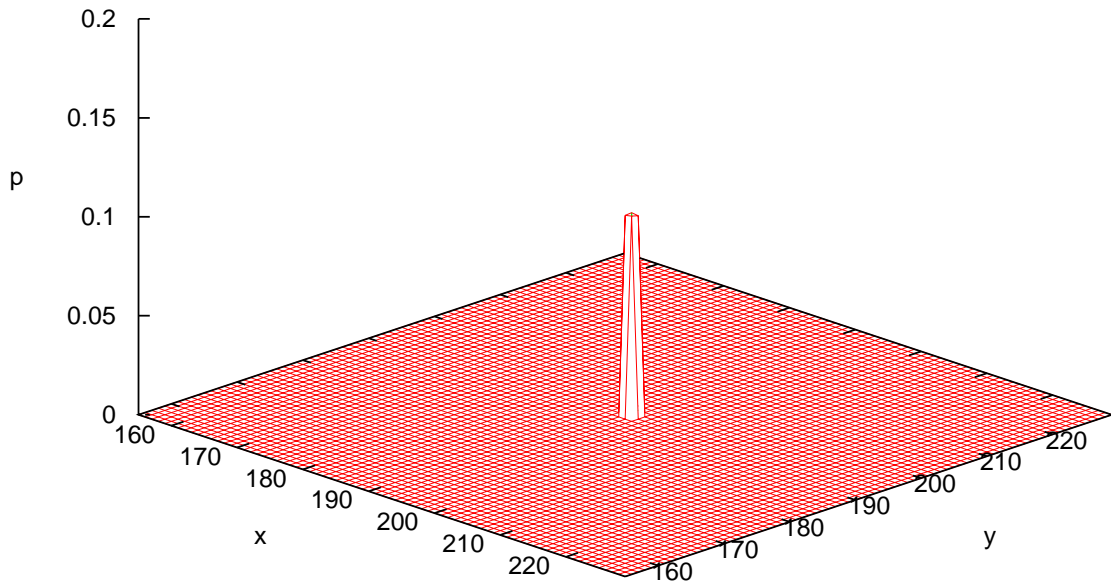
Figure 4.14: Simulated photon reflection for $\delta_1 = 0'$ and $E_1 = 1\,\text{keV}$: the displayed plot is only a section of the entire detector array with 384×384 pixels. The x- and y-coordinate are given in integer detector pixel coordinates, and the height of the peak represents the probability that an incident photon is focused to the corresponding pixel.
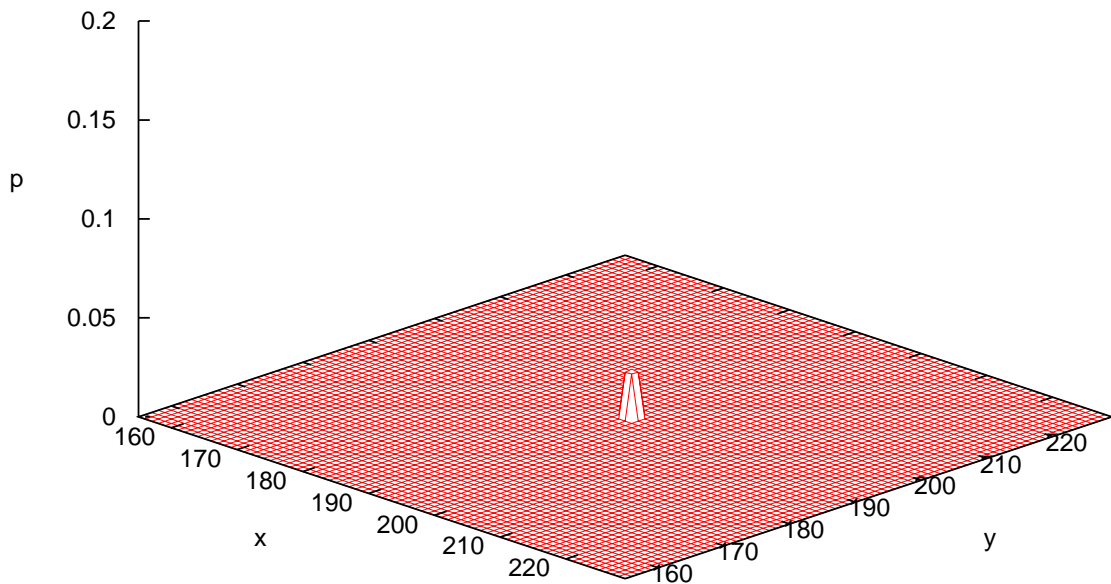
Figure 4.15: Simulated photon reflection for $\delta_1 = 0'$ and $E_2 = 4\,\text{keV}$: the peak is significantly lower than for $E_1 = 1\,\text{keV}$.

4.2.5 Split events

The basic principle of a CCD detector is to measure the charge cloud that is created by photons in the form of electron-hole pairs in the semiconductor material. The more energy an incident photon originally had, the more electron-hole pairs are created. In high energy astronomy usually charge clouds originating from single photons are measured (except from pileup, Sec. 4.2.6).
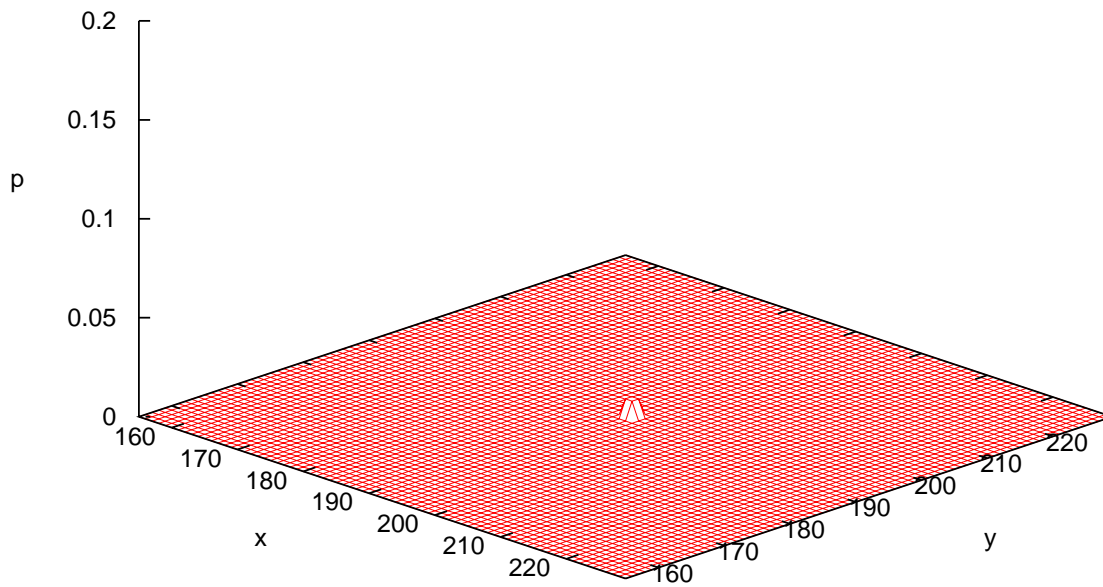
Figure 4.16: Simulated photon reflection for $\delta_1 = 0'$ and $E_3 = 7\,\mathrm{keV}$: due to the decrease of reflectivity for higher photon energies the size of the peak is hardly comparable to the peaks for E_1 and E_2.
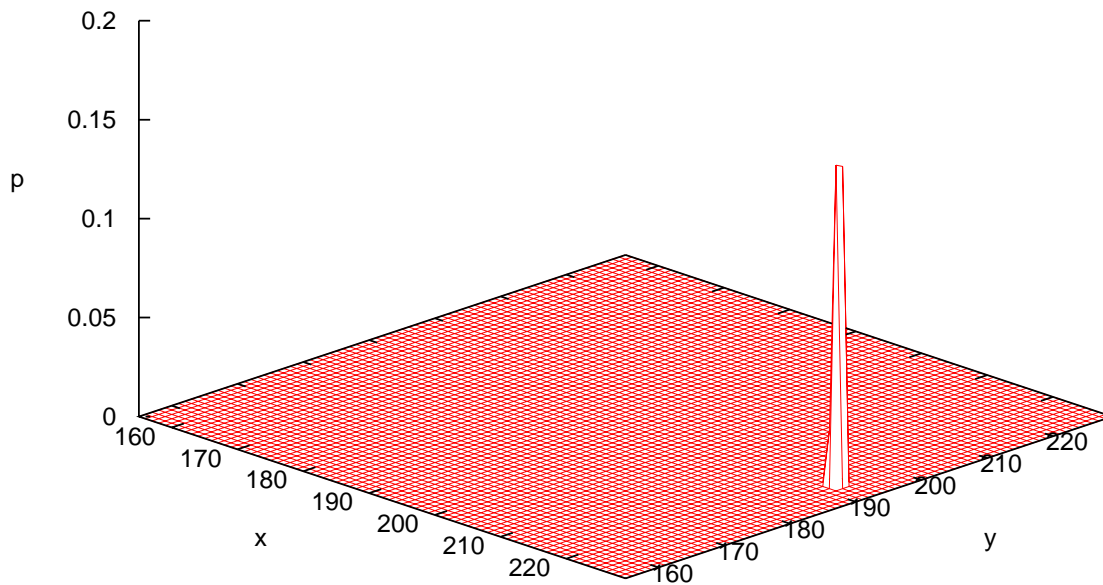
Figure 4.17: Simulated photon reflection for $\delta_2 = 5'$ and $E_1 = 1\,\mathrm{keV}$.

Due to diffusion and Coulomb repulsion in a typical detector the charge cloud has a finite extension of $\sim 5 - 6\,\mu\mathrm{m}$ (Martin, 2004). As the detector pixel size is finite, the charge cloud may be distributed over several neighboring detector pixels, which is called a split event. Usually the size of the charge cloud is smaller than the size of a detector pixel, so there are mainly four basic types of split events (graphically displayed in Fig. 4.21):

- **single event:** The charge cloud lies completely within one detector pixel.
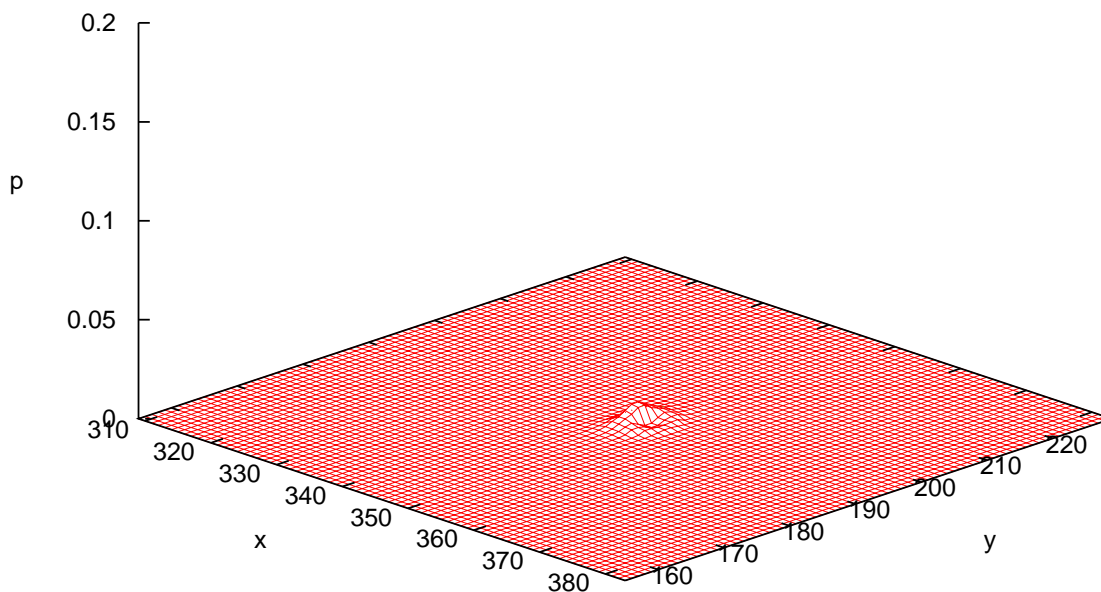
Figure 4.18: Simulated photon reflection for $\delta_6 = 25'$ and $E_1 = 1\,\text{keV}$: in comparison to the sharp PSF peaks for on-axis sources the photons are spread over a much wider pixel area for sources close to the edge of the FOV.
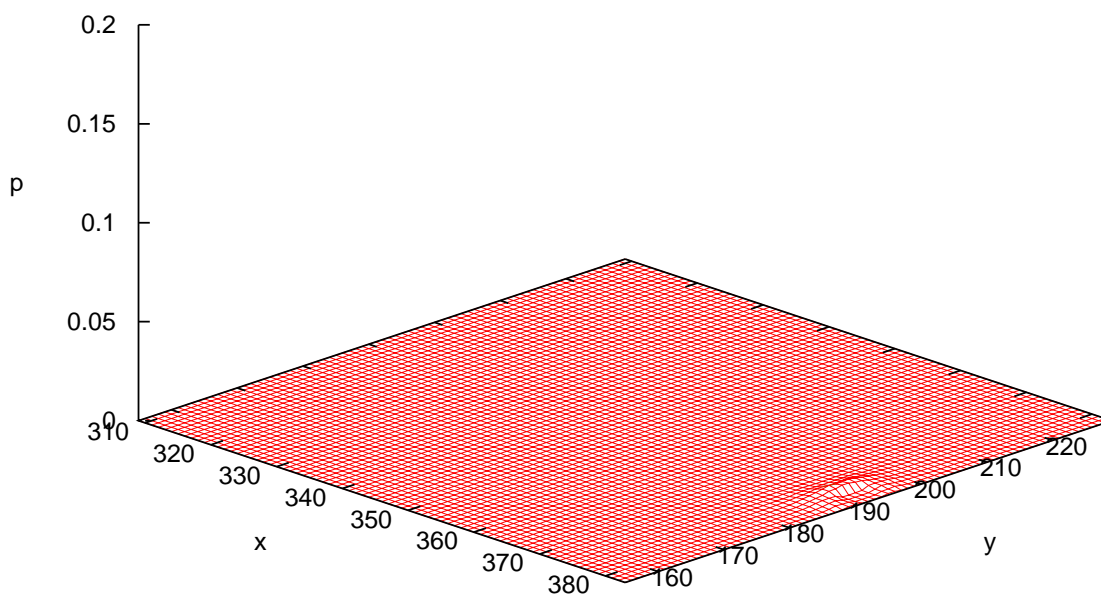
Figure 4.19: Simulated photon reflection for $\delta_7 = 30'$ and $E_1 = 1\,\text{keV}$.

- **double event:** The charge cloud is spread over two neighboring pixels, which have a common border.

- **triple event:** Three neighboring pixels are affected forming a triangle (not a line), where the main part of the charge cloud lies in the "central" pixel.

- **quadruple event:** The four affected pixels form a square, where the pixels with the biggest and the smallest charge fraction lie opposite to each other on diagonal positions.
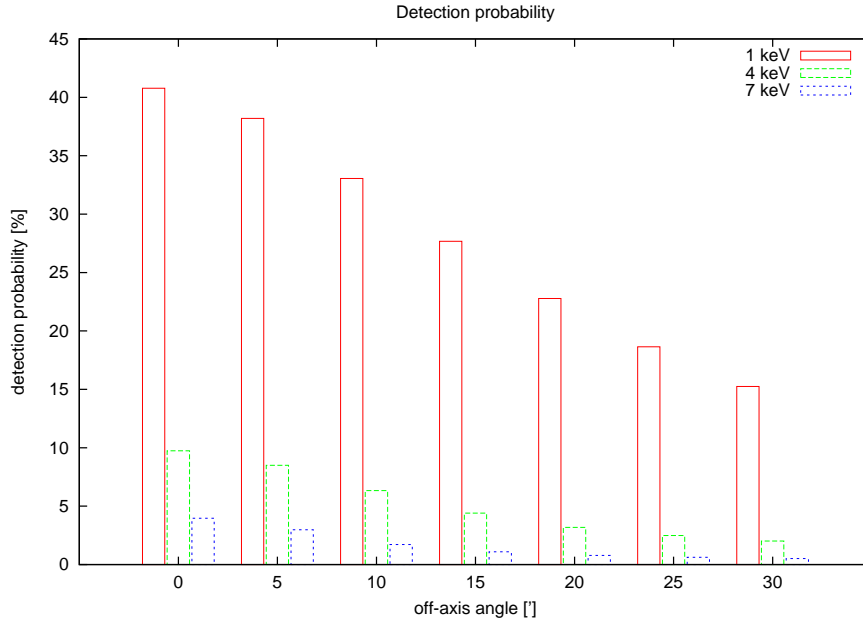
Figure 4.20: Dependence of the mirror reflectivity on the off-axis angle and photon energy: for high energetic photons close the edge of the FOV the reflectivity decreases dramatically. For this determination of the detection probability an ideal detector has been assumed, i.e., with quantum efficiency = 1.
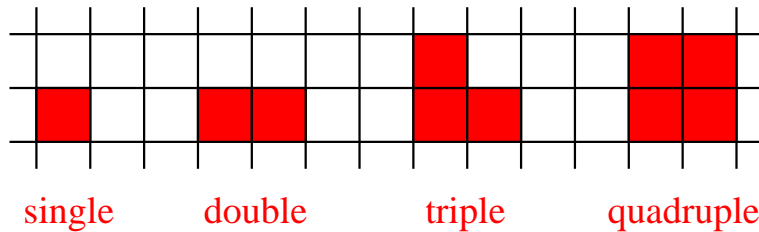
Figure 4.21: The 4 basic types of split patterns. The charge cloud that is created by a photon hitting the detector can be distributed among neighboring pixels. In the eROSITA simulation the 4 displayed pattern types are taken into account.

For the simulation the shape of the charge cloud is assumed to be a 2-dimensional Gaussian distribution with a certain standard deviation σ_{cc}, which can be specified by a program parameter. The radius of the charge cloud is defined as $r_{cc} := 3\sigma_{cc}$. If a photon hits the detector close to the border of a pixel (distance to border $d < r_{cc}$), the part of the entire charge that is measured in the neighboring pixel can be calculated by evaluating the Gaussian integral

$$G(x = -d/\sigma_{cc}) = \frac{1}{2\pi} \int_{-\infty}^{x} e^{-t^2/2} \, dt \qquad (4.12)$$

Because the detector has 2 dimensions, one has to consider the distances d_x and d_y to the next neighboring pixels in both x- and y-direction, and the spatial distribution of the total charge charge
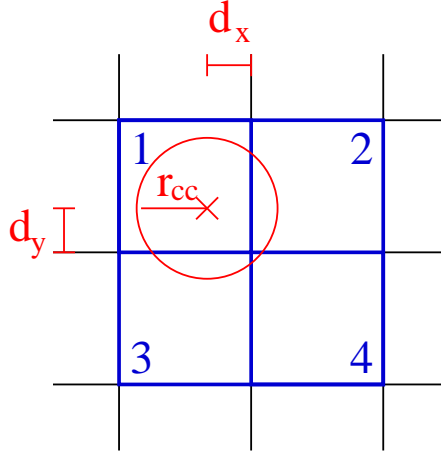
Figure 4.22: Schematic charge distribution in a quadruple event. The charge cloud is assumed to have a Gaussian shape with $r_{cc} := 3\sigma_{cc}$.

Q_0 for the example in Fig. 4.22 can be determined as:

$$Q_1 = \left(1 - G(-d_x/\sigma_{cc})\right)\left(1 - G(-d_y/\sigma_{cc})\right) \cdot Q_0 \tag{4.13}$$

$$Q_2 = G(-d_x/\sigma_{cc})\left(1 - G(-d_y/\sigma_{cc})\right) \cdot Q_0 \tag{4.14}$$

$$Q_3 = \left(1 - G(-d_x/\sigma_{cc})\right)G(-d_y/\sigma_{cc}) \cdot Q_0 \tag{4.15}$$

$$Q_4 = G(-d_x/\sigma_{cc})G(-d_y/\sigma_{cc}) \cdot Q_0 \tag{4.16}$$

where the Gaussian integral (4.12) is calculated numerically using the error function of the *special functions* package in the **G**NU **S**cientific **L**ibrary (GSL).

If, e.g., the charge fraction Q_4 is below the detector threshold (Sec. 4.2.8), no event will be registered in the detector pixel No. 4 (provided that no other photon hits the pixel during the same integration period, which would result in pileup, cf. 4.2.6), and the pattern in Fig. 4.22 will effectively be a triple.

Split events can be reconstruct from the measured data by searching for the possible split pattern with the particular charge distribution. After this analysis the several events that contribute to the same split event can be summarized as one event with a particular grade, which specifies the split pattern (see Ehle et al. 2007). In the current simulation this analysis is not performed, so the events in output event list are designated as singles. The split pattern recognition has to be implemented in an additional algorithm.

The ratio of single events and split events with more than one affected pixel basically depends on the relative size of the charge clouds to the size of the detector pixels. As long as the extent of the charge clouds is small in comparison to the width of the detector pixels, most detected events are singles. But if the radius of the charge cloud is of the same order as the pixel width, a split event will occur, if the distance between the point, where the photon hits the detector, and the nearest pixel edge is smaller than the extension of the charge cloud:

$$d_{edge} < r_{cc} \tag{4.17}$$

Therefore the ratio of split events and total number of photons

$$R_{splits} = \frac{N_{splits}}{N_{photons}} \tag{4.18}$$

can be estimated by comparing the corresponding fractions of pixel area

$$R_{\text{splits}} = 1 - R_{\text{singles}} \,\hat{=}\, 1 - \left(\frac{a - 2r_{\text{cc}}}{a} \right)^2 \qquad (4.19)$$

where a denotes the width of a pixel. For a pixel size of $a = 75\,\mu$m and an estimated charge cloud radius $r_{\text{cloud}} = 6\,\mu$m the area ratio in (4.19) is about $R_{\text{splits}} \approx 29.4\%$. This value is consistent with the simulated ratio of $N_{\text{splits}}/N_{\text{photons}} \approx 28.6\%$ for a sample of $N_{\text{photons}} \approx 1700$ photons.

4.2.6 Pileup

Photon events on the detector are not continuously read out, but the created charges are stored in the detector pixels during the integration time and measured at the end of this period. For eROSITA the integration time is 50 ms. Especially for very bright sources it might happen that two or more photons hit the same detector pixel during the one integration period. In this case the detector measures approximately the sum of the individual charge clouds (Davis 2001a, Ehle et al. 2007), which is then interpreted as a single photon with correspondingly higher energy. Usually there is no possibility to distinguish between these two scenarios of a single or multiple photon event.

    Of course, this has also some effects on the measured data. Particularly the spectrum is slightly shifted to higher energies, because two or more photons can add up to an event with an energy corresponding to a higher energetic photon (Davis, 2001a). If the observed source has a line spectrum, the measured spectrum might contain multiples of the characteristic lines (Martin, 2004, p.49). In the same way the count rate of totally registered events decreases.

    For very bright sources it is even possible that so many photons hit the same detector pixel during one integration period that the resulting charge cannot be hold within the pixel. In that case a fraction of the charge cloud flows to the neighboring pixels, which might result in the detection of additional events with an almost arbitrary energy depending on the transferred charge. This kind of extreme pileup can be identified by, e.g., the occurrence of strange split patterns (Davis, 2001a). This phenomenon is only observed for looking at really bright sources, and the resulting data usually are not very useful due to the corruption of the registered events by these strong pileup effects.

    All in all pileup has negative effects on the quality of the measured data. But for bright sources at least some fraction of pileup events cannot be excluded, as the detector has a finite integration time. Therefore, the pileup of charge clouds, which are created by two or more photons in the same detector pixel (without charge transfer to neighboring pixels), is implemented in the simulation in order to obtain a realistic model of the eROSITA CCD detector for the commonly observed sources.

4.2.7 Detector background

Basically there are two different kinds of background radiation for X-ray telescopes (Ehle et al. 2007, Guainazzi 2008, Puccetti et al. 2008). On the one hand there is the CXRB. Photons originating from the CXRB are detected by the telescope in the same way as photons from different X-ray sources. In the simulation this background is modelled by the extension of the source catalog to a large number of very faint point sources, according to the observed source flux distribution in the deep field surveys (Sec. 4.1.2). Up to now the major fraction of the CXRB has been resolved to discrete sources, so the large sample of very faint sources available in the simulation seems to model that kind of background radiation properly.

    Additionally to this X-ray background that is reflected to the CCD by the mirror system there is a different kind of detector background originating from high energetic radiation passing the
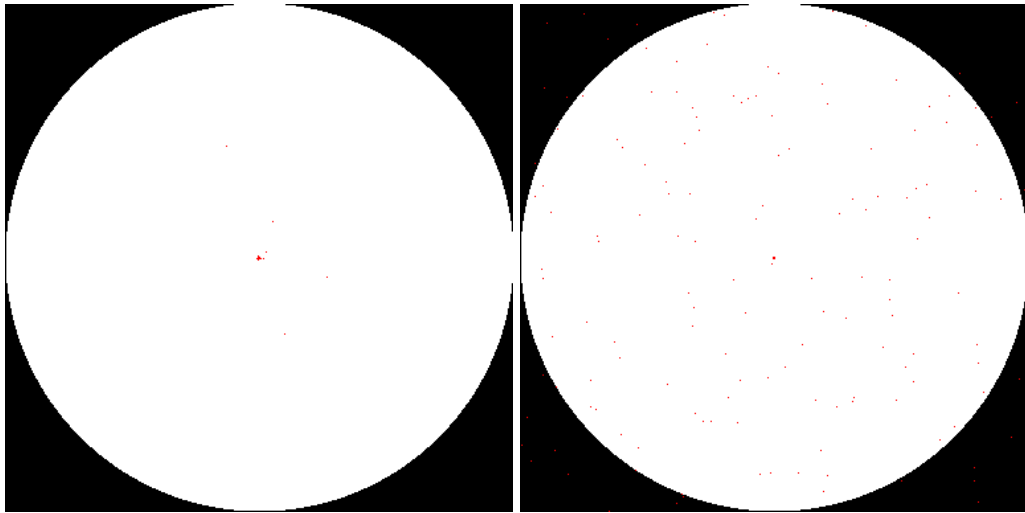
Figure 4.23: Simulation of a pointed observation with duration of 1 s: the left hand picture is the simulated measurement of a point source located directly on the optical axis. The right hand picture shows the same observation with the additional simulation of detector background events (0.001 counts s^{-1} pixel^{-1}). Of course, background events also occur in the detector pixels that lie outside the FOV.

detector shield. The eROSITA CCD is mainly shielded by a copper housing against cosmic radiation. But the telescope mass is limited due to the mounting on the satellite, so the shield is only a compromise between reducing weight and reducing background events. The detector background is caused by protons, electrons and other particles close to the radiation belts of the Earth. Although the eROSITA orbit is lower than the *van-Allen* belts (the lower one starts at about 700 km), there is a certain amount of radiation in this height, too.

In the simulation the detector background is modelled by single photon events that are randomly distributed on the CCD detector. The count rate and the energy spectrum of these background events are program parameters and can be adapted to the results of closer examinations of the expected background. An example for the effect of the background radiation is shown in Fig. 4.23, where simulated detector images for an observation with and without background events are displayed.

In contrary to the CXRB this kind of background events can also occur in pixels that lie outside the actual FOV, because the high energetic particles penetrate the shield from arbitrary directions. The resulting events can be located anywhere on the detector. This particular property makes it possible to measure the true detector background during the flight of the satellite and to take it into consideration in the analysis of the observed events (cf. MPE, et al. 2007).

4.2.8 Detector response

When a photon hits a particular CCD detector pixel it creates a charge cloud by interaction with the semiconductor material. The charge is stored inside the pixel during the integration time (50 ms for eROSITA) and shifted to the frame store area at the end of that period. From the frame store the charge is finally read out and results in a pulse signal, which can be processed by the subsequent electronics. The height of the pulse corresponds to the amount of measured charge and, therefore, to the photon energy, as the charge is usually created by a single photon, provided that there is no pileup. This relation makes it possible to perform spectroscopy on the X-ray photons that are measured by a CCD detector.

An ideal detector would have a linear dependence between the photon energy and the resulting pulse signal, the so-called **P**ulse **H**eight **A**mplitude (PHA). As a real detector has a finite energy resolution with a particular number of discrete PHA channels, the resulting relation between photon energy and PHA channel has approximately the form of a Gaussian function with the following energy resolution (Wilms, 2006):

$$\frac{\Delta E}{E} \propto \sqrt{E} \tag{4.20}$$

Depending on the detector material, there are several additional features mainly originating from atomic emission lines, which have an effect on the charge creation by the incident X-ray photons. Usually these features disturb the clear linear dependence between photon energy and measured PHA channel. Especially at the absorption edges of the CCD material an incident photon might be measured in one out of a major number of PHA channels according to a particular probability distribution.

This probability distribution is usually modelled by the *detector response* function $R(c, E)$, which represents the probability, that an incoming photon with energy E is measured in the PHA channel c. The count rate in a particular PHA channel h can theoretically be obtained according to Wilms (2006), Davis (2001b), or Davis (2001a) as

$$n(c) = \int\limits_0^\infty R(c, E) A(E) F(E) \, dE \tag{4.21}$$

where $A(E)$ is the effective area (see Fig. 2.8 in Sec. 2.2.2), and $F(E)$ is the source flux in the corresponding energy band.

Converting the continuous function $R(c, E)$ to a discrete function with finite energy bins for the photon energy results in the detector *response matrix*

$$R_D(c, j) = \frac{1}{E_j - E_{j-1}} \int\limits_{E_{j-1}}^{E_j} R(c, E) \, dE \tag{4.22}$$

as pointed out by George et al. (1998). $R_D(c, j)$ describes the probability that a photon with energy E in the bin $E_{j-1} < E < E_j$ is measured in the PHA channel c, thus usually $\sum_c R(c, j) = 1$ for each photon energy bin j. The response matrix is sometimes also referred to as *redistribution matrix*, because each row of the matrix represents the redistribution of a monochromatic photon input to the individual PHA channels (Guainazzi, 2008).

The response matrix for a particular detector is usually stored (in a compact format) in the RMF, which also contains the lower threshold for detected events. Below this threshold, the signal created by the charge is too weak for measuring and is therefore neglected.

The simulation uses the RMF to determine the measured PHA channel for the amount of charge, which has been created by the incident photons after they have been reflected by the mirror system. Values below the detector threshold are simply neglected. This method is similar to the procedure described in Puccetti et al. (2008), except for the fact that the mirror properties of Simbol-X are implemented in the additional **A**ncillary **R**esponse **F**ile (ARF), which also describes the imaging probabilities and energy-dependent effective area of the mirror system (George et al., 1998). The eROSITA simulation uses an explicit model for the PSF (Sec. 4.2.4) instead of the ARF.

In Fig. 4.24 the response matrix for the EPIC pn-CCD on the satellite XMM-Newton (Strüder et al., 2001) is visualized. Apart from the main diagonal, which represents the desired linear
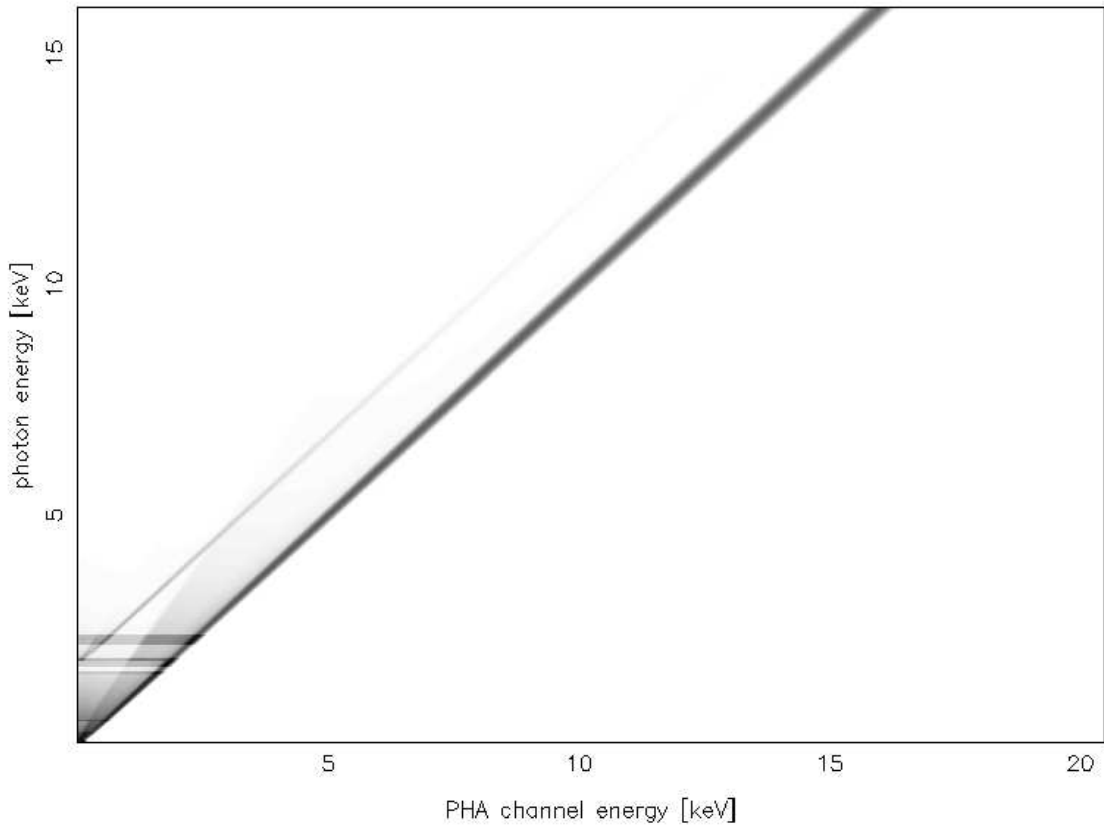
Figure 4.24: RMF matrix of EPIC pn-CCD (XMM-Newton): apart from the ideal linear dependence between photon energy and PHA channel, the RMF exhibits additional features due to the properties of the CCD material. The eROSITA detector is based on the EPIC camera, and, therefore, might have a similar shape.

relation between photon energy and PHA channel energy, the matrix has some additional features. For example, there is a weaker line running parallel to the main diagonal. This means that photons with, e.g., ∼ 3 keV might be either detected at a channel corresponding to ∼ 3 keV or at a lower energy of ∼ 1 keV. For different detectors there might be even more side peaks. Unfortunately these material-dependent effects destroy the unambiguous relation between the photon and the measured energy, which is assumed for the ideal case, and, therefore, complicate spectral analysis.

Currently there is no proper RMF available for the eROSITA CCD, so the simulation was tested with the EPIC pn response matrix. (The eROSITA camera chip is basically a successor of the EPIC CCD.) On reading out the individual detector pixels, the contained charge is converted to a PHA channel according to the probability distribution respresented by the RMF, and taking into account the lower threshold for the detector signals. As the RMF data are stored in a file with standardized format (George et al., 1998), it can be replaced easily, when adequate data for the eROSITA RMF are available.

4.3 File formats

The different input and output data of the simulation, presented in the previous part of this chapter, have to be stored in different FITS files. The format of the individual file types is presented in the

Table 4.1: The essential columns of the binary table in a source catalog file.

Name	Data type	Content
R_A_	Float	right ascension of the source
Dec_	Float	declination of the source
src_cps	Double	source count rate
E_min, E_max	Double	minimum and maximum value of the regarded energy band
SrcModel	String	source model, specifies the name of a FITS file containing the spectrum

following.

As far as possible, standardized file formats were used in order to guarantee a maximum of portability. Depending on the individual mission, there might be slight differences in the contained table columns of the individual FITS files, although the column names themselves are usually clearly defined. Therefore, the design of the file formats for the simulation follows the given standards as far as available, and defines new formats if required. The simulation specific formats should be intuitively accessible.

4.3.1 Source catalogs

The X-ray sources from the RASS-FSC are transformed from the ASCII file, which is published in the internet, to a FITS file (Sec. 4.1.1). The randomly generated sources (Sec. 4.1.2) are also stored in a binary table in FITS format. The FITS tables contain all information required by the simulation for generating photons for the individual sources. An overview of the essential columns is given in Table 4.1. The FITS file for the RASS-FSC contains additional information from the originally published file, but this data is not used by the simulation.

Currently the simulation deals with the right ascension, the declination, and the source count rate. Additional fields are implemented for the spectral model and the minimum and maximum value of the energy range for the source as in a similar simulator for Simbol-X (Puccetti et al., 2008), but are not used in the current implementation of the program. Their usage is one of the future development steps of the simulation. Of course, there are also further possible parameters like a light curve model for each individual source, which could also be implemented, if required.

4.3.2 PHA files

For the generation of photons the simulation requires spectra of the individual sources (and the detector background model). These data are stored in several FITS files, where each file contains one particular spectrum. The binary table in each file has basically two columns. The first column gives the PHA channel, i.e., the energy bin of the photon energy, and the second column contains the count rate in the corresponding channel (cf. Table 4.2).

Simple spectra for testing the simulation can be created easily with a few lines of code (sub-program *create_spectrum*), whereas real source spectra for the execution of the simulation can be obtained from spectral analysis software like XSPEC. Similar to the sources detector background has a particular spectrum, which is also stored in a PHA file for input in the simulation.

Table 4.2: The individual columns of the binary table in a PHA file.

Name	Data type	Content
CHANNEL	Long	PHA channel
COUNTS	Float	count rate in this channel, normalized to $\sum_c \text{counts}(c) = 1$

Table 4.3: The individual columns of the binary table in a PSF file. This file format is not a standard, but designed in particular for the simulation.

Name	Data type	Content
OFFAXANG	Float	off-axis angle δ
ENERGY	Float	photon energy E in keV
X, Y	Integer	offset of the $n \times m$ sub-matrix
		(n and m are stored in header keywords)
PSF_DATA	Float-Array	matrix entries of $n \times m$ sub-matrix
	with length $n \cdot m$	stored in a 1-dimensional array

4.3.3 PSF files

The imaging properties of the mirror system are modelled by the PSF. Mathematically it can be described by a $N \times N$ matrix for each available off-axis angle and energy combination (Sec. 4.2.4), where N is the width of the detector in pixels. The individual matrix entries $P_{x,y}(\delta, E)$ represent the probability, that an incident photon with energy E at the off-axis angle δ is reflected to the detector pixel with coordinates x and y.

Usually most matrix entries are equal to zero, so each $N \times N$ matrix can be reduced to a $n \times m$ sub-matrix, with $n \leq N$, which consumes less memory. These sub-matrices are stored in a FITS binary table, which can be read by the simulation.

4.3.4 RMF files

Similar to the PSF of the mirror system the measurement probabilities of a detector are described by the detector response function and the detector response matrix respectively. The exact meaning of these terms is described in Sec. 4.2.8.

Basically the detector response matrix is a huge $n \times m$ matrix, where n is the number of energy bins for incident photons, and m is the number of possible PHA output channels. The matrix entry $(R_D)_{j,i}$ represents the probability that an incident photon with energy E_j is measured in the PHA channel i, which corresponds to the energy E_i (George et al., 1998).

The necessary information for modelling a particular detector is stored in FITS format in the RMF. This file contains two binary tables. One of them is called *MATRIX* or *SPECRESP MATRIX* and contains the actual detector response matrix including the definition of the energy bins E_j for the incident photons. The relation between the PHA channel i and the corresponding measured energy value E_i is given in the additional table *EBOUNDS*.

Apart from that the RMF contains header keywords with information about the number of PHA channels and the lower detector threshold. The detailed layout of the FITS file is presented in George et al. (1998).

Table 4.4: The individual columns of the binary table in an orbit file.

Name	Data type	Content
TIME	Float	time t (refers to header keyword *MJDREF*)
X, Y, Z	Float	position of the satellite at time t
Vx, Vy, Vz	Float	velocity of the satellite at time t

Table 4.5: The individual columns of the binary table in an attitude file.

Name	Data type	Content
VALTIME	String	time t in format yyyy-mm-ddThh:mm:ss
TIME	Float	time t (refers to header keyword *MJDREF*)
VIEWRA	Float	right ascension of telescope axis at time t
VIEWDECL	Float	declination of telescope axis at time t
ROLLANG	Float	*roll-angle* at time t
ASPANGLE	Float	solar aspect angle at time t

4.3.5 Orbit files

Orbit files are stored as FITS files and contain a binary table with the position and velocity of the satellite at particular points of time (cf. Table 4.4). Usually the time statements in the different FITS files refer to a reference date specified by the header keyword *MJDREF*. Position and velocity are given in Cartesian coordinates, which can be easily processed by the simulation algorithm.

At the time when the simulation was developed, no real orbit data were available for eROSITA, so the orbit files had to be created by an orbit propagation algorithm according to the methods described in Chap. 5. The resulting files are used as input for the measurement simulation and the attitude calculator, which requires the orbit information to determine the telescope's pointing direction.

As the data are only available for discrete points of time with steps of several seconds or minutes, the simulation software has to perform an interpolation in order to obtain the satellite's position and velocity for intermediate points of time.

4.3.6 Attitude files

Attitude files specify the satellite's orientation in 3-dimensional space at particular points of time. Basically the attitude can be given by defining three different angles. For convenience in the context of the simulation two of them are the right ascension and declination of the telescope axis respectively. The third angle, specified as *roll-angle* is the rotation angle of the satellite around the telescope axis. An overview is given in Table 4.5.

Using the orbit files created by the orbit propagation algorithm, attitude information can be determined easily, assuming that the telescope always points straight away from the center of the Earth. Actually the survey geometry is more complicated (cf. Sec. 2.1.3), but the attitude files for this complex pointing strategy will be provided at later steps of the development of eROSITA. With the assumption of the simplified survey geometry the right ascension and declination of the telescope axis are equal to the satellite's right ascension and declination. The *roll-angle*, i.e., the rotation angle around the telescope axis, is still not fixed and can be determined according to the

requirement that the solar panels should collect as much sunlight as possible. Therefore, the *roll-angle* can be directly calculated from the position of the Sun, which is obtained from an algorithm presented in Meeus (1998).

According to this attitude model the satellite's orientation is determined from a given orbit file. The resulting attitude file contains the time, the right ascension and declination of the telescope axis, the *roll-angle*, and, as additional information, the solar aspect angle. Reading this attitude file, the simulation software can easily determine the telescope viewing direction.

4.3.7 TLE

The **T**wo **L**ine **E**lements (TLEs) are a commonly used format to describe a satellite's orbit parameters. As the name already suggests, they basically consist of two lines with a fixed length of 69 characters each and a specific data format. There might also be a zeroth line with the satellite's common or human readable name, but the important data are contained in the subsequent two lines.

Apart from different identifiers and classifications a TLE provides drag parameters and the satellite's orbital elements for a specified point of time. Therefore, TLEs are usually used to predict the orbit for a short period assuming Keplerian motion, maybe including perturbation theory up to first order. As the exact orbit perturbations by gravitational and atmospheric effects cannot be given over a long span of time, the TLE elements have to be updated regularly.

A detailed description of the TLE format is given in Steiner & Schagerl (2004, p. 148ff). with a list of the meaning of the individual bytes in each line. As the orbit determination program, which was developed in the course of this simulation, neglects atmospheric effects, mainly the second line of the TLEs is important, because it contains information about the Keplerian orbital elements. Although an interface for input and output of TLEs was implemented for the orbit propagation algorithm, usually orbit files containing the satellite's positions and velocities in Cartesian coordinates are preferred as input for the simulation.

There are several orbit prediction programs on the web using TLE input files to calculate, e.g., the ground tracks of the ISS or some well-known satellites. Unfortunately the calculations in these programs are not accurate enough to determine the eROSITA orbit for the simulation, as they usually neglect perturbation effects or implement only first order perturbation theory. Therefore, a separate algorithm had to be developed for this purpose.

4.3.8 Event lists

The result of the simulated measurement process is an event list with the detected photons (or multi-pixel events). The corresponding FITS output file contains a binary table with the time of the measurement, the PHA channel, the so-called grade (cf. Sec. 4.2.5), and the pixel coordinates of each individual event. The individual columns in the table are listed in Table 4.6. The columns are implemented according to George et al. (1994). Of course, there is a large number of additional columns that can be added if required.

As the detector is not read out continuously but in time intervals of 50 ms, the time in the event list is usually not equal to the time, when the photon has actually hit the detector. The time difference might be up to the integration time. The PHA channel represents the measured detector energy, where the relation between channel and energy is given in the *EBOUNDS* table of the RMF (Sec. 4.3.4), and the grade should designate the split pattern. As the simulation implements no recognition of split events, all events are regarded as singles. Therefore, the grade is not used and set to zero in this context.

Table 4.6: The individual columns of the binary table in an event list file.

Name	Data type	Content
TIME	Float	time of the detection, i.e., readout time of the frame
PHA	Long	number of detector PHA channel
GRADE	Integer	number that specifies the split type
RAWX, RAWY	Integer	raw detector pixel coordinates of the event

Chapter 5

Satellite orbits

It is commonly known that satellites move around the Earth on elliptic or in many cases even circular orbits. Similar to the motion of the planets around the Sun these orbits can be described by Kepler's laws. If the simplification of a purely two point mass gravitational system is not postulated, the satellite's motion becomes more complicated and perturbation theory has to be applied.

This chapter treats the mathematical background of simple Kepler orbits and provides an introduction to orbit perturbation theory up to second order. Effects from the particular shape of the Earth's gravitational potential on close Earth orbits are taken into account, particularly with regards to eROSITA, which was originally designed for a 600 km orbit because of the low particle background in this height. Formulas for the semi-analytical solution of the mathematical problem of close Earth orbits are given in Appendix A.

The effects of atmospheric drag are neglected, because they are smaller than the gravitational effects and would result in even more complicated mathematical effort. As the atmospheric parameters usually cannot be predicted with the required accuracy, the resulting model would be insufficient for long term orbit calculations anyhow.

5.1 Issue

In order to simulate the measurement process of eROSITA, one has to know the position of the satellite and the pointing of the telescope on the satellite's orbit (see Chap. 4). The latter is particularly important to determine the visible sources inside the FOV from the given source catalogs.

As this simulation was developed at quite an early stage of the eROSITA mission preparation, there was no realistic orbit data available for Spectrum-X-Gamma, and its motion around the Earth had to be calculated for the simulation. One of the simulation's targets is the generation of detector event lists as input for the NRTA software, which affords quite accurate position and attitude data. The orbit propagation algorithm can also be used later during the flight of eROSITA to determine the position of the satellite, when the data from the spacecraft is not available or unreliable.

The orbit calculation had to be developed completely, as actually no program code or complete tools were available for the desired purpose. Most programs and references with explicit formulas do either only work with Keplerian orbits or first order perturbation theory, or perform a numerical integration. In this work a semi-analytical approach was implemented, which provides on the one hand a quite good understanding of the mathematical background and on the other hand the possibility to determine the influence of particular parameters on the satellite's orbit. Therefore,

the semi-analytical method was preferred to the purely numerical approach.

5.2 Mathematical background

Before discussing the particular implementation of the orbit calculation for the simulation, the following section will provide a short overview of the mathematical background. First the pure Keplerian satellite motion is regarded, including the introduction of the necessary formalism, later perturbation effects are discussed with respect to their importance for close Earth orbits.

5.2.1 Two-body system

First the gravitational interaction of two point masses in a two-body system is considered using Newton's laws. As this is a popular problem, it is treated in many books about astrodynamics. This section will follow the approach of Steiner & Schagerl (2004).

According to Newton, the force between the masses m_1 and m_2 located at $\mathbf{r}_1$ and $\mathbf{r}_2$ is

$$F = \frac{Gm_1m_2}{r^2} \tag{5.1}$$

with $\mathbf{r} = \mathbf{r}_1 - \mathbf{r}_2$ and $r = |\mathbf{r}|$. For $m_1 = $ const. and $m_2 = $ const. one obtains:

$$\ddot{\mathbf{r}} = -\frac{G(m_1 + m_2)}{r^3}\mathbf{r} \tag{5.2}$$

This non-linear differential equation describes the relative motion of the two point masses. The motion of the center of mass is just a straight line, as there are no external forces.

This general formula can be applied to the particular situation of a satellite on its orbit around the Earth, where m_1 is chosen as the mass of the Earth and m_2 as the mass of the satellite. For convenience the origin of the coordinate system Γ' is set into the center of the Earth ($\mathbf{r}_1 = \mathbf{0}$) and the following approximation is performed, as $m_1 \gg m_2$:

$$G(m_1 + m_2) \approx Gm_1 =: \mu \tag{5.3}$$

Because of the huge mass difference the center of mass coincides approximately with the center of the Earth:

$$\mathbf{R} = \frac{m_1\mathbf{r}_1 + m_2\mathbf{r}_2}{m_1 + m_2} \approx \mathbf{r}_1 = \mathbf{0} \tag{5.4}$$

The position of the satellite is $\mathbf{r}_2 = \mathbf{r}$, as $\mathbf{r}_1 = \mathbf{0}$. To determine $\mathbf{r}(t)$ as a function of time, the following equation of motion has to be solved, which is obtained from Eq. (5.2) using (5.3):

$$\ddot{\mathbf{r}} = -\mu\frac{\mathbf{r}}{r^3} \tag{5.5}$$

As already mentioned above, this equation describes the relative motion of the two masses, i.e., in this particular case the motion of the satellite around the Earth. Scalar multiplication of (5.5) with $\dot{\mathbf{r}}$ yields:

$$\ddot{\mathbf{r}} \cdot \dot{\mathbf{r}} + \mu\frac{\mathbf{r} \cdot \dot{\mathbf{r}}}{r^3} = 0 \tag{5.6}$$

Taking into account the following relations:

$$\ddot{\mathbf{r}} \cdot \dot{\mathbf{r}} = \frac{d}{dt}\left(\frac{1}{2}\dot{\mathbf{r}}\right) = \frac{d}{dt}\left(\frac{1}{2}v^2\right) \tag{5.7}$$

$$\mathbf{r} \cdot \dot{\mathbf{r}} = \frac{d}{dt}\left(\frac{1}{2}\mathbf{r}^2\right) = \frac{d}{dt}\left(\frac{1}{2}r^2\right) = r\dot{r} \tag{5.8}$$

one obtains

$$\frac{d}{dt}\left(\frac{1}{2}\dot{\mathbf{r}}^2\right) + \mu\frac{\dot{r}}{r^2} = \frac{d}{dt}\left(\frac{v^2}{2} - \frac{\mu}{r}\right) = 0 \tag{5.9}$$

which means that

$$C := \frac{v^2}{2} - \frac{\mu}{r} = \text{const.} \tag{5.10}$$

is a constant of motion. Often it is referred to as *specific energy* of the relative motion.

The conservation of angular momentum can also be derived from Eq. (5.5) by calculating the vector product with $\mathbf{r}$:

$$\mathbf{r} \times \ddot{\mathbf{r}} = \frac{d}{dt}(\mathbf{r} \times \dot{\mathbf{r}}) = 0 \tag{5.11}$$

$$\Rightarrow \mathbf{h} := \mathbf{r} \times \dot{\mathbf{r}} = \text{const.} \tag{5.12}$$

Choosing the z'-axis of the coordinate system Γ' to point in the direction of $\mathbf{h}$, the vectors $\mathbf{r}$ and $\dot{\mathbf{r}}$ lie in the x'-y'-plane. Kepler's second law can easily be derived from the conservation of angular momentum

$$\mathbf{h}\, dt = h\, \mathbf{e}_{z'}^0\, dt = \mathbf{r} \times \dot{\mathbf{r}}\, dt = 2\, dA\, \mathbf{e}_{z'}^0 \tag{5.13}$$

where $\mathbf{e}_{z'}^0$ is the unit vector along the z'-axis of Γ', and $dA = 1/2\, r^2 d\theta$ is the half area of the parallelogram spanned by $\mathbf{r}$ and $\dot{\mathbf{r}}dt$, i.e., dA is the area the vector $\mathbf{r}$ is wandering over during the time interval dt. As $h = |\mathbf{h}| = \text{const.}$, Kepler's second law is proven:

$$\dot{A} = \frac{1}{2}r^2 d\theta = \frac{1}{2}h = \text{const.} \tag{5.14}$$

With the choice of $\mathbf{h} \parallel \mathbf{e}_{z'}^0$, $\mathbf{r}$ and $\dot{\mathbf{r}}$ lie in the x'-y'-plane and can be expressed in polar coordinates. Introducing $\mathbf{e}_r = (\cos\theta, \sin\theta, 0)^T$ and $\mathbf{e}_\theta = (-\sin\theta, \cos\theta, 0)^T$ with the angle θ between $\mathbf{r}$ and the, at the moment, arbitrary x'-axis, one can write

$$\mathbf{r} = r\mathbf{e}_r \tag{5.15}$$

$$\dot{\mathbf{r}} = \dot{r}\mathbf{e}_r + r\dot{\theta}\mathbf{e}_\theta \tag{5.16}$$

In this representation the angular momentum is

$$\mathbf{h} = (r\mathbf{e}_r) \times (\dot{r}\mathbf{e}_r + r\dot{\theta}\mathbf{e}_\theta) = r^2\dot{\theta}\mathbf{e}_{z'}^0 \tag{5.17}$$

as $\mathbf{e}_r \times \mathbf{e}_\theta = \mathbf{e}_{z'}^0$.

To determine the geometry of the orbit, it is useful to define the quantity $\mathbf{q} := \dot{\mathbf{r}} \times \mathbf{h} - \mu\mathbf{e}_r$, which is also a constant of motion. With (5.5) $\times\mathbf{h} \Rightarrow$

$$\begin{aligned} 0 &= \ddot{\mathbf{r}} \times \mathbf{h} + \frac{\mu}{r^3}\mathbf{r} \times \mathbf{h} \\ &= \frac{d}{dt}(\dot{\mathbf{r}} \times \mathbf{h}) + \frac{\mu}{r^3}(r\mathbf{e}_r) \times \left(r^2\dot{\theta}\mathbf{e}_{z'}^0\right) \\ &= \frac{d}{dt}(\dot{\mathbf{r}} \times \mathbf{h}) - \mu\dot{\theta}\mathbf{e}_\theta \\ &= \frac{d}{dt}(\dot{\mathbf{r}} \times \mathbf{h} - \mu\mathbf{e}_r) \end{aligned} \tag{5.18}$$

where the relation $\dot{\mathbf{e}}_r = \dot{\theta}\mathbf{e}_\theta$ has been used. The vector $\mathbf{q}$ lies in the x'-y'-plane, because $\mathbf{q} \cdot \mathbf{h} = 0$, and the direction of the x'-axis of the coordinate system Γ' can be defined as $\mathbf{e}_{x'}^0 := \mathbf{q}/q$, thus one obtains:

$$\cos\theta = \frac{\mathbf{q} \cdot \mathbf{r}}{qr} = \frac{\mathbf{r} \cdot (\dot{\mathbf{r}} \times \mathbf{h}) - \mu r}{qr} \tag{5.19}$$

After performing the cyclic permutation $\mathbf{r} \cdot (\dot{\mathbf{r}} \times \mathbf{h}) = \mathbf{h} \cdot (\mathbf{r} \times \dot{\mathbf{r}}) = \mathbf{h} \cdot \mathbf{h} = h^2$ this results in:

$$\cos\theta = \frac{h^2}{qr} - \frac{\mu}{q} \tag{5.20}$$

$$r(\theta) = \frac{p}{1 + e\cos\theta} \tag{5.21}$$

with $p = h^2/\mu$ and $e = q/\mu$.

This equation describes conic sections (Steiner & Schagerl, 2004, p. 21f.). Depending on e the corresponding orbit is a circle ($e = 0$), an ellipse ($0 < e < 1$), a parabola ($e = 1$), or a hyperbola ($e > 1$). The so-called eccentricity e must be positive, because $q = |\mathbf{q}| \geq 0$ and $\mu > 0$. The cases $e \geq 1$ will be neglected in the following, as only closed satellite orbits are taken into account. For eROSITA one even has an almost circular orbit with $e \approx 0$.

5.2.2 Spherical approximation

In the previous section a system consisting of two point masses has been considered. The satellite's extension is negligible in comparison to the distance between the satellite and the center of the Earth, and one can approximately describe the satellite as a point mass.

But the radius of the Earth is of the same order as the distance between the center of the Earth and the satellite. Therefore, it must be proven explicitly that the same formulas can be used for the satellite problem as for a system of two point masses. This will be done by showing that for distances greater than the radius of the Earth our planet has approximately the same gravitational potential, as if all its mass would be concentrated in its center.

For this calculation it is assumed that the Earth is a perfect sphere with radius R_e and its mass M_e is distributed uniformly inside the sphere. The gravitational potential for a test mass m at a position $\mathbf{r}$ above the surface ($|\mathbf{r} - \mathbf{r}_1| = |\mathbf{r}| = r > R_e$) is:

$$V(\mathbf{r}) = -Gm \int_{M_e} \frac{dM}{s} = -Gm \int_0^{R_e} \int_0^{\pi} \frac{2\pi\rho(r')}{s} \sin(\psi)\, d\psi\, dr' \tag{5.22}$$

with $s = |\mathbf{r} - \mathbf{r}'|$, $\rho(r') = \rho = \text{const.}$, and the infinitesimal mass element $dM = 2\pi\rho r'^2 \sin\Psi\, dr'\, d\Psi$ (see Fig. 5.1). Using the cosine identity $r^2 = r^2 + r'^2 - 2rr'\cos(\psi) \Rightarrow s\, ds = rr' \sin(\psi)\, d\psi$ the integration variable can be replaced:

$$V(\mathbf{r}) = -2\pi Gm \int_0^{R_e} \int_{r-r'}^{r+r'} \frac{\rho r'}{r}\, ds\, dr' = -4\pi \frac{Gm}{r} \int_0^{R_e} r'^2 \rho\, dr' = -\frac{GmM_e}{r} \tag{5.23}$$

In other words the Earth has indeed the same potential, as a point source with the same mass at the center of the Earth would have, and the formalism developed in Sec. 5.2.1 can be used for the calculation of a satellite's orbit.

5.2.3 Kepler orbits: Kepler elements

In Sec. 5.2.1 it was concluded from Eq. (5.21) that the orbit of a satellite around the Earth is an ellipse (or a circle), if only finite systems with $e < 1$ are considered. The Earth and, therefore, the origin of the coordinate system is located in one of the two focal points of the ellipse, as Kepler's first law claims.

To describe the motion of the satellite on its orbit around the Earth, it is useful to switch from the coordinate system Γ' introduced in Sec. 5.2.1 to the geocentric equator system Γ with the
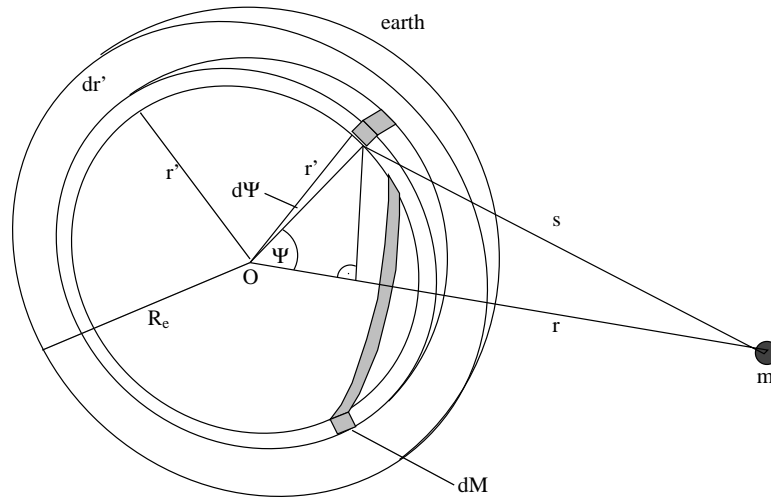
Figure 5.1: Integration over the total volume of the Earth according to Steiner & Schagerl (2004).

z-axis pointing in the direction of the north pole, the x-axis to the First Point of Aries (a fixed direction with respect to the background of stars), and the y-axis perpendicular to both of them.

This coordinate system is moving around the Sun along the path of the Earth, but the directions of its axes are fixed in reference to the cosmic background. As the satellite's motion is almost entirely dominated by the gravitational potential of the Earth, influences from the Sun or other planets can be neglected, and the coordinate system can be regarded as an inertial system. The geocentric equator system is a common choice for astronomical problems. It is more convenient for this purpose than Γ', which depends on the attitude of the orbital plane.

To characterize the orbit and the position of the satellite, the ellipse can be defined, e.g., by the length of its semimajor axis a and its eccentricity e. But, of course, there are also different possible sets of parameters to describe an ellipse. For example, a common choice is to define the parameter p of the ellipse instead of the semimajor axis a, where

$$p = a(1 - e^2) \tag{5.24}$$

Having specified the ellipse, the actual position of the satellite is given by the angle θ, which is called *true anomaly*, as shown in Fig. 5.2.

Therefore, one needs a set of three parameters such as (a, e, θ) to describe the position of the satellite within the orbital plane. But the alignment of this plane in 3-dimensional space is still arbitrary. In order to designate a particular orbital plane, usually the three additional angles i, Ω and ω are introduced.

The first parameter i is called the *inclination* and is defined as the angle between the orbital plane and the equatorial plane of the Earth. Its possible values lie in the interval from $0°$ to $180°$, where orbits with $i < 90°$ are called *prograde*, $i = 90°$ means a *polar*, and $i > 90°$ a *retrograde* orbit.

The value of Ω designates the right ascension of the ascending node, i.e., the direction, where the satellite's orbit crosses the equatorial plane coming from the southern hemisphere. From the geometrical point of view the ascending node is defined by the intersection line of the equatorial with the orbital plane. Possible values lie in the interval from $0°$ to $360°$.

To determine the position of the perigee, the so-called *argument of perigee* ω is used, which specifies the angle between the vector from the center of the Earth (i.e., the origin of the coordinate

63
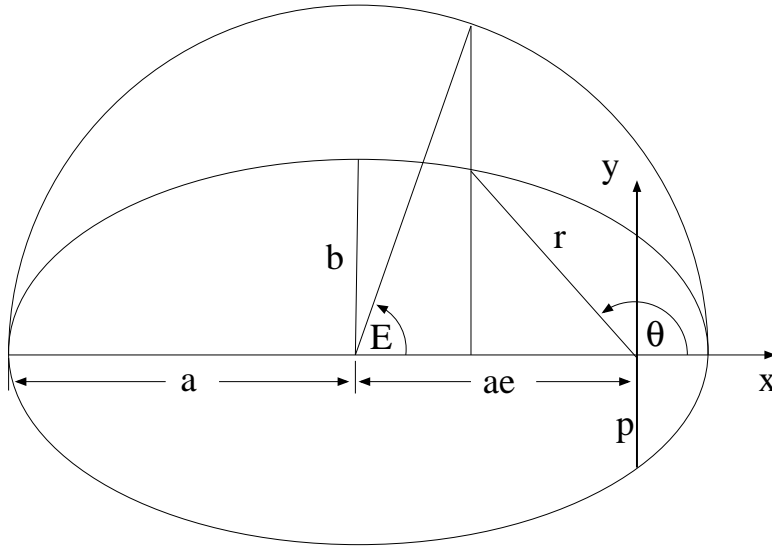
Figure 5.2: Parameters of an ellipse according to Flury (1991): the ellipse is clearly defined by its semimajor axis a and its eccentricity e. The position of the satellite on the ellipse can be specified by the eccentric anomaly E or the true anomaly θ.

system) to the perigee of the ellipse (the satellite's closest position to the Earth) and the vector from the center of the Earth to the ascending node. The argument of perigee has possible values between $0°$ and $360°$.

Fig. 5.3 shows the parameter set (i, Ω, ω) describing the attitude of the orbital plane according to the geocentric equator system. Specifying the six Keplerian orbital elements $(a, e, i, \Omega, \omega, \theta)$ is a common choice to define the complete orbit of a satellite. It is quite suitable for analytical calculations and is used, e.g., as basis for the NORAD TLE format (Sec. 4.3.7).

5.2.4 Kepler orbits: equations of motion

This section will describe how the position and velocity of a satellite can be obtained from its Keplerian elements. The most difficult part of this calculation is the determination of the true anomaly θ depending on the time. It is shown below that there is no explicit analytical function $\theta(t)$. But it is possible to calculate a quantity M called the *mean anomaly*, which is defined as

$$M = n(t - t_\pi) \tag{5.25}$$

with the mean motion

$$n = \sqrt{\frac{\mu}{a^3}} = \frac{2\pi}{T} \tag{5.26}$$

and t_π the time, when the satellite was in the perigee position.

$$T = 2\pi \sqrt{\frac{a^3}{\mu}} \tag{5.27}$$

is the time for one revolution, so n can be regarded as the mean angular velocity of the satellite. The motion is not uniform (e.g., the satellite is faster at perigee and slower at apogee according to Kepler's second law), and, therefore, the mean anomaly is not equal to θ or E. This would only be valid for a circle, i.e., $e = 0$. In that special case the equality $n = E = \theta$ holds.
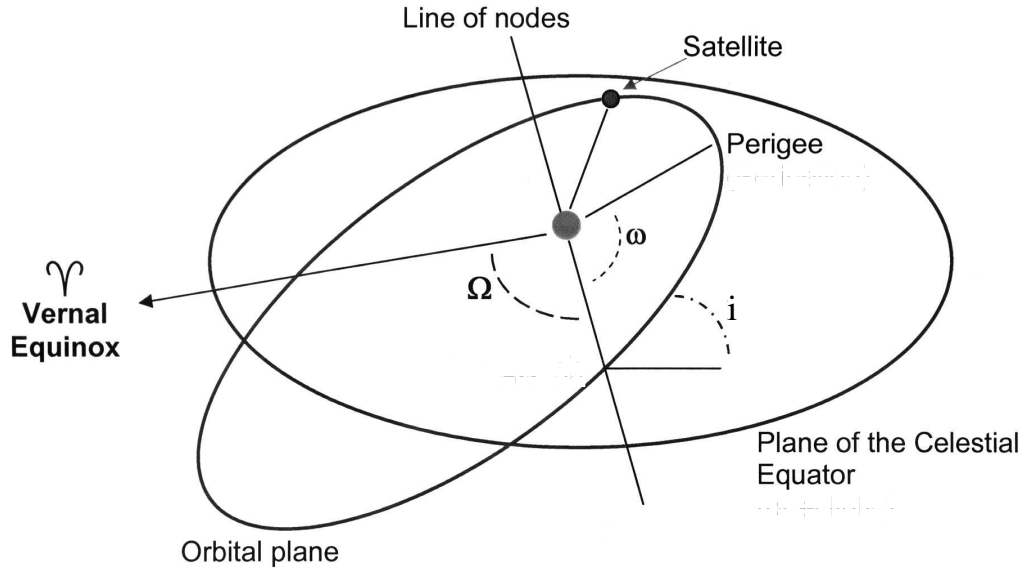
Figure 5.3: The attitude of the orbital plane in 3-dimensional space is defined by three angles: the inclination i, the right ascension of the ascending node Ω, and the argument of perigee ω (North Carolina State University / Department of Physics, *http://www.physics.ncsu.edu*).

Considering Kepler's second law and using some geometric relations, one can derive the *Kepler equation* (Steiner & Schagerl, 2004, p. 68ff.):

$$M = E - e\sin(E) \tag{5.28}$$

This relation between the mean and the eccentric anomaly is a basic element of orbit calculations. Unfortunately it cannot be solved for E, so there is no possibility to obtain the eccentric anomaly as a function of time. Instead of that for a given time t the mean anomaly M can be calculated according to Eq. (5.25). The result is put in the Kepler equation to determine the corresponding eccentric anomaly E using numerical methods like the Newton algorithm. Knowing E, it is quite simple to obtain the actually required true anomaly θ by using (Steiner & Schagerl, 2004, p. 71)

$$\tan\left(\frac{E}{2}\right) = \sqrt{\frac{1-e}{1+e}}\tan\left(\frac{\theta}{2}\right) \tag{5.29}$$

The position $\mathbf{r}$ of the satellite according to the coordinate system Γ' can then be expressed in terms of E or θ (Fig. 5.2) by using some geometric relations. As shown by Flury (1991, p. 20):

$$\mathbf{r} = a\,(\cos E - e)\,\mathbf{e}_{x'}^0 + a\,\sqrt{1-e^2}\,\sin E\,\mathbf{e}_{y'}^0 \tag{5.30}$$

Taking into account (Flury, 1991, p.20)

$$\dot{E} = \sqrt{\frac{\mu}{a}}\frac{1}{r} \tag{5.31}$$

Differentiation of Eq. (5.30) yields:

$$\dot{\mathbf{r}} = \mathbf{v} = -\frac{\sqrt{\mu a}}{r}\sin E\,\mathbf{e}_{x'}^0 + \frac{\sqrt{\mu p}}{r}\cos E\,\mathbf{e}_{y'}^0 \tag{5.32}$$

The remaining problem that still has to be solved is the transformation from Γ' to the equatorial coordinate system Γ. For that purpose the vectors $\mathbf{e}_{x'}^0$ and $\mathbf{e}_{y'}^0$ have to be expressed in terms of $\mathbf{e}_x^0 = (1, 0, 0)^T$, $\mathbf{e}_y^0 = (0, 1, 0)^T$, and $\mathbf{e}_z^0 = (0, 0, 1)^T$:

$$\mathbf{e}_{x'}^0 = \begin{pmatrix} \cos\omega\cos\Omega - \sin\omega\sin\Omega\cos i \\ \cos\omega\sin\Omega + \sin\omega\cos\Omega\cos i \\ \sin\omega\sin i \end{pmatrix} \tag{5.33}$$

$$\mathbf{e}_{y'}^0 = \begin{pmatrix} -\sin\omega\cos\Omega - \cos\omega\sin\Omega\cos i \\ -\sin\omega\sin\Omega + \cos\omega\cos\Omega\cos i \\ \cos\omega\sin i \end{pmatrix} \tag{5.34}$$

Knowing the orbital elements of a satellite, its position and velocity can be determined for any given point of time following the previous method. Therefore, the parameter set $(a, e, i, \Omega, \omega, t)$ or $(a, e, i, \Omega, \omega, M)$ can be used to define the position and velocity.

A similar method for calculating this data is based on the *argument of latitude*

$$u := \omega + \theta \tag{5.35}$$

and can be found, e.g., in Flury (1991, p. 38). In principle it is the same approach using the true anomaly θ instead of the eccentric anomaly E.

5.2.5   Oblateness of the Earth

In the previous sections (especially in Sec. 5.2.2) the Earth was assumed to have a perfectly spherical shape with uniform mass distribution. With that assumption it is possible to replace the Earth's gravitational potential by the potential of a point mass with the same total mass, so the two-body formalism developed in section 5.2.1 can be applied.

The resulting orbits for eccentricity $e < 1$ are periodic, i.e., the satellite remains in its orbit over the time, and after each revolution around the Earth it returns to its initial position. This approximation is quite suitable for satellites at high altitudes, i.e., several 1000 kilometers above the Earth's surface.

For lower orbits the Earth's particular shape has to be regarded more closely. Due to its rotation the equatorial radius is about 21.4 km larger than the distance of north and south pole. The resulting shape can be approximated by a rotational ellipsoid, which is schematically shown in Fig. 5.4.

Additionally to the oblateness there are further deviations from a perfect spherical potential by inhomogeneous mass distribution. All these effects are small in comparison to the gravitational force on the satellite (the oblateness $f = 21.4\,\text{km}/6378\,\text{km} \approx 0.34\%$ is the most noticeable deviation), so perturbation theory can be applied to calculate the effects of deviations from the perfectly spherical shape.

For that purpose the description of the Earth's gravitational potential has to be approximated by a more realistic equation (Flury 1991, Steiner & Schagerl 2004). The simplified form used in section 5.2.1 was:

$$V_0 = -\frac{\mu}{r} \tag{5.36}$$

This potential satisfies the Laplace equation, which generally holds outside of any body with arbitrary shape:

$$\nabla^2 V_0 = 0 \tag{5.37}$$
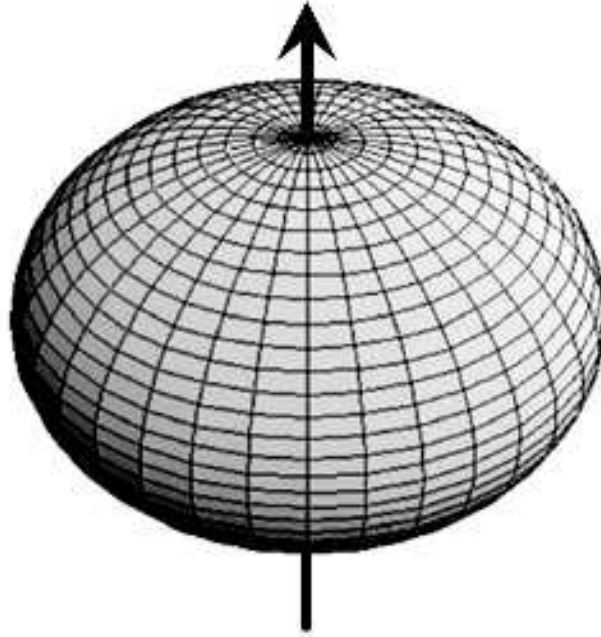
Figure 5.4: The equatorial diameter of the Earth is about 42 km greater than the distance of north and south pole. Therefore, the shape can be approximated by a rotational ellipsoid (Walter, 2007).

Expressing the ∇ operator in some kind of spherical coordinates with the latitude φ and the longitude λ

$$x = r \cos \varphi \cos \lambda \tag{5.38}$$

$$y = r \cos \varphi \sin \lambda \tag{5.39}$$

$$z = r \sin \varphi \tag{5.40}$$

yields the following form of the Laplace equation for a general potential V:

$$\nabla^2 V = \frac{1}{r^2} \left[\frac{\partial}{\partial r} \left(r^2 \frac{\partial V}{\partial r} \right) + \frac{1}{\cos \varphi} \frac{\partial}{\partial \varphi} \left(\cos \varphi \frac{\partial V}{\partial \varphi} \right) + \frac{1}{\cos^2 \varphi} \frac{\partial^2 V}{\partial \lambda^2} \right] = 0 \tag{5.41}$$

A general ansatz for solving this differential equation is the following product:

$$V(r, \varphi, \lambda) = R(r) P(\varphi) L(\lambda) \tag{5.42}$$

with

$$R(r) = A r^n + B r^{-n-1} \tag{5.43}$$

$$P(\varphi) = P_{nm}(\sin \varphi) \tag{5.44}$$

$$L(\lambda) = C \cos(m\lambda) + D \sin(m\lambda) \tag{5.45}$$

Due to the condition $V(\infty) = 0$ one obtains $A = 0$. The functions P_{nm} are the associated Legendre polynomials:

$$P_{nm}(x) = (1 - x^2)^{m/2} \frac{d^m}{dx^m} P_n(x) \tag{5.46}$$

with the Legendre polynomials:

$$P_n(x) = \frac{1}{2^n n!} \frac{d^n}{dx^n} (x^2 - 1)^n \tag{5.47}$$

Table 5.1: Jeffrey coefficients (from Goddard Earth Model) and Legendre polynomials for $n = 2, 3, 4$ according to Flury (1991).

n	$J_n \cdot 10^6$	$P_n(x)$
2	1082.6268	$\frac{1}{2}\left(3x^2 - 1\right)$
3	−2.5356	$\frac{1}{2}x\left(5x^2 - 3\right)$
4	−1.6234	$\frac{35}{8}\left(x^4 - 30x^2 + 3\right)$
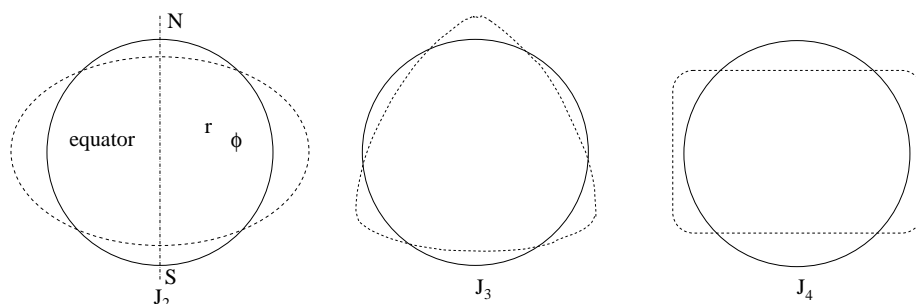
Figure 5.5: Equipotential surfaces for $V(r, \varphi) = V_0(r) + V_n(r, \varphi) = $ const., with $V_n(r, \varphi) = \frac{\mu}{r} J_n \left(\frac{R_e}{r}\right)^n P_n(\sin \varphi) = $ const. (dotted lines) in comparison to $V_0(r) = -\frac{\mu}{r} = $ const. (circles) (pictures taken from Steiner & Schagerl 2004 with ϕ denoting the latitude).

Therefore the Earth's potential can be written in the form:

$$V = -\frac{\mu}{r}\left[1 + \sum_{n=1}^{\infty}\sum_{m=0}^{n}\left(\frac{R_e}{r}\right)^n P_{nm}(\sin \varphi)\left(C_{nm}\cos(m\lambda) + D_{nm}\sin(m\lambda)\right)\right] \qquad (5.48)$$

For the current purpose it is sufficient to regard the special case $m = 0$. With this particular choice the potential can be simplified:

$$V = -\frac{\mu}{r}\left[1 - \sum_{n=1}^{\infty} J_n \left(\frac{R_e}{r}\right)^n P_n(\sin \varphi)\right] \qquad (5.49)$$

where $J_n = -C_{n0}$. The *Jeffrey coefficient* $J_1 = 0$ vanishes, as the center of mass of the Earth coincides with the origin of the coordinate system (Steiner & Schagerl, 2004, p. 120). The coefficients for $n = 2, 3, 4$ taken from the Goddard Earth Model (GEM-10, cf. Flury 1991, p. 70), which have been determined by exact measurements of satellite orbits, and the corresponding Legendre polynomials are listed in Table 5.2.5.

In Fig. 5.5 the effect of the individual spherical harmonics in the expansion of the gravitational potential is displayed. The coefficients J_2 and J_4 mainly describe the effects of the oblateness of the Earth (see Sec. 5.2.7), whereas the J_3 term is caused by asymmetry between the northern and southern hemisphere.

As discussed in Sec. 5.2.1 for $e < 1$, the relative motion of two point masses is a closed orbit. Therefore a satellite's motion around the Earth would be periodic in the coordinate system Γ, if the Earth's potential had a perfectly spherical and uniform mass distribution, i.e., $V \equiv V_0$, as assumed in Sec. 5.2.2, and if there was no atmospheric drag.

The additional terms for $n > 1$ in the expansion of the gravitational potential (5.49), however, result in a variation of the orbital elements. For example they cause a precession of the orbital

plane around the Earth's axis, which will be explained below. In comparison to the gravitational effects the atmospheric drag mainly results in a continuous reduction of the semimajor axis *a* and the eccentricity *e* (Steiner & Schagerl, 2004, p. 131ff.). The influence by the atmosphere does not exert a conservative force on the satellite and its calculation is mathematically more challenging.

5.2.6 Perturbation theory

In order to calculate the perturbation effects on the orbital elements, a system of differential equations for the parameter set $(a, e, i, \Omega, \omega, M)$ has to be found. The derivation of these equations affords some mathematical effort, so the exact procedure will not be presented in this text, especially as it is described in almost any book on orbit calculations that deals with perturbation theory (e.g., Steiner & Schagerl 2004, ch. 4 or Flury 1991, ch. 3). Finally one obtains the following Lagrange perturbation equations:

$$\frac{da}{dt} = -\frac{2}{na} \frac{\partial W^*}{\partial M} \tag{5.50}$$

$$\frac{de}{dt} = -\frac{1 - e^2}{na^2 e} \frac{\partial W^*}{\partial M} + \frac{\sqrt{1 - e^2}}{na^2 e} \frac{\partial W^*}{\partial \omega} \tag{5.51}$$

$$\frac{di}{dt} = -\frac{\cot i}{na^2 \sqrt{1 - e^2}} \frac{\partial W^*}{\partial \omega} + \frac{1}{na^2 \sqrt{1 - e^2} \sin i} \frac{\partial W^*}{\partial \Omega} \tag{5.52}$$

$$\frac{d\Omega}{dt} = -\frac{1}{na^2 \sqrt{1 - e^2} \sin i} \frac{\partial W^*}{\partial i} \tag{5.53}$$

$$\frac{d\omega}{dt} = -\frac{\sqrt{1 - e^2}}{na^2 e} \frac{\partial W^*}{\partial e} + \frac{\cot i}{na^2 \sqrt{1 - e^2}} \frac{\partial W^*}{\partial i} \tag{5.54}$$

$$\frac{dM}{dt} = \frac{1 - e^2}{na^2 e} \frac{\partial W^*}{\partial e} + \frac{2}{na} \frac{\partial W^*}{\partial a} \tag{5.55}$$

These differential equations describe the temporal change of the orbital elements due to the perturbation potential W^*, which can be obtained from

$$W(\mathbf{r}) = V(r) - V_0(r) = \sum_{n > 1} V_n(r) \tag{5.56}$$

All perturbation forces can be derived from this potential. After a coordinate transformation $(\mathbf{r}, \mathbf{v}) \rightarrow (a, e, i, \Omega, \omega, M)$ the perturbation potential can be expressed in terms of Keplerian orbital elements:

$$W(\mathbf{r}) \rightarrow W^* (a, e, i, \Omega, \omega, M) \tag{5.57}$$

With W^* the Eqs. (5.50) – (5.55) can be used to determine the effect of the gravitational perturbation on the orbital elements.

As the calculation of the atmospheric drag is quite challenging due to the number of parameters for a proper model of the atmosphere, it will not be explained in this thesis. For the explicit mathematical calculation see Klinkrad (1983) or Liu & Alford (1979). According to Liu & Alford (1979) for satellites above 200 km it is a valid approximation to neglect atmospheric drag due to its magnitude in comparison to gravitational effects. Therefore, in the following only perturbations that are caused by the shape of the Earth's gravitational potential will be considered.

5.2.7 Perturbations due to oblateness

To determine the contribution of the J_2 terms in the expansion of the gravitational potential, one has to regard the following perturbation potential according to Eq. (5.49) and Table 5.2.5 (Steiner
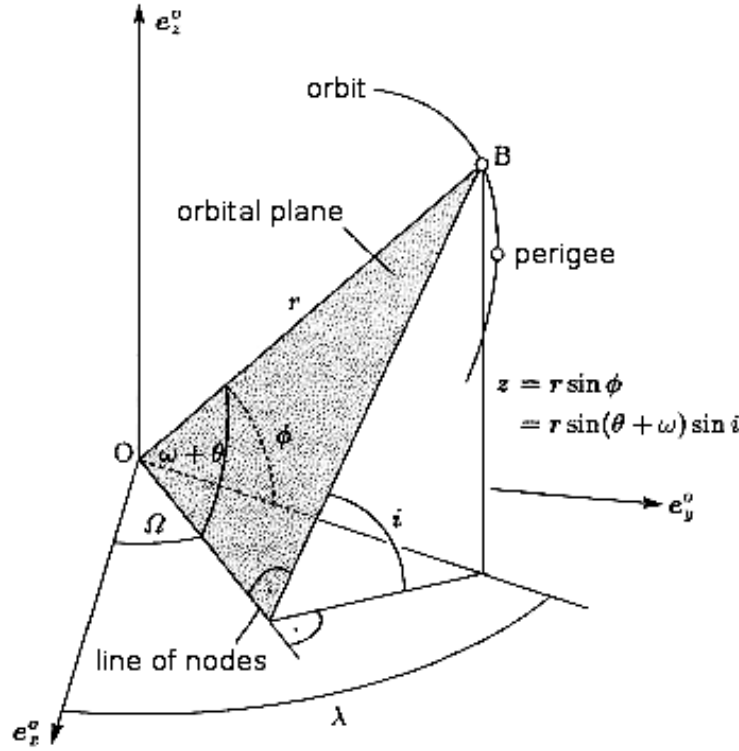
Figure 5.6: Trigonometric relations between the inclination i, the argument of perigee $u := \theta + \omega$ and the latitude φ according to Steiner & Schagerl (2004).

& Schagerl, 2004):

$$W_2 = V_2(r, \varphi) = -\frac{\mu}{r} J_2 \left(\frac{R_e}{r}\right)^2 \left(\frac{1}{2} - \frac{3}{2} \sin^2 \varphi\right) \tag{5.58}$$

It can be shown that $\sin \varphi = \sin(\omega + \theta) \sin i$ (see Fig. 5.6 and Steiner & Schagerl 2004, p. 124). Therefore the perturbation potential in terms of orbital elements reads:

$$W_2^* = -\frac{\mu J_2 R_e^2 (1 - e \cos \theta)^3}{a^3 (1 - e^2)^3} \left(\frac{1}{2} - \frac{3}{4} \sin^2 i + \frac{3}{4} \sin^2 i \cos(2\theta + 2\omega)\right) \tag{5.59}$$

where the geometrical relation $2 \sin^2(\theta + \omega) = 1 - \cos(2\theta + 2\omega)$ and Eq. (5.21) have been used.

Eq. (5.59) is based on the true anomaly θ instead of the mean anomaly M, which is needed for the Lagrange perturbation Eqs. (5.50) – (5.55). As explained in Sec. 5.2.3, the Kepler equation (5.28) cannot be solved with respect to E, thus there is no way to express E and, therefore, θ analytically in terms of M.

It is possible, though, to apply an averaging process to determine the *mean perturbation* effects on the satellite's orbit. The idea is to regard the satellite's motion as a quasi-static Kepler orbit and average the perturbation potential W^* over the time interval T that is needed for one revolution, i.e., one complete orbit around the Earth:

$$\bar{W}^*(a, e, i, \Omega, \omega) = \frac{1}{T} \int_0^T W^*(a, e, i, \Omega, \omega, M(t)) \, dt \tag{5.60}$$

Instead of integrating over the time $\int_0^T dt$ one can calculate the integral over the true anomaly for one revolution, i.e., $\int_0^{2\pi} d\theta$. The integration variables dt and $d\theta$ are related to each other through

Kepler's second law (5.14) and the following relations (Steiner & Schagerl, 2004, p. 126):

$$T = 2\pi \sqrt{\frac{a^3}{\mu}} \tag{5.61}$$

$$h = \sqrt{\mu a(1 - e^2)} \tag{5.62}$$

Therefore the relation between the integration variables is

$$\frac{1}{T} dt = \frac{r^2}{hT} d\theta = \frac{1}{2\pi} \left(\frac{r}{a}\right)^2 \frac{d\theta}{\sqrt{1 - e^2}} \tag{5.63}$$

Using the following integrals (Steiner & Schagerl, 2004, p. 126)

$$\frac{1}{2\pi} \int_0^{2\pi} \frac{1 + e\cos\theta}{1 - e^2} d\theta = \frac{1}{1 - e^2} \quad \text{and} \quad \frac{1}{2\pi} \int_0^{2\pi} \frac{1 + e\cos\theta}{1 - e^2} \cos(2\theta + 2\omega) d\theta = 0 \tag{5.64}$$

the average perturbation potential can finally be calculated as:

$$\begin{aligned}
\bar{W}_2^* &= -\frac{\mu J_2 R_e^2}{a^3 \sqrt{1 - e^2}} \frac{1}{2\pi} \int_0^{2\pi} \left(\frac{1 - e\cos\theta}{1 - e^2}\right)\left(\frac{1}{2} - \frac{3}{4}\sin^2 i + \frac{3}{4}\sin^2 i \cos(2\theta + 2\omega)\right) d\theta \\
&= -\frac{\mu J_2 R_e^2}{a^3(1 - e^2)^{3/2}}\left(\frac{1}{2} - \frac{3}{4}\sin^2 i\right)
\end{aligned} \tag{5.65}$$

The differential equations for the orbital elements can be obtained from Eqs. (5.50) – (5.55) by evaluating the derivatives:

$$\frac{\partial \bar{W}_2^*}{\partial a} = \frac{3}{2}\frac{\mu J_2 R_e^2}{a^4(1 - e^2)^{3/2}}\left(1 - \frac{3}{2}\sin^2 i\right) \tag{5.66}$$

$$\frac{\partial \bar{W}_2^*}{\partial e} = -\frac{3}{2}\frac{\mu J_2 R_e^2}{a^4(1 - e^2)^{5/2}}\left(1 - \frac{3}{2}\sin^2 i\right) \tag{5.67}$$

$$\frac{\partial \bar{W}_2^*}{\partial i} = \frac{3}{2}\frac{\mu J_2 R_e^2}{a^4(1 - e^2)^{3/2}}\sin i \cos i \tag{5.68}$$

The remaining three derivatives with respect to Ω, ω and M are zero, thus Eqs. (5.50) – (5.55) read:

$$\left(\frac{da}{dt}\right)_2 = 0 \tag{5.69}$$

$$\left(\frac{de}{dt}\right)_2 = 0 \tag{5.70}$$

$$\left(\frac{di}{dt}\right)_2 = 0 \tag{5.71}$$

$$\left(\frac{d\Omega}{dt}\right)_2 = -\frac{3}{2}\frac{\mu J_2 R_e^2}{na^5(1 - e^2)^2}\cos i \tag{5.72}$$

$$\left(\frac{d\omega}{dt}\right)_2 = \frac{3}{4}\frac{\mu J_2 R_e^2}{na^5(1 - e^2)^2}\left(4 - 5\sin^2 i\right) \tag{5.73}$$

$$\left(\frac{dM}{dt}\right)_2 = \frac{3}{4}\frac{\mu J_2 R_e^2}{na^5(1 - e^2)^{3/2}}\left(2 - 3\sin^2 i\right) \tag{5.74}$$

The index "2" means that the equations describe the change of the orbital elements due to the J_2 terms in the perturbation theory. Of course, additionally to the J_2 contribution the temporal change of M also has a contribution due to the motion of satellite itself. Therefore, the time derivative for M actually has an extra term $n = 2\pi/T$, which is not a result of perturbation theory, but anyhow can be combined with (5.74):

$$\frac{dM}{dt} = n + \left(\frac{dM}{dt}\right)_2 + \sum_{k=3}^{\infty} \left(\frac{dM}{dt}\right)_k \tag{5.75}$$

As the mean perturbation potential $\bar{W}^*$ does not depend on Ω, ω, and M, the three orbital elements a, e, and i are independent of time according to Eqs. (5.50), (5.51), and (5.52). This means that they are constant during the entire flight of the satellite, if only mean perturbation with J_2 contributions is considered. (For higher order perturbation theory or regarding W^* instead of $\bar{W}^*$, this is not valid.)

Solving the differential equations, perturbation theory up to order J_2 yields (Steiner & Schagerl 2004, p. 128, Keller 2002, p. 28):

$$\Omega(t) = \Omega_0 - \frac{3}{2}\frac{J_2 R_e^2}{p_0^2} n_0 \cos i_0 (t - t_0) \tag{5.76}$$

$$\omega(t) = \omega_0 + \frac{3}{4}\frac{J_2 R_e^2}{p_0^2} n_0 \left(4 - 5\sin^2 i_0\right)(t - t_0) \tag{5.77}$$

$$M(t) = M_0 + \left[n_0 + \frac{3}{4}\frac{J_2 R_e^2}{p_0^2} n_0 \sqrt{1 - e_0^2}\left(2 - 3\sin^2 i_0\right)\right](t - t_0) \tag{5.78}$$

with $n_0 = \sqrt{\mu/a_0^3}$ and $p_0 = a_0(1 - e_0^2)$ being the initial values at time t_0.

Taking a closer look at Eqs. (5.76) – (5.78), the mean J_2 perturbations cause a slow change of the three orbital elements Ω, ω and M. Additionally to the Keplerian motion of the satellite, the perturbation terms, e.g., alter the attitude of the orbital plane in 3-dimensional space, as Eq. (5.76) describes a precession of the line of nodes along the equator, which is displayed in Fig. 5.7. The reason for this effect is explained in Fig. 5.8: the equatorial bulge exerts a torque on the satellite's orbit. Therefore, the angular momentum vector performs a precession around the Earth's axis, which means a precessing line of nodes.

Additionally to the precession of the orbital plane, in first order perturbation theory the argument of perigee is not constant any more, and the mean anomaly is not only changing due to the mean motion n. However, the change of the orbital elements due to J_2 perturbations is much smaller than the change of M caused by the satellite's mean motion, e.g., the precession of the line of nodes $\dot{\Omega}_2$ is usually of the order of a few degrees per day (see Sec. 5.4). But, of course, this effect cannot be neglected for the prediction of a satellite's orbit over a period of more than a single revolution.

5.2.8 Secular and periodic variations

The exact calculation of perturbation effects is quite difficult due to the non-analytical relation between the mean anomaly M, which is needed for the Lagrange equations (5.50) – (5.55), and the true anomaly θ and eccentric anomaly E respectively, which describe the actual position of the satellite. This problems can be solved by regarding the orbital parameters a, e, i, Ω, and ω as constant during one revolution and taking the average perturbation potential $\bar{W}^*$ by integration (cf. Eq. (5.60)).
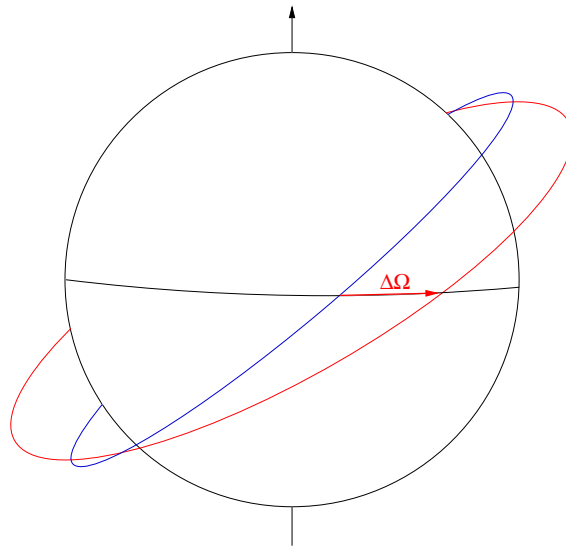
Figure 5.7: Precession of the orbital plane around the Earth's rotational axis due to orbit perturbation effects.
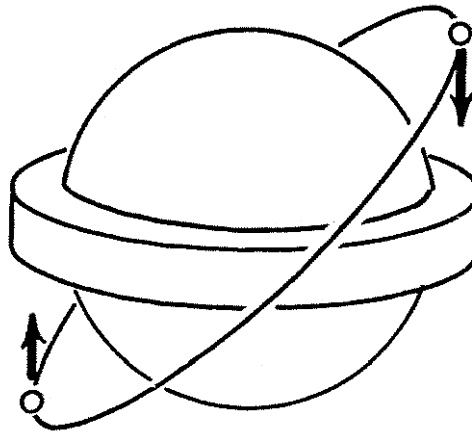
Figure 5.8: Equatorial bulge exerts a torque on the satellite's orbit (Bate et al., 1971).

This method results in a constant time derivative of the orbital elements (5.72) – (5.69). But due to the motion of the satellite around the Earth, it is exposed to the gravitational potential at different positions. Therefore, in general the perturbation potential W^* is not constant on the orbit. Actually it can be written as a combination of a mean potential and some short-term deviations:

$$W^* = \bar{W}^* + \Delta W^* \tag{5.79}$$

The periodicity of the satellite's orbit is transferred to the deviations ΔW^*. Therefore the change of the orbital parameters also has to be split in a constant part, which was calculated by the averaging method in section 5.2.7, and additional periodic contributions, which are more difficult to be calculated.

The different perturbation effects can be classified as *secular* (from the Latin word *saeculum*, which means century) perturbations, long period and short period variations (Keller, 2002, p. 26f.). A schematic superposition of the different perturbations is displayed in Fig. 5.9.
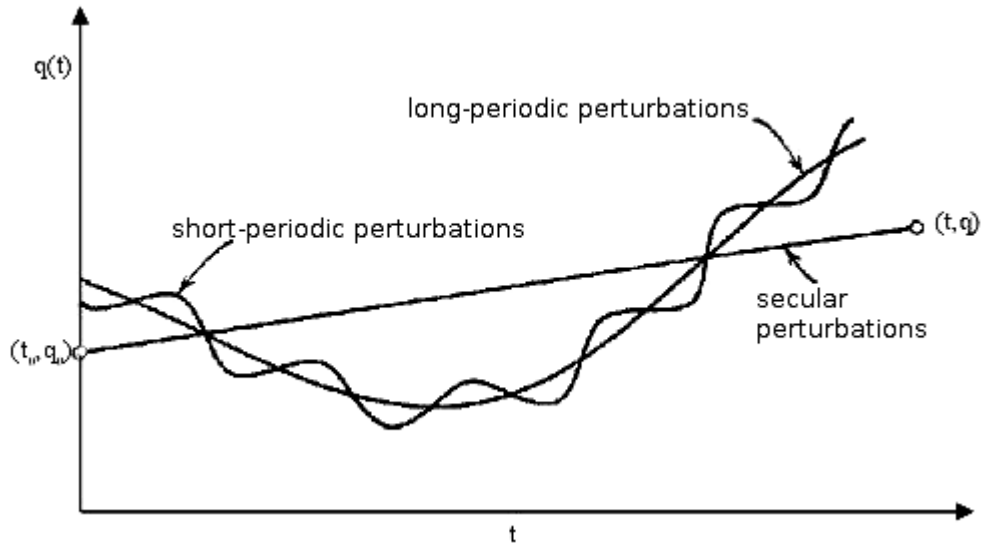
Figure 5.9: Superposition of different perturbation terms on the orbital parameter q (Keller, 2002): the total perturbation is a composition of secular, short, and long period effects.

According to Escobal (1965, p. 361f.) and Kozai (1959), the long period variations are caused by trigonometric functions of ω, whereas the short period variations are caused by trigonometric functions of the argument of latitude $u = \omega + \theta$. The difference in the period of these variations is caused by the fact that on the satellite's orbit the true anomaly θ is varying much faster between 0 and 2π than the argument of perigee, which is mainly changing due to secular variations. The true anomaly is sometimes referred to as a *fast variable*, whereas the first 5 Keplerian elements, namely a, e, i, Ω, and ω are called *slow variables* (Liu, 1974).

The total change of the orbital element q can be qualified as (Escobal, 1965, p. 362):

$$q = q_0 + \dot{q}_0(t - t_0) + K_1 \cos(2\omega) + K_2 \sin(2\theta + 2\omega) \tag{5.80}$$

where $\dot{q}_0$ is the secular change, and K_1 and K_2 are the amplitudes of the long and short period variations respectively.

5.2.9 Higher order perturbations

In the previous sections (particularly in Sec. 5.2.7) only contributions up to J_2 have been considered for the perturbation potential $W = V - V_0$. As the higher Jeffrey coefficients J_n, with $n > 2$, are at least about three magnitudes smaller than J_2, there are only very small differences between J_2 and higher order perturbation theory, as can be seen in Fig. 5.12. Therefore calculations including J_2 contributions are good enough to describe the evolution of the satellite's orbit qualitatively during a short span of time. But for closer examinations and accurate orbit predictions over several days, as required for the NRTA, higher order perturbation theory has to be applied.

The expansion of the gravitational potential given by Eq. (5.49) up to $n = 4$ yields additional terms with the coefficients J_2^2, J_3 and J_4. In this context the *order* of the perturbation theory is commonly defined in the following way: all terms that contain only first order factors of J_2 are summarized as *first order* terms. The contributions to the perturbation potential with J_2^2, J_3, or J_4 factors are denoted as *second order* due to their magnitude (Escobal, 1965, p. 366).

As can be seen from the explicit calculation of the perturbation contributions, the first order coefficient J_2 mainly results in secular and short period variations, whereas the second order terms

J_2^2, J_3, and J_4 have noticeable effects on long period oscillations of the orbital elements (see Kozai 1959).

As the determination of the higher order perturbation contributions is quite lengthy, the results, which can be found, e.g., in Flury (1991), Klinkrad (1983), Liu (1974), or Liu & Alford (1979), are used in this text without explicit derivation. The explicit form of these terms is given in Appendix A. The interested reader may take a look at Brouwer (1959) or Kozai (1959) for the relevant mathematical background.

Using the formulas for the time derivatives of the mean orbital elements $\dot{q}$ (secular + long period variations) and the short period oscillations Δq for $q \in \{a, e, i, \Omega, \omega, M\}$, one can calculate the set $\{q(t)\}$ at the required time t from the initial orbital elements $\{q_0\}$ at t_0 by integration:

$$q(t) = q_0 + \int_{t_0}^{t} \dot{q}\, dt + \Delta q \tag{5.81}$$

In general $\dot{q}$ depends on the slow variables a, e, i, Ω and ω. The fast variable M is eliminated from $\dot{q}$ by using the mean perturbation potential $\bar{W}^*$ instead of W^*. Anyhow, the integration in Eq. (5.81) cannot be done analytically, as the slow variables are time-dependent, too. The numerical solution for this problem is to regard the slow variables as constant over a short time interval Δt (e.g., $\Delta t \approx 1\,\mathrm{s}$) and to perform the integration in an iterative process:

$$\bar{q}(t + \Delta t) = \bar{q}(t) + \dot{q}\left(\{\bar{q}(t)\}\right) \cdot \Delta t \tag{5.82}$$

$$q(t + \Delta t) = \bar{q}(t + \Delta t) + \Delta q\left(\{\bar{q}(t + \Delta t)\}\right) \tag{5.83}$$

Knowing $q(t)$, the position and velocity of the satellite, $\mathbf{r}(t)$ and $\mathbf{v}(t)$ respectively, can be calculated easily using the formulas in Sec. 5.2.3.

5.2.10 Singularities for small eccentricity

Taking a closer look on the perturbation terms in Appendix A, there are some expressions with the eccentricity e in the denominator. As a result, for $e \to 0$ the corresponding quantities become singular. For the secular and long period variations the J_3 terms of $\dot{\omega}$ and $\dot{M}$ are affected by this problem.

Considering the actual meaning of these two Keplerian orbital elements, the reason for the divergences is quite obvious: in the special case $e = 0$ the satellite's orbit is a special kind of ellipse, namely a circular orbit. As a circle has no perigee, there is no way to define the argument of perigee ω. In the same way the true anomaly becomes undefined. The divergences of $\dot{\omega}$ and $\dot{M}$ are, therefore, just a mathematical but not a physical problem. As the position and velocity of the satellite are still well defined even on a circular orbit, the sum $\dot{\omega} + \dot{M}$ should be finite for $e = 0$ (Henrard, 1974).

In fact, the explicit calculation exhibits that the J_3 contribution to this sum still contains the eccentricity e in the denominator. But due to the particular form of the enumerator the limit is well defined:

$$\lim_{e \to 0} \left(\dot{\omega} + \dot{M}\right)_{J_3} = 0 \tag{5.84}$$

That means that the mathematical description of orbits using Keplerian orbital elements is inapplicable for small eccentricity, and therefore a different way has to be found to determine the position of the satellite. Fortunately, small modifications of the theory introduced above are sufficient to make it suitable even for $e \to 0$. There are two similar approaches to avoid divergences for small eccentricity and additionally for small orbit inclinations. The basic idea is a transformation to a different set of orbital elements, as, e.g., explained by Kozai (1959) or Lyddane (1963). One

disadvantage of the presented methods is that the perturbation potential still is given in Keplerian orbital elements. For each calculation step the alternative set of orbital elements has to be transformed back to Keplerian orbital elements to obtain the perturbation terms for the next step, which results in additional computation time. A further transformation was introduced by Hoots (1981), which should avoid this transformation problem.

As the orbit of Spectrum-X-Gamma has nearly no eccentricity, it is important to choose one of these transformations to avoid divergences at the numerical integration of the orbital elements (Eqs. 5.82 and 5.83). The inclination of $i \approx 30°$ does not cause any problems. Therefore, the following transformation, proposed by Flury (1991), was chosen to handle the low-eccentricity contributions in perturbation theory. It follows the approach of Kozai (1959) and Lyddane (1963):

$$h := e \cos \omega \qquad (5.85)$$

$$k := e \sin \omega \qquad (5.86)$$

$$u' := \omega + M \qquad (5.87)$$

Here the quantity u' is used instead of the argument of latitude $u = \omega + \theta$, as the perturbation term $\dot{M}$ is well known in contrary to $\dot{\theta}$. The numerical effort of this implementation is kept as small as possible by optimization of the necessary calculations.

It turns out that the limits of h, k and u' for $e \to 0$ are indeed finite. Therefore, the calculation of the perturbation terms for the orbit propagation according to Eqs. (5.82) and (5.83) is well defined for the parameter set (a, i, Ω, h, k, u'). To determine the satellite's position and velocity using the formulas in Sec. 5.2.3, the variables h, k and u' are transformed back to e, ω and M. The numerical effort for this latter transformation is negligible in comparison to the calculation of the perturbation terms $\dot{q}$ and Δq. In contrast to the method of Hoots (1981) this algorithm was given in more detail. Therefore, the negligible effort for the additional transformation is accepted with regard to the reliability of the procedure.

The mathematical terms used for the calculation of perturbation effects on this new parameter set are summarized in Appendix A, as they are not explicitly displayed in the required form in any of the references cited above.

5.3 Implementation

The orbit calculation is implemented in a separate program which creates an orbit file as input for the measurement simulation. The format of the orbit file is described in Sec. 4.3.5. In order to obtain the satellite's position and velocity as exact as possible, perturbation theory up to second order, i.e., with contributions from J_2, J_2^2, J_3, and J_4 has been applied.

For testing purpose a similar algorithm with first order perturbation theory was implemented, which is based on the formulas in Eqs. (5.76), (5.77), and (5.78). Although this algorithm is no capable of computing small orbit variations, and is, therefore, not usable for long term calculations, the code is quite simple and the satellite's orbit, except from periodic variations, can be determined for one or a few revolutions with a limited degree of accuracy. For the actual simulation second order perturbation theory was applied, so only this latter method is explained in detail in the following.

The most important input parameters for the orbit calculations are the initial set of Keplerian orbital elements $(\bar{a}_0, \bar{e}_0, \bar{i}_0, \bar{\Omega}_0, \bar{\omega}_0, \bar{M}_0)$ at the start time t_0, the calculated span of time, and the iteration step width Δt. From these values the necessary data for the calculation can be obtained, and the iterative computation of the orbit data according to the previously mentioned mathematical methods is performed.

Starting with the initial parameter set $\{\bar{q}_0\}$ of Keplerian orbital elements, the iteration step $t \rightarrow t+\Delta t$ is performed according to Eq. (5.82) with $\dot{q}$ given by the formulas in Appendix A.1. The critical parts of $\dot{q}$ that might be divergent for $e \rightarrow 0$ and originate especially from J_3 contributions are calculated in terms of the alternative set of orbital elements h, k, u' and afterwards transformed back and added to the Keplerian elements e, ω, M. More information about this method and the explicit formulas is given in the appendix. In a similar way as the secular and long period changes of the orbital elements the short period variations are determined according to Eq. (5.83) with Δq given in Appendix A.2.

To obtain the orbit over the entire span of time, the previous calculations are repeated continuously: first the secular and long period iteration of the Keplerian orbital elements is performed ($\{\bar{q}(t)\} \rightarrow \{\bar{q}(t + \Delta t)\}$), then the short period variations are added. The latter ones are only important for the determination of the satellite's current position, but they do not contribute to the perturbation terms $\dot{q}$ or Δq, i.e., the short period variations have no impact on the secular or long period orbit evolution. But, of course, the short period terms Δq are affected by $\bar{q}$.

For the output of the satellite's position and velocity to the generated orbit file these quantities have to be calculated in Cartesian coordinates according to Eqs. (5.30) and (5.32). For that purpose the Kepler equation (5.28) has to be solved to obtain the eccentric anomaly E and finally the true anomaly θ. With θ the position and velocity can be determined by trigonometric calculations.

5.4 Verification

Several checks have been performed in order to verify the output of the orbit propagation algorithm. Besides comparison of the calculated orbits to values from literature, the program has been run with parameters of the **R**ossi **X**-ray **T**iming **E**xplorer (RXTE) satellite, which is actually in space, and the resulting data have been compared to the available orbit files.

5.4.1 Ground track

As the orbit files that are created by the eROSITA orbit propagation program have the common file format, standard orbit visualization tools can be applied to obtain graphical output for the generated orbits. In order to illustrate the eROSITA orbit and to verify the implemented algorithm, an **I**nteractive **D**ata **L**anguage (IDL) routine written by Felix Fürst (Dr.Remeis-Sternwarte) was used to create a picture of the ground track during 2 revolutions. It is displayed in Fig. 5.10.

The effects of perturbation theory are not noticeable for this short period, so basically the orbit consists of two circular revolutions around the Earth. Due to the rotation of the Earth during the time span of 96 min, which is needed for one revolution, the ground track is not a closed line.

5.4.2 Change of orbital elements

For the program verification the perturbation effects in the orbit determination can be restricted to J_2 terms (Sec. 5.2.7). The resulting temporal changes of the orbital elements can be compared with values from literature or with analytically determined quantities, according to Eqs. (5.76) – (5.78) (see, e.g., Bate et al. 1971, p. 157f., Keller 2002, p. 29f., Flury 1991, p. 75f., Steiner & Schagerl 2004, p. 128).

The computational results for $\Delta\Omega$/day and $\Delta\omega$/day in Fig. 5.11 can be compared to the analytical values obtained from Eqs. (5.76) and (5.77) as well as to the figures in Bate et al. (1971, p. 157f.). (In this section Δq does not designate a short period perturbation, but a difference in the parameter q after a specific interval.) The perturbation effects for some real satellites given in Keller (2002, p. 30) can also be reproduced by the orbit calculation program, as shown in
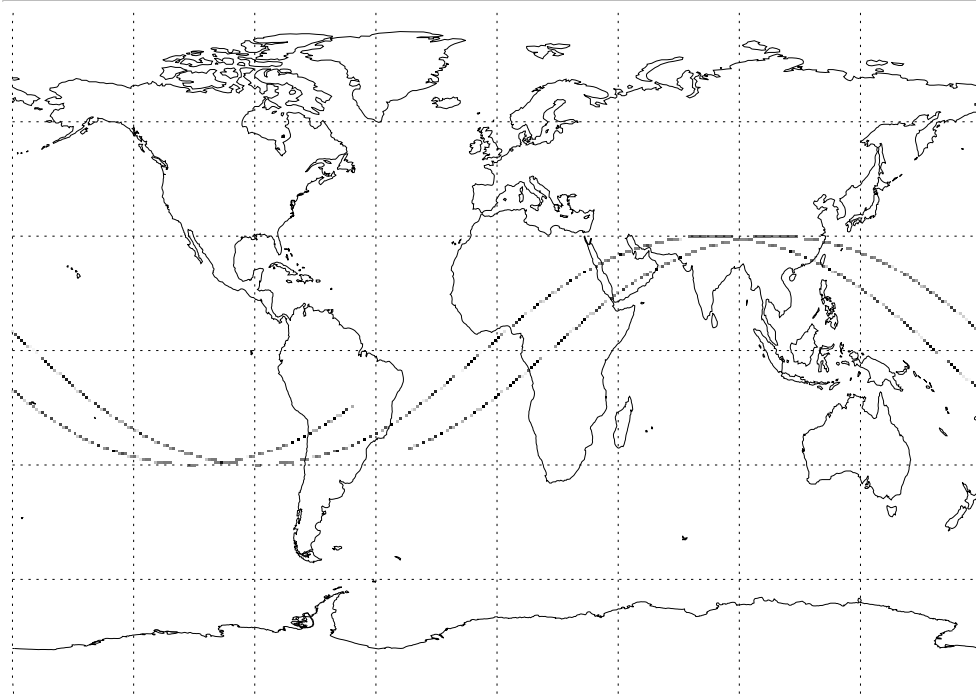
Figure 5.10: Ground track of eROSITA orbit.

Table 5.2: Comparison of the secular perturbation effects determined by the calculation program with the data of real satellites taken from Keller (2002, p. 30).

satellite	Iridium	Globalstar	ICO	GPS
a [km]	7158.173	7782.173	16732.173	26562.173
e	0	0	0	0
i [°]	86.4	52	45	55
T [min]	101	114	360	718
J_2 **perturbations according to Keller (2002)**				
$\Delta\Omega$/day	-0.4178	-3.0519	-0.2409	-0.0388
$\Delta\omega$/day	-3.2612	2.2188	0.2556	0.0218
J_2 **perturbations according to orbit calculation program**				
$\Delta\Omega$/day	-0.4178	-3.0574	-0.2409	-0.0388
$\Delta\omega$/day	-3.2612	2.2228	0.2556	0.0218
J_2**,** J_3 **+** J_4 **perturbations according to orbit calculation program**				
$\Delta\Omega$/day	-0.4165	-3.0585	-0.2410	-0.0388

Table 5.2. These comparisons exhibit a very good agreement of the calculated orbit data with the values obtained from the different independent sources. Although only J_2 contributions are considered in the presented computations, this may anyhow confirm the correct implementation of the orbit propagation algorithm.

As pointed out in Sec. 5.2.10, the argument of pergee ω is not well defined for orbits with low eccentricity $e \approx 0$. For these orbits one has to regard the argument of latitude u instead.

The change of the argument of perigee $\Delta\omega$ cannot be calculated for the zero-eccentricity orbits in Table 5.2 by the second order algorithm, so for second order perturbation theory the corresponding row for $\Delta\omega$ is missing in the table. As first order perturbation theory contains no $1/e$ terms, there are no divergences, and the quantity $\Delta\omega$ can be specified for this method.

Taking a closer look at Table 5.2, the data for second order perturbation theory have more aberrations from the satellite data given by Keller (2002) than the first order perturbation theory. In contrary the comparison of the data of RXTE in Sec. 5.4.3 and particularly in Fig. 5.16 exhibits a better agreement with the second order perturbation theory than with first order. This fact suggests that the actual satellite data in Table 5.2 were probably obtained for only J_2 contributions, which would explain this discrepancy.

The plots in Fig. 5.12 verify the statement from Sec. 5.2.9, that there is almost no noticeable difference in the secular change of the orbital elements based on first and second order perturbation theory due to the difference of about 3 magnitudes in J_2 vs. J_3 and J_4.

5.4.3 Comparison with RXTE

The most obvious way to verify the proper orbit prediction is to compare the calculations of the algorithm with the actually measured orbit data of a true satellite. For this purpose orbit files of RXTE have been analyzed, and the contained orbit positions and velocities have been transformed to Keplerian orbital elements. The RXTE satellite is quite suitable for a verification of this algorithm, because it also has a close Earth orbit $a \approx 6956\,\mathrm{km}$ with a low eccentricity $e \approx 0.0008$ and an inclination of $i \approx 23°$. Therefore its orbit is quite similar to the eROSITA orbit.

The determination of the orbital elements includes perturbation effects with J_2, J_3, and J_4 contributions and starts at $t_0 = 0\,\mathrm{Ms}$. (In this section all time values refer to t_0.) As the following Figs. 5.13 and 5.14 show for some of the Keplerian orbital elements, the actual deviation between the predicted and the true orbital elements keeps within an acceptable range.

The deviations of the semimajor axis a, e.g., lie in a range of $\pm 0.005\%$, i.e., they are quite negligible. The right ascension of the ascending node Ω is also predicted quite precisely. Figs. 5.13 and 5.14 also show that even after a timespan of $5\,\mathrm{Ms} \approx 58\,\mathrm{days}$ the semimajor axis a still is determined quite well, whereas the calculated value of Ω deviates from the proper value for about 0.4%.

Although the aberration of Ω and also of the remaining angles like the inclination is quite small, the deviations of the individual angles sum up to a considerable deviation in the calculation of the actual position. Figs. 5.15 and 5.16 show that the implemented orbit prediction methods are only applicable over a time span of a few days. Some of these deviations may also be caused by different initial parameters $\{\bar{q}_0\}$ for the orbit propagation algorithm and the RXTE orbit. The orbital elements of RXTE are not provided by the orbit files, but had to be obtained from a fit to the given orbit. The short period oscillations in the distance, which are displayed in Fig. 5.16, also suggest that the fit of the Keplerian elements to the initial parameters of RXTE might have a better solution. Therefore, there might be a possibility to improve the agreement of both orbits. Anyhow the orbit prediction accuracy of about $\pm 30\,\mathrm{km}$ over short periods is sufficient for the current purpose of the simulation. For the NRTA, predictions over a longer period are usually not necessary.
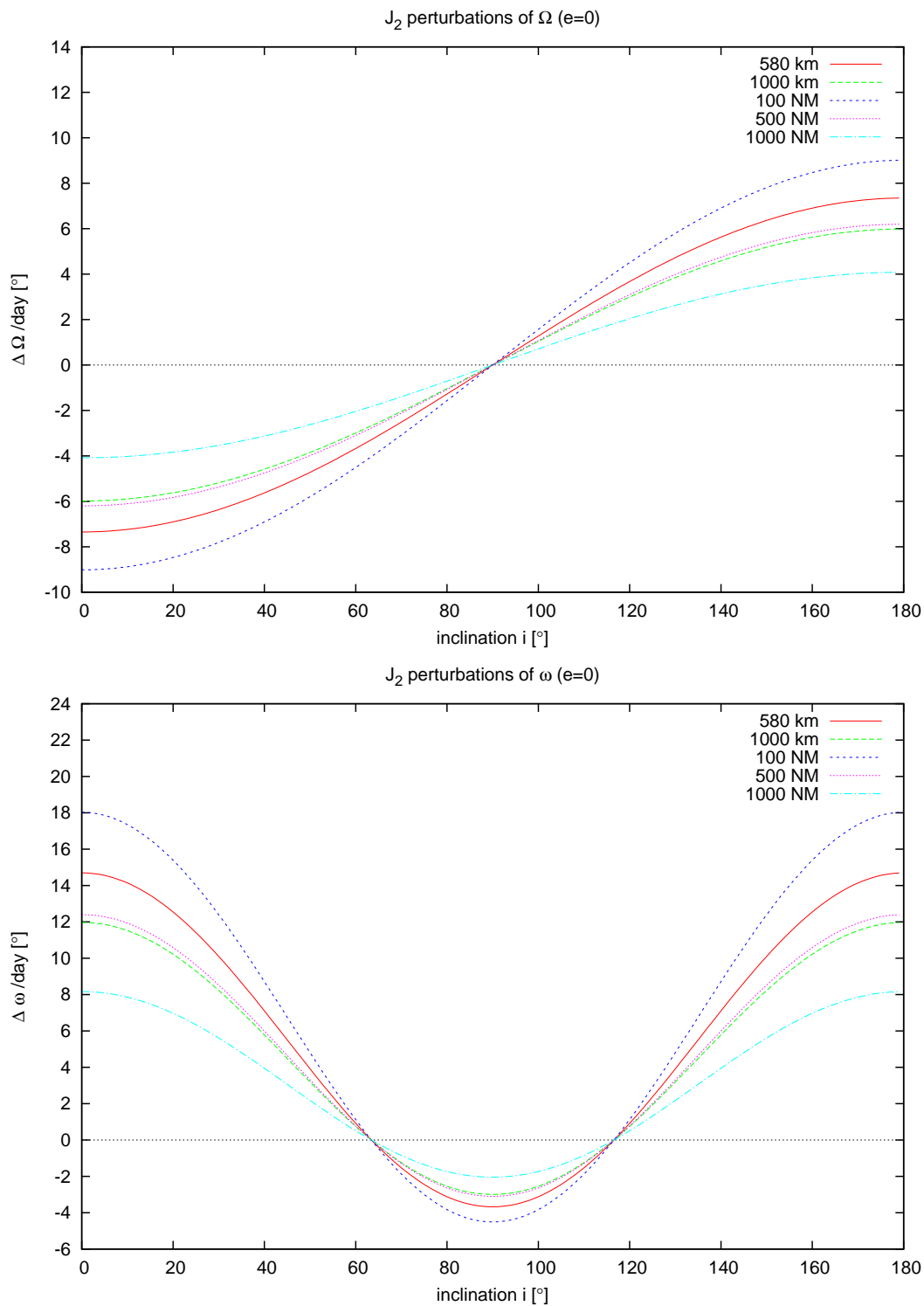
Figure 5.11: Secular change of the right ascension of the ascending node and the argument of perigee respectively per day in dependence on the orbit inclination, due to mean J_2 perturbation theory.
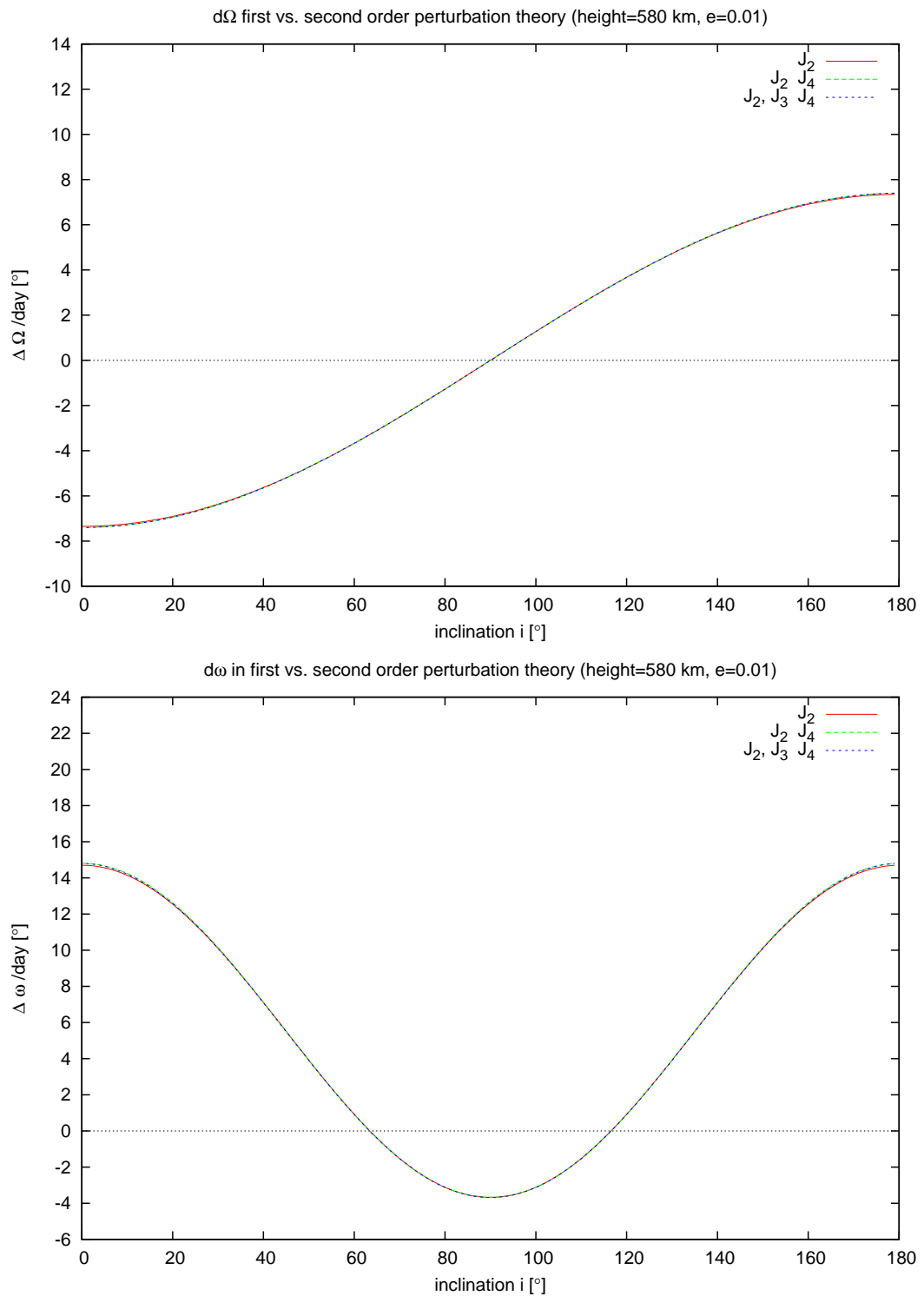
Figure 5.12: Secular change of the right ascension of the ascending node and the argument of perigee respectively per day in dependence on the orbit inclination, regarding perturbation theory with different combinations of Jeffrey coefficients J_n.
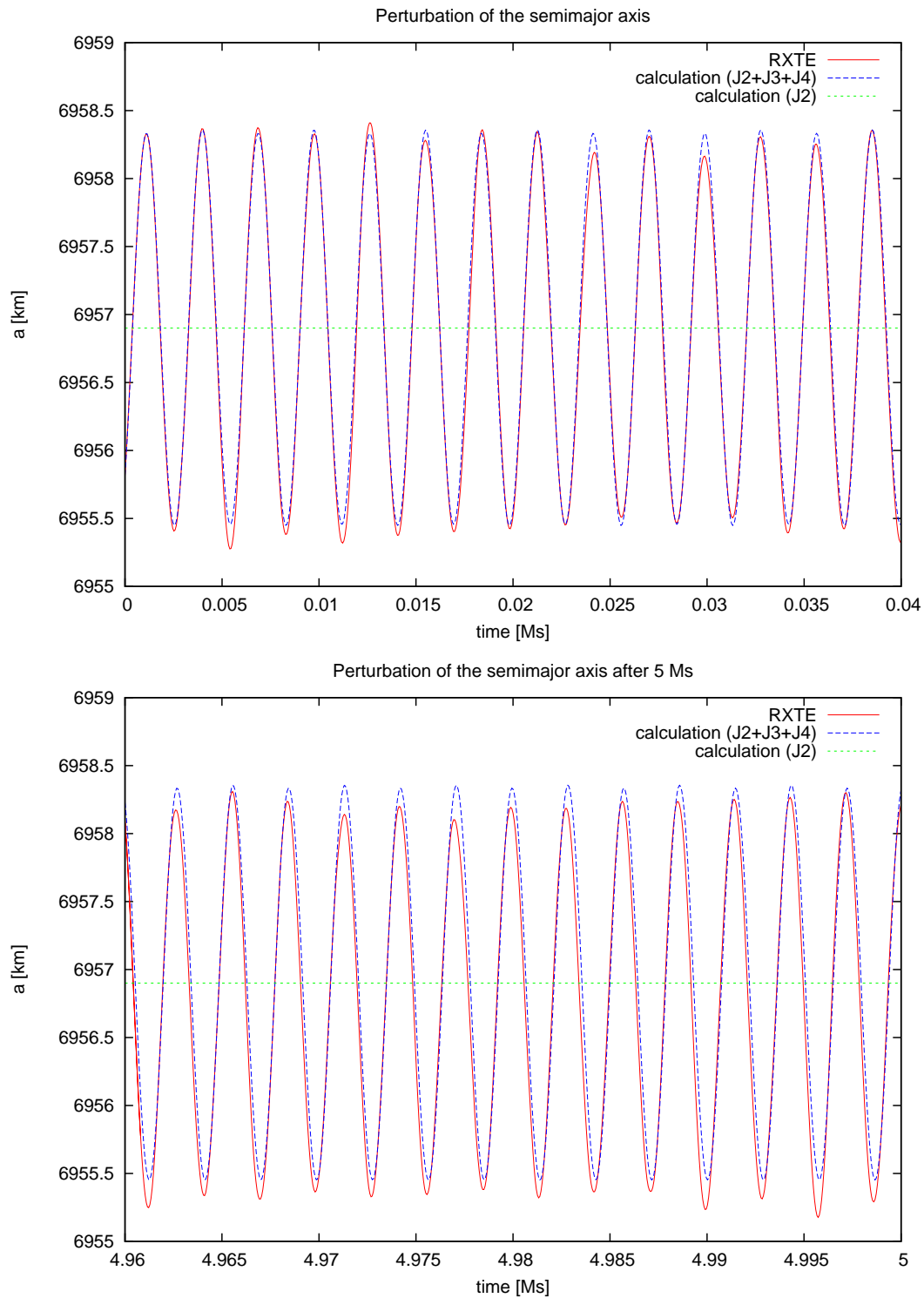
Figure 5.13: Comparison of the calculated data to the actual semimajor axis a of RXTE at t_0 and after 5 Ms respectively.
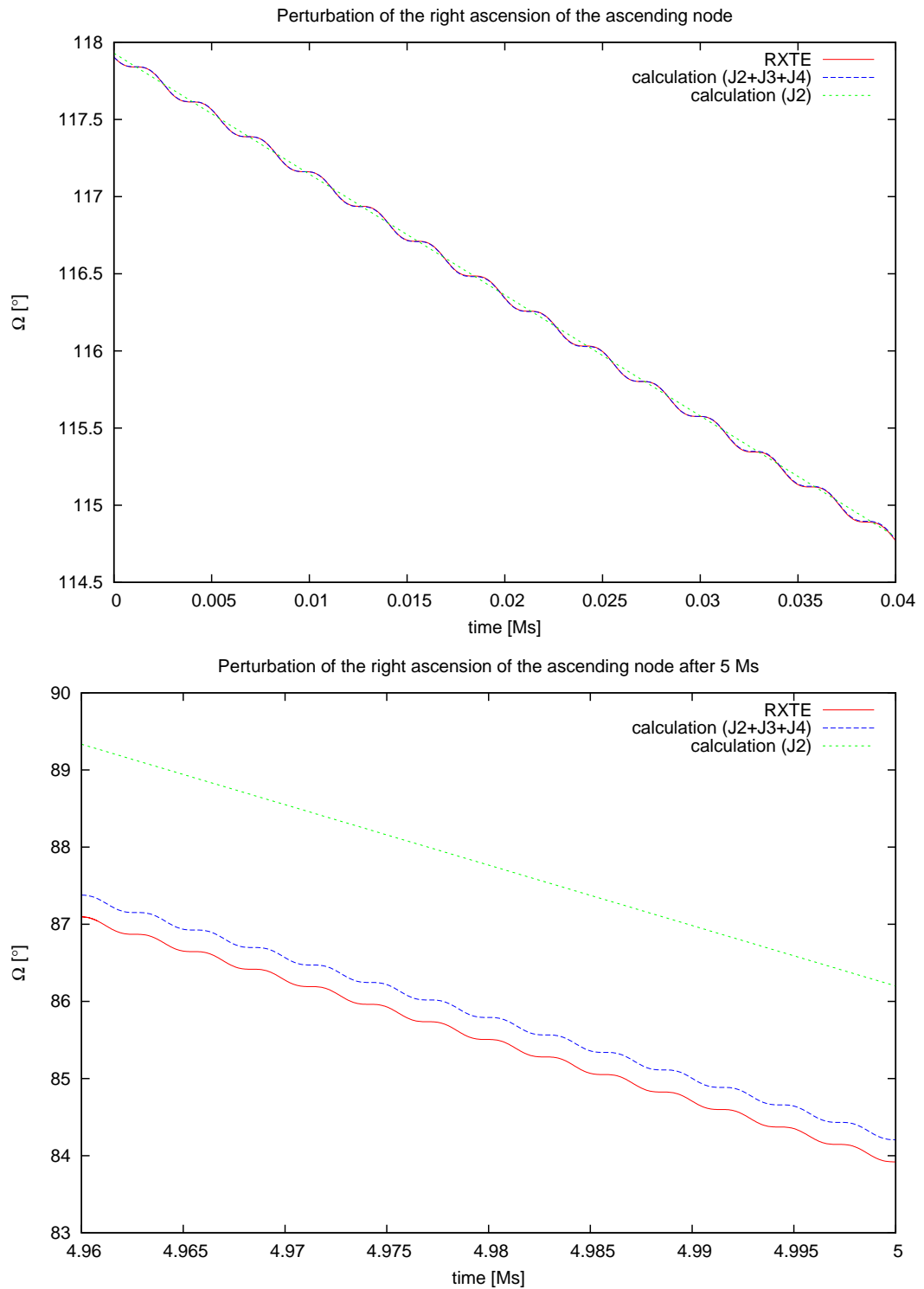
Figure 5.14: Comparison of the calculated data to the actual right ascension of the ascending node Ω of RXTE at t_0 and after 5 Ms respectively.
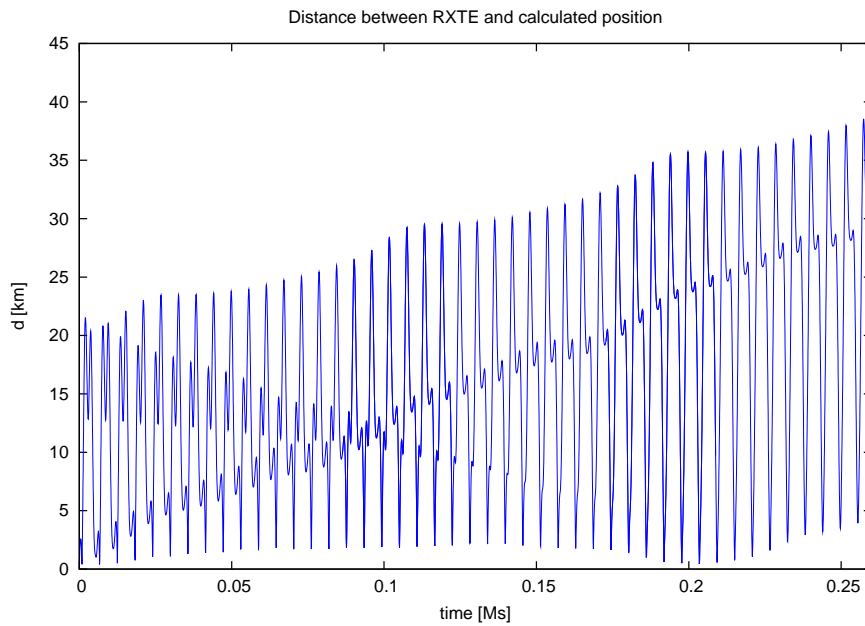
Figure 5.15: Evolution of the distance between the calculated and the RXTE satellite position during a period of 3 days.
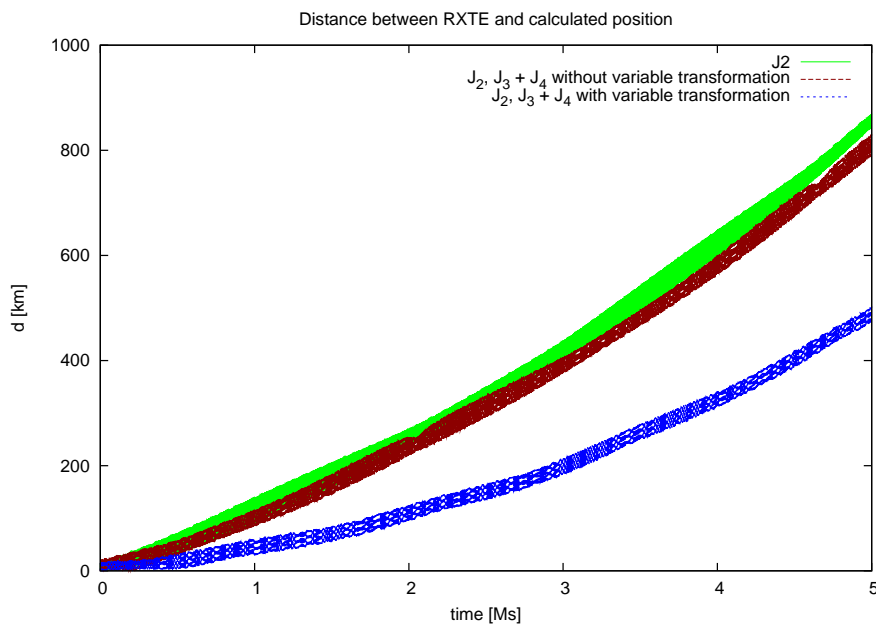
Figure 5.16: Evolution of the distance between the calculated and the RXTE satellite position during a period of 5 Ms. The second order perturbation theory has been performed twice in different ways. The first time the calculation of the perturbation terms was based Keplerian orbit elements, whereas the second time the variable transformation according to Kozai (1959) and Lyddane (1963) was implemented. The orbit of RXTE has a very small eccentricity, so the latter calculation method results in a much better agreement with the actual orbit of the satellite.

Chapter 6

Simulation results

This chapter will give some general results obtained from the simulation. Many data have already been presented in the context of previous chapters. Especially some light curve and spectra measurements are shown in Chap. 4, where the corresponding algorithms are treated. The data in this chapter are more general and do not fit into a particularly one of the previous chapters.

6.1 PSF effects

In Sec. 4.2.4 the PSF of the eROSITA mirror system was introduced. According to Peter Friedrich's simulations the PSF has a particular shape and, therefore, some characteristic effects on the measured data. This section will present some data from the simulation that demonstrate these features.

Of course, the energy dependence of the mirror reflectivity, which is displayed in Fig. 4.20, has an impact on the measurement of source spectra. The higher the photon energy, the more photons get lost at the reflection in the mirror system. For example, a source spectrum with constant count rate for the different energy bands will result in a measurement with decreasing count rate in the higher PHA channels. This effect can be actually observed for the simulation and is displayed in Fig. 6.1.

At the current state of the simulation, the model of the PSF as a function of δ and E has a step function like shape, whereas, of course, the real PSF is continuous. The step features in the simulation are caused the fact, that so far there is no proper interpolation for intermediate off-axis angles or photon energies. As there is only simulated PSF data available for some discrete values of δ and E (see Sec. 4.2.4), the current model results in the observed step function. This aspect will be improved at one of the next development steps.

The visualization of a sample data set from a pointed observation with three sources close the optical axis is displayed in Fig. 6.2. As the measurement was performed without detector background noise, the effects of the PSF can be clearly seen in this plot: each of the three peaks is extended over several neighboring detector pixels, and there are also several additional events outside the main peaks due to scattered photons. As the image displays a detector section around the center of the detector, except for some neglegible spread the peaks are quite sharp due to the high quality of the eROSITA PSF for on-axis sources.

At the border of the FOV the PSF becomes worse, as can be concluded from Fig. 6.3, which shows the measured photons for several sources aligned on two lines through the center of the detector: one parallel to the detector's y-axis and one diagonal line. The photons on the optical axis are focused to a very limited number of about 4 pixels, whereas for larger off-axis angle δ the photons are spread over a wide range of several pixels, i.e., the detected events are not located
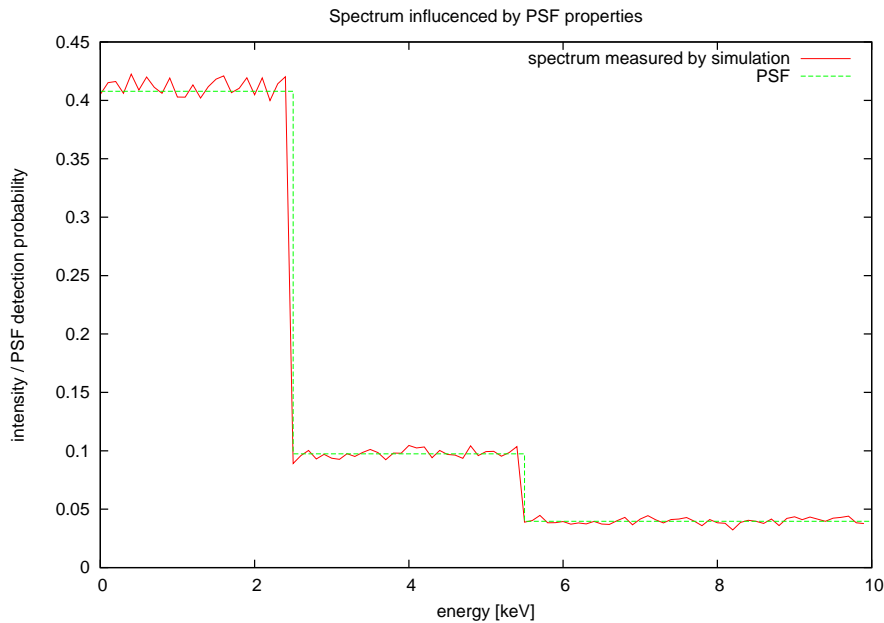
Figure 6.1: Effect of the energy dependence of the PSF on a measured spectrum for a simulated on-axis source with flat input spectrum (equal photon count rate for all PHA channels at 1 keV, 4 keV, and 7 keV respectively): the absolute detection probability of the PSF is reproduced. (For the displayed measurement an ideal detector has been assumed, i.e., with quantum efficiency = 1.) As the mirror properties become worse for higher photon energies, the fraction of photons that are really imaged onto the detector decreases for higher PHA channels. The step function like shape of the PSF is caused by the fact, that the mirror reflection simulation has only been performed for three discrete values E_j so far. Of course, the real PSF is a continuous function of δ and E, and not a step function. The shape of the PSF can be easily improved by further simulations or more complex interpolation for intermediate photon energies E_j.
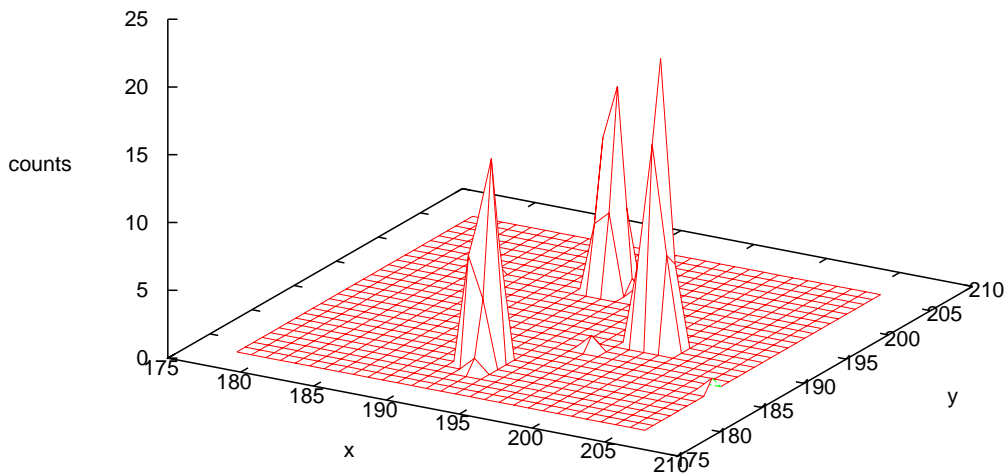
Figure 6.2: Sample measurement for a pointed observation with three sources close to the telescope axis (without detector background noise): the counts per detector pixel are displayed for a small section of the detector close to its center. Due to the PSF the three main peaks have a final extension, and there are some additional single events outside the main peaks caused by scattered photons.
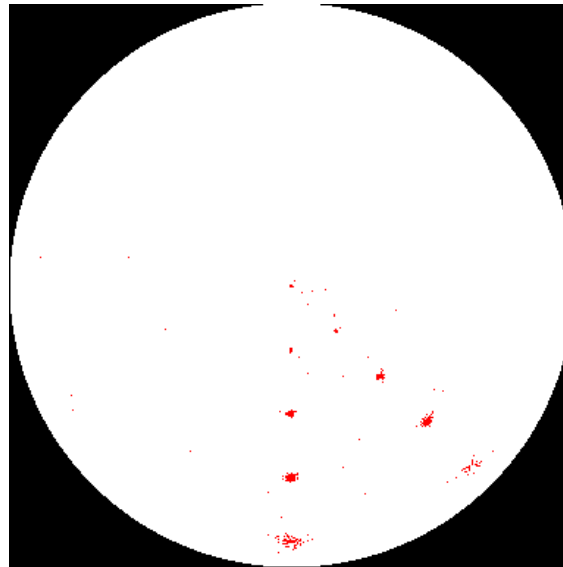
Figure 6.3: Sample measurement simulation with photons originating from several bright sources aligned on two lines (without detector background noise): the white circle marks the FOV and the red points represent single photon events. The source images close to the center of the detector are quite sharp, whereas the photons are widely spread for sources close to the border of the FOV.

directly on the vertical and diagonal line respectively.

6.2 Detector effects

To point out the effects of the detector response on the measured photon energies, a source with a constant spectrum was observed in a long-time pointed observation. The result is displayed in Fig. 6.4. Due to the energy dependence of the PSF model the constant input spectrum has a step function like shape after reflection of the generated photons on the mirror shells. This property has been discussed previously in Sec. 4.2.4 and Sec. 6.1.

As the detector response function is not a linear relation between the incident photon energy and the measured PHA channel, the finally measured spectrum is even more altered. The EPIC detector response matrix shown in Fig. 4.24 has significant features and side peaks for low energies, and the photons below ≲ 1 keV tend to be measured at lower energy than they actually had. This additional feature besides the PSF effects can be clearly seen in the finally measured spectrum in Fig. 6.4.

For higher energies the relation between photon energy and measured PHA channel is approximately linear. Therefore, in this region the spectrum of measured energies is basically equal to the spectrum of photons after the reflection in the mirror system.

6.3 Exposure time

In order to point out the effects of the integration time, two detector images can be compared in Fig. 6.5, which have been taken with exposure times of 10 ks and 100 ks respectively. The image with the longer exposure time contains additional sources that cannot be identified in the other picture. Of course, the background radiation is higher for the longer integration time, but the logarthmic intensity scale of the pictures also has to be taken into account.
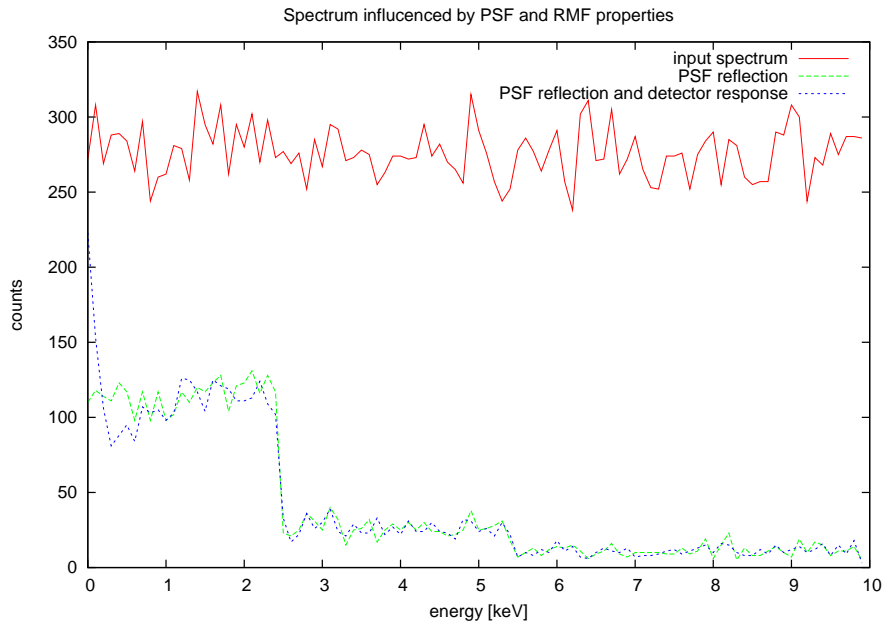
Figure 6.4: A constant input spectrum of photons is reflected by the mirror system and finally measured by the CCD detector according to the RMF of the EPIC. The particular properties of the PSF and the RMF have characteristic effects on the spectrum: due to the energy dependence of the PSF less photons are detected for higher energies than for lower energies. For the latter (with energy ≤ 1 keV) the RMF with its particular features, which are displayed in Fig. 4.24, results in a shift of some events to even lower PHA channels. This effect can be clearly seen in the spectrum. The simulation was performed for infinitely small charge cloud size, so there are no split events.

The analysis of the detector images may be improved by using adequate software tools, e.g., for subtraction of the background events. But even from these simple pictures one can see the additional sources that become visible after a longer exposure time.

6.4 Scanning the sky

The primary goal of the simulation is the generation of event files for the all-sky survey of eROSITA. Many of the previously presented results have been obtained from pointed observations of very bright sources, as this situation is more convenient for measuring, e.g., the light curve of a source during a longer period. In order to analyze a source spectrum, it is also important that the source remains at a fixed position in the FOV. Otherwise the spectrum would be influenced by the position dependency of the PSF, which has different ratios of imaging probabilities for the individual energy bands at different off-axis angles (cf. Sec. 4.2.4).

But, of course, the simulation is actually designed for the implementation of the all-sky survey. The pictures in Fig. 6.6 are taken from this scenario and display the images of several sources at particular points of time during the scan over the sky. The telescope axis is moving according to the satellite's orbit such that for an observer fixed to the telescope axis the sources seem to be wandering through the FOV with a velocity of

$$\frac{384\,\text{pixel}}{61.9'} \cdot \frac{360°}{96 \cdot 60\,\text{s}} \approx 23\,\text{pixel}\,\text{s}^{-1} \tag{6.1}$$

This point of view is adopted in the following.
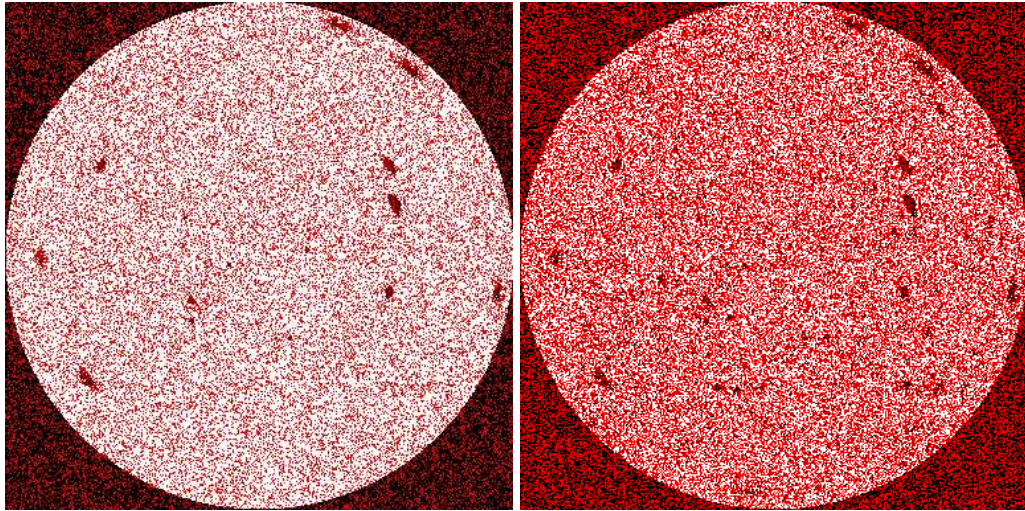
Figure 6.5: Comparison of different exposure times: the left image was taken with an exposure time of 10 ks, the right with 100 ks. The images display the photon counts in the individual pixels for pointed observations in a logarithmic scale. The detector background count rate was set to 0.00015 counts s^{-1} pixel^{-1}. Several weak sources that are not visible in the left image can be seen in the right one due to the longer integration time.

Observing the highlighted source on its path through the FOV, clearly reveals the particular properties of the modelled eROSITA PSF, which is much sharper at the center than a the edge of the FOV (cf. Sec. 4.2.4). This spread can be very well seen in Fig. 6.7, too, which is a detector image taken with an integration time of 60 s. Due to this long exposure time and the motion of the telescope axis the individual point sources are smeared to stripes over the entire width of the FOV with a particularly wide photon spread at the edges.

The satellite's orbit has a period of about 96 min and the FOV has a diameter of 61.9′, so the time for a transverse passage of a source through the FOV can be determined according to

$$t_{\text{passage}} = \left(\frac{61.9}{60}\right)^{\circ} \cdot \left(\frac{360°}{96 \cdot 60 \text{ s}}\right)^{-1} \approx 16.5 \text{ s} \tag{6.2}$$

which matches the observed passage time for the highlighted source in Fig. 6.6. Of course, t_{passage} is a maximum value, only valid for sources passing through the center of the FOV. For sources at the edge of the FOV the interval of visibility is usually shorter.

Regarding the motion of source images on the detector, the implementation of the motion of the telescope axis on the satellite's orbit during the simulation of the all-sky survey seems to work properly.
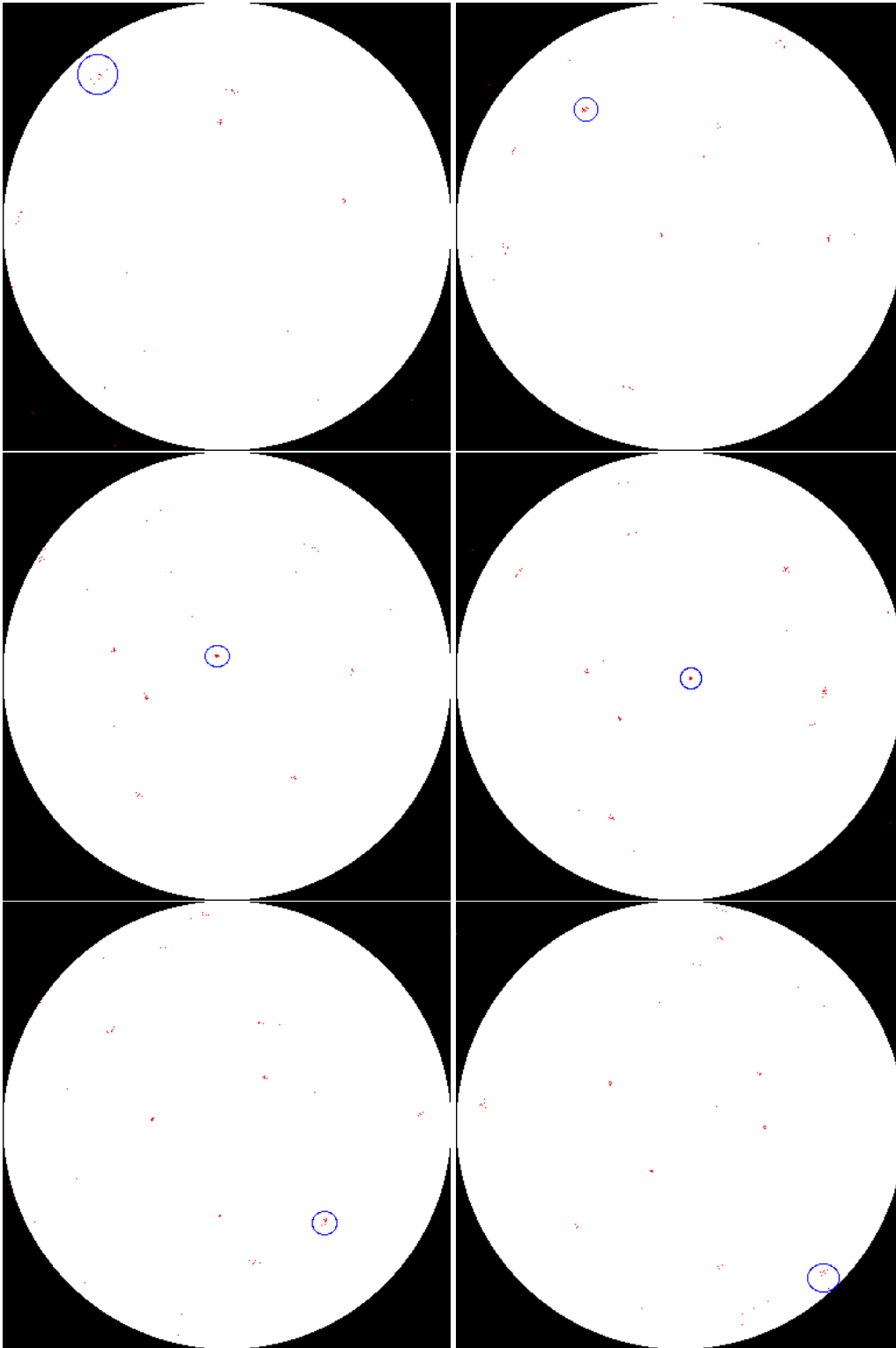
Figure 6.6: Source wandering through the FOV during the scanning process in a simulation of the all-sky survey. Due to the particular shape of the PSF the image of the highlighted source (marked with a blue circle) becomes sharper, when it approaches the center of the detector, whereas at the edge of the FOV the photons are spread over a wider area of pixels. Starting in the upper left corner the pictures are taken at time t_0, $t_0 + 1.75$ s, $t_0 + 6.50$ s, $t_0 + 7.60$ s, $t_0 + 12.35$ s, and $t_0 + 14.90$ s.
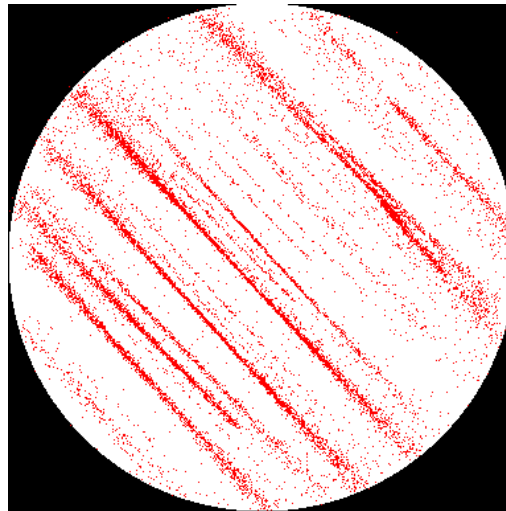
Figure 6.7: Detector image taken with an exposure time of 60 s for several very bright sources. Due to the motion of the telescope axis, the individual sources are smeared as stripes over the entire width of the FOV. Close to the center the PSF has a high accuracy, whereas at the edges the photons are spread over a wide area.

Chapter 7

Conclusion

The eROSITA mission is intended to be an extension of the former ROSAT experiment. Its main destination is a comprehensive source catalog obtained from an all-sky survey of the X-ray sky.

The simulation for eROSITA, which was developed in the course of this work, is a powerful tool for the simulation of individual photon events observed by an X-ray telescope. It provides a possibility to specify individual source properties like a particular spectrum or a light curve for the sources in the RASS-FSC or in the catalog of randomly created sources. The latter are generated according to a flux distribution observed in deep surveys of particular regions of the sky.

The CXRB is simulated by a large number of very faint, discrete X-ray sources. An extension of the program code for the simulation of extended sources is planned as one of the next steps in the development of the simulation. This is necessary, as eROSITA is also intended to discover galaxy clusters, which create diffuse X-ray radiation in major sections of the sky.

In order to obtain the pointing of the telescope's FOV along the satellite's orbit during the all-sky survey, the satellite's motion is calculated by an orbit propagation algorithm developed for this purpose. The algorithm includes second order perturbation theory and is designed for low-earth orbits with a small eccentricity. The achieved accuracy and agreement with real satellite data is sufficient for the simulation.

The measurement process of X-ray photons by the telescope and the resulting detection of single photon events was the main subject of this work. The implementation of this process is based on realistic models, e.g., of the mirror system and the CCD detector. The corresponding technical input data are obtained from files with a standardized format, and can therefore be modified easily, when more precise data for the properties of the individual components will be available in the future.

From the detected events the simulation program creates an event list similar to the measurement data from other X-ray satellites. This list can be evaluated by standard spectral analysis software or can be used as input for the NRTA software. In this way the latter can be tested on simulated measurements of different critical scenarios with, e.g., transient X-ray sources or detector defects. This verification method is necessary, as real satellite data will not be available before the launch of Spectrum-X-Gamma, but the NRTA has to be fully operational at this point of time.

Apart from that purpose the simulation is also applicable for experiments, whether some particularly weak sources will be visible for the telescope, or whether they are overwhelmed by the background radiation. It is possible to study the impact of the motion of the telescope axis on the measured data during the all-sky survey. Due to the finite integration intervals this motion will cause a smearing of the sources in the direction of motion. This effect has to be considered in the image reconstruction, and the necessary mathematical methods for the analysis of these data can be studied by using event lists from the simulation.

So far the basic functions of the telescope can be simulated properly by the program. Light

curves and spectra used as input for simulated observations can be reproduced from the resulting event lists. The implementation of the mirror and the detector model have also been tested separately and seem to work in the right way. Particularly the simulation of the all-sky survey produces realistic output. Thus the program can be regarded as successfully verified, and its output can be used for testing the NRTA.

Of course, there are several aspects in the simulation that can be implemented in more detail. For example, the already mentioned implementation of extended sources is necessary for proper simulations of photons from galaxy clusters or diffuse galactic radiation. This diffuse X-ray radiation may emerge from major sections of the sky, which usually have irregular shapes. Therefore, the description of this kind of sources is much more challenging than the simulation of point sources. The implementation of the diffuse radiation from extended sources is one of the future steps in the further development of the simulation.

Apart from that there are further improvements to make the effects, which have to be considered in the simulation, more realistic. For example, the model of the detector background, which is at the moment implemented by events distributed randomly on the entire detector, can be improved. As the background mainly originates from protons passing the detector shield, the resulting events are usually aligned in stripes on the detector. This particular property will be included in the background model, because it is necessary for testing the background reconstruction algorithms on the output event lists.

To obtain realistic data, it is also necessary to improve especially the implemented model of the PSF. Due to the lack of a proper interpolation algorithm for values between the different available discrete off-axis angles and photon energies, the shape of the PSF as a function of δ and E currently is a step function. Of course, in contrast the real PSF is a continuous function. Therefore, the model has to be upgraded by designing a better interpolation method and by enlarging the number of available off-axis angles and energies with additional PSF simulations.

The image reconstruction itself is an important future step in the development of the NRTA. For this purpose many individual aspects like source smearing due the PSF or the telescope motion, or detector effects due to the RMF, split events, pileup, or background effects have to be considered to obtain a precise image reconstruction from the measured data. Of course, this development can be done by using the simulation as test facility for understanding the impact of these effects on the measurement.

At an advanced stage of in the development there will also be a simulation of an entire all-sky survey. Therefore, the individual aspects of the program have to be improved to obtain more realistic data. As the input of the software is quite flexible, the simulation may be adapted easily, when more precise data about the individual telescope components is available. For example, orbit and attitude data according to the real survey pointing geometry can be used for the simulation of the whole all-sky survey. In order to achieve this compatibility, it is important that the program is designed according to the current standards of HEAsoft.

Due to this flexibility the simulation can be even modified and adapted for different X-ray telescopes than eROSITA. For example, it might also be interesting to simulate measurements of the future satellite Simbol-X. These data could be compared to the existing simulation described by Puccetti et al. (2008), which is based on a different concept. It should be possible to reconstruct the imaging and detection properties like the PSF, the ARF, or the RMF of Simbol-X.

Although many further developments are necessary, with its high degree of flexibility and compatibility the current eROSITA simulation program is a promising basis for comprehensive and detailed simulations of the imaging and measurement process of X-ray telescopes.

Bibliography

Arnaud K., 2008, HEAdas Developer's Guide (v. 1.1), HEASARC, Goddard Space Flight Center, Greenbelt, USA

Aschenbach B., Hahn H.M., Trümper J., Jenkner H., 1998, The Invisible Sky, ROSAT and the Age of X-Ray Astronomy, Springer-Verlag New York

Bate R., Mueller D., White J., 1971, Fundamentals of astrodynamics, Dover Publications, New York

Benlloch S., Wilms J., Edelson R., et al., 2001, The Astrophysical Journal 562, L121

Bernlöhr K., Carrol O., Cornils R., et al., 2003, Astroparticle Physics 20, 111

Borkowski J., 2002, Parameter Interface Library Users Manual (v. 1.8.5), INTEGRAL Science Data Centre, Versoix, Switzerland

Brandt W.N., Hasinger G., 2005, Annual Review of Astronomy & Astrophysics 43, 827

Brouwer D., 1959, The Astronomical Journal 64, 378

Carroll B.W., Ostlie D.A., 1996, An introduction to modern astrophysics, Addison-Wesley

Charles P.A., Seward F.D., 1995, Exploring the X-ray universe, Cambridge, New York: Cambridge University Press

Davis J.E., 2001a, The Astrophysical Journal 562, 575

Davis J.E., 2001b, The Astrophysical Journal 548, 1010

Deák I., 1990, Random Number Generators and Simulation, Mathematical Methods of Operations Research 4, Akadémiai Kiadó, Budapest

Dijkstra E.W., 1968, Communications of the ACM 11, 147

Dmitriev G., Hasinger G., Parmar A., et al., 2005, SPECTRUM-RG/eROSITA/LOBSTER MISSION DEFINITION DOCUMENT, Technical report, Roscosmos, ESA, IKI, MPE, University of Leicester

Ehle M., Breitfellner M., Díaz Trigo M., et al., 2007, XMM-Newton Users' Handbook (v. 2.5)

Escobal P.R., 1965, Methods of orbit determination, Wiley, New York, London, Sydney

Fiorucci G., Bourquin J.P., Bovet D., et al., 1990, Nuclear Instruments and Methods in Physics Research A 292, 141

Flury W., 1991, Vorlesung Raumfahrtmechanik, Lecture, Technische Hochschule Darmstadt

Friedrich P., 2008, In: Ringberg eROSITA and high-energy groups meeting., Garching, Germany

Fürmetz M., 2007, diploma thesis, MPE, TU München, Garching, Germany

Fürmetz M., Friedrich P., 2008, In: Ringberg eROSITA and high-energy groups meeting., Garching, Germany

George I.M., Arnaud K.A., Ruamsuwan B.P.L., Corcoran M.F., 1998, The Calibration Requirements for Spectral Analysis, HEASARC, Greenbelt, USA

George I.M., Rots A., Mukai K., 1994, Guidelines for defining FITS formats for event lists, NASA, HEASARC, Goddard Space Flight Center, Greenbelt, USA

Giacconi R., Gursky H., Paolini F.R., Rossi B.B., 1962, Physical Review Letters 9, 439

Gould H., Tobochnik J., Christian W., 2006, An introduction to computer simulation methods: Applications to Physical Systems (third edition), Addison-Wesley

Groeneveld H.A., 1999, Design, Simulation und Optimierung kodierter Aperturen, Ph.D. thesis

Guainazzi M., 2008, EPIC status of calibration and data analysis (v. 2.7), ESA

Hanisch R.J., Farris A., Greisen E.W., et al., 2001, Astronomy and Astrophysics 376, 359

Hasinger G., 2008, In: Ringberg eROSITA and high-energy groups meeting., Garching, Germany

HEASARC 2007, CFITSIO User's Reference Guide (v. 3.0), HEASARC, Greenbelt, USA

Henrard J., 1974, Celestial Mechanics 10, 437

Hoots F.R., 1981, Celestial Mechanics 24, 367

Jansen F., Lumb D., Altieri B., et al., 2001, Astronomy and Astrophysics 365, L1

Keller H., 2002, Untersuchung spezieller geometrischer Größen zum Aufbau von Intersatellitenverbindungen, Ph.D. thesis

Klinkrad H.H., 1983, Analytische Berechnung erdnaher Satellitenbahnen unter Verwendung eines realistischen Luftwiderstandsmodells, Ph.D. thesis

Kozai Y., 1959, The Astronomical Journal 64, 367

Liu J.J.F., 1974, AIAA Journal 12, 1511

Liu J.J.F., Alford R.L., 1979, In: Olson W.P., Pfitzer K.A. (eds.) AIAA, Aerospace Sciences Meeting.

Lyddane R.H., 1963, The Astronomical Journal 68, 555

Marshall F.E., Boldt E.A., Holt S.S., et al., 1980, Astrophysical Journal 235, 4

Martin M., 2004, Eigenschaften von Detektoren für den schnellen Auslesekanal auf XEUS

Meeus J., 1998, Astronomical algorithms, Astronomical algorithms (2nd ed.) by J. Meeus. Richmond, VA: Willmann-Bell, 1998.

Meidinger N., 2008, In: Ringberg eROSITA and high-energy groups meeting., Garching, Germany

Meidinger N., Andritschke R., Hälker O., et al., 2007, In: Siegmund O.H. (ed.) UV, X-Ray, and Gamma-Ray Space Instrumentation for Astronomy XV, SPIE Volume 6686, 0H - 0H-10.

Mitsuda K., Bautz M., Inoue H., et al., 2007, Publications of the Astronomical Society of Japan 59, 1

MPE, IAAT, FAU, et al., 2007, Beteiligung der FAU Erlangen-Nürnberg an eROSITA für die Spectrum Roentgen-Gamma Mission, Proposal

Petry D., The MAGIC Telescope Collaboration 1999, Astronomy and Astrophysics Supplement 138, 601

Predehl P., 2008a, eROSITA CCD module requirements, Technical report, MPE, Garching, Germany

Predehl P., 2008b, In: Ringberg eROSITA and high-energy groups meeting., Garching, Germany

Predehl P., Andritschke R., Bornemann W., et al., 2007, In: Siegmund O.H. (ed.) UV, X-Ray, and Gamma-Ray Space Instrumentation for Astronomy XV, SPIE Volume 6686, 17 - 17-9.

Predehl P., Hasinger G., Böhringer H., et al., 2006, In: Turner M.J.L., Hasinger G. (eds.) Space Telescopes and Instrumentation II: Ultraviolet to Gamma Ray, SPIE Volume 6266, 0P.

Puccetti S., Piconcelli E., Giommi P., Fiore F., 2008, Cookbook for the ASDC Simbol-X data simulator, Technical report, ASDC, Frascati, Italy

Redfern D., Bartram J.F., 1995, Acoustical Society of America Journal 98, 21

Schroeder D.J., 2000, Astronomical optics (second edition), Academic Press, San Diego

Squires G., Kaiser N., Babul A., et al., 1996, Astrophysical Journal 461, 572

Steiner W., Schagerl M., 2004, Raumflugmechanik, Springer, Heidelberg, Berlin

Strüder L., Briel U., Dennerl K., et al., 2001, Astronomy and Astrophysics 365, L18

Timmer J., König M., 1995, Astronomy and Astrophysics 300, 707

Uttley P., McHardy I.M., 2001, Monthly Notices of the Royal Astronomical Society 323, L26

Voges W., Aschenbach B., Boller T., et al., 2000, VizieR Online Data Catalog 9029

Walter U., 2007, Raumfahrttechnik, Lecture, TU München

Weisskopf M.C., Tananbaum H.D., Van Speybroeck L.P., O'Dell S.L., 2000, In: Truemper J.E., Aschenbach B. (eds.) Proc. SPIE Vol. 4012, 2-16, X-Ray Optics, Instruments, and Missions III, Vol. 4012., p.2

Wilms J., 2002, Ph.D. thesis, Universität Tübingen

Wilms J., 2006, Active Galactic Nuclei, Lecture, Dr. Remeis-Sternwarte Bamberg (Astronomical Institute of the University of Erlangen-Nuremberg), Bamberg

Wilms J., 2008, X-ray Astronomy I, Lecture, Dr. Remeis-Sternwarte Bamberg (Astronomical Institute of the University of Erlangen-Nuremberg), Bamberg

Wilms J., Kreykenbohm I., 2008, In: Ringberg eROSITA and high-energy groups meeting., Bamberg

Wolter H., 1952, Annalen der Physik 445, 94

Appendix A

Orbit perturbations

To calculate a close Earth satellite's orbit according to second order perturbation theory (Eqs. (5.82) and (5.83)), the explicit form of the contributions $\dot{q}\left(\{\bar{q}\}\right)$ and $\Delta q\left(\{\bar{q}\}\right)$ for the orbital elements $q \in \{a, i, \Omega, h, k, u'\}$ has to be known. Unfortunately most references dealing with second order perturbation theory (e.g., Flury 1991, Klinkrad 1983, Liu 1974 or Liu & Alford 1979), use Keplerian orbital elements $q \in (a, e, i, \Omega, \omega, M)$. Additionally the formulas in some of these references contain typos, which may have emerged from the lengthy mathematical expressions for $\dot{q}\left(\{\bar{q}\}\right)$ and $\Delta q\left(\{\bar{q}\}\right)$, thus it is difficult to find a reliable source for the necessary perturbation terms.

In the following an overview over the perturbation contributions for the transformed parameter set (a, i, Ω, h, k, u') is given, with $h, k,$ and u' defined by equations (5.85), (5.86) and (5.87) respectively. The mathematical expressions have been summarized from the references mentioned above. Several typos found in the sources have been eliminated. Because of the lengthy expressions most calculations have been performed with *Maple* (Redfern & Bartram, 1995). But as *Maple* uses some inconvenient geometrical transformations during the calculation, some results had to be modified afterwards in order to achieve a better computer performance for running the implemented orbit propagation algorithm. Finally the code was tested according to different verification procedures (see Sec. 5.4), but still there is no guarantee for the correctness of the different mathematical expressions. Almost all available references contain more or less discrepancies, so there is no absolutely reliable source.

As the perturbation terms $\dot{q}$ and Δq are given in terms of Keplerian orbital elements (a, e, i, Ω, f), a transformation from the system (a, i, Ω, h, k, u') to Keplerian orbital elements has to be performed before the iteration steps (5.82) and (5.83), in order to be able to calculate the changes of the low-eccentricity orbit parameters a, i, Ω, h, k, u'. That means, in order to be independent of the Keplerian coordinates and to avoid this transformation, the formulas in the following sections A.1 and A.2 have to be rewritten in the new parameter space. The computational effort for the transformation between the different parameter systems is negligible in comparison to the computation of $\dot{q}$ and Δq. Therefore, the explicit mathematical transformation of equations (A.4) to (A.28) was not performed in this work.

A.1 Secular and long period

The following contributions $\dot{q}\left(\{\bar{q}\}\right)$ describe the long term evolution of the satellite's orbit (secular and long period changes) in second order perturbation theory. In Flury (1991), Klinkrad (1983), Liu (1974) or Liu & Alford (1979)) one can find these perturbations on the set of Keplerian orbital elements. The simulation deals with the modified parameter set presented in Sec. 5.2.10 in order

to avoid divergencies, so some transformations have been applied using *Maple*:

$$\dot{h} = \dot{e}\cos\omega - e\sin\omega\,\dot{\omega} \tag{A.1}$$

$$\dot{k} = \dot{e}\sin\omega + e\cos\omega\,\dot{\omega} \tag{A.2}$$

$$\dot{u}' = \dot{\omega} + \dot{M} \tag{A.3}$$

The contributions $\dot{e}$, $\dot{\omega}$, and $\dot{M}$ can be obtained from the given literature. The possibly divergent terms, which are the J_3 contributions, have been summarized in such a way, that there are no infinities throughout the numerical calculation of the perturbations:

$$\dot{a} = 0 \tag{A.4}$$

$$
\begin{aligned}
\dot{i} = {}& \frac{3}{64}nJ_2^2\left(\frac{R_e}{p}\right)^4 \sin(2i)\left(14 - 15\sin^2 i\right)e^2\sin(2\omega) \\
& + \frac{3}{8}nJ_3\left(\frac{R_e}{p}\right)^3 \cos i\left(4 - 5\sin^2 i\right)e\cos\omega \\
& + \frac{15}{64}nJ_4\left(\frac{R_e}{p}\right)^4 \sin(2i)\left(6 - 7\sin^2 i\right)e^2\sin(2\omega)
\end{aligned} \tag{A.5}
$$

$$
\begin{aligned}
\dot{\Omega} = {}& -\frac{3}{2}nJ_2\left(\frac{R_e}{p}\right)^2 \cos i \\
& -\frac{3}{2}nJ_2^2\left(\frac{R_e}{p}\right)^4 \cos i\left[\frac{9}{4} + \frac{3}{2}\sqrt{1-e^2} - \sin^2 i\left(\frac{5}{2} + \frac{9}{4}\sqrt{1-e^2}\right)\right. \\
& \left. + \frac{e^2}{16}\left(4 + 5\sin^2 i\right) - \frac{e^2}{8}\left(7 - 15\sin^2 i\right)\cos(2\omega)\right] \\
& -\frac{3}{8}nJ_3\left(\frac{R_e}{p}\right)^3 \left(4 - 5\sin^2 i\right)\frac{e}{\tan i}\sin\omega \\
& + \frac{15}{16}nJ_4\left(\frac{R_e}{p}\right)^4 \cos i\left[\left(4 - 7\sin^2 i\right)\left(1 + \frac{3}{2}e^2\right) - \left(3 - 7\sin^2 i\right)e^2\cos(2\omega)\right]
\end{aligned} \tag{A.6}
$$

$$\dot{h} = (\dot{e})_{J_2+J_4}\cos\omega - e\sin\omega\,(\dot{\omega})_{J_2+J_4} + \left(\dot{h}\right)_{J_3} \tag{A.7}$$

$$\dot{k} = (\dot{e})_{J_2+J_4}\sin\omega + e\cos\omega\,(\dot{\omega})_{J_2+J_4} + \left(\dot{k}\right)_{J_3} \tag{A.8}$$

$$\dot{u}' = (\dot{\omega})_{J_2+J_4} + \left(\dot{M}\right)_{J_2+J_4} + \left(\dot{u}'\right)_{J_3} \tag{A.9}$$

with

$$
\begin{aligned}
(\dot{e})_{J_2+J_4} = {}& -\frac{3}{32}nJ_2^2\left(\frac{R_e}{p}\right)^4 \sin^2 i\left(14 - 15\sin^2 i\right)e\left(1 - e^2\right)\sin(2\omega) \\
& -\frac{15}{32}nJ_4\left(\frac{R_e}{p}\right)^4 \sin^2 i\left(6 - 7\sin^2 i\right)e\left(1 - e^2\right)\sin(2\omega)
\end{aligned} \tag{A.10}
$$

$$(\dot{\omega})_{J_2+J_4} = \frac{3}{4}nJ_2\left(\frac{R_e}{p}\right)^2\left(4-5\sin^2 i\right)$$

$$+ \frac{3}{16}nJ_2^2\left(\frac{R_e}{p}\right)^4\left[48-103\sin^2 i+\frac{215}{4}\sin^4 i+\left(7-\frac{9}{2}\sin^2 i-\frac{45}{8}\sin^4 i\right)e^2\right.$$

$$+ 6\sqrt{1-e^2}\left(1-\frac{3}{2}\sin^2 i\right)\left(4-5\sin^2 i\right)$$

$$\left.- \frac{1}{4}\left(2\left(14-15\sin^2 i\right)\sin^2 i-\left(28-158\sin^2 i+135\sin^4 i\right)e^2\right)\cos(2\omega)\right]$$

$$- \frac{15}{32}nJ_4\left(\frac{R_e}{p}\right)^4\left[16-62\sin^2 i+49\sin^4 i+\frac{3}{4}\left(24-84\sin^2 i+63\sin^4 i\right)e^2\right.$$

$$\left.+ \left(\sin^2 i\left(6-7\sin^2 i\right)-\frac{1}{2}\left(12-70\sin^2 i+63\sin^4 i\right)e^2\right)\cos(2\omega)\right]$$

(A.11)

$$\left(\dot{M}\right)_{J_2+J_4} = n\left[1+\frac{3}{2}J_2\left(\frac{R_e}{p}\right)^2\left(1-\frac{3}{2}\sin^2 i\right)\sqrt{1-e^2}\right]$$

$$+ \frac{3}{2}nJ_2^2\left(\frac{R_e}{p}\right)^4\left[\left(1-\frac{3}{2}\sin^2 i\right)^2\left(1-e^2\right)+\left(\frac{5}{4}\left(1-\frac{5}{2}\sin^2 i+\frac{13}{8}\sin^4 i\right)\right.\right.$$

$$+ \frac{5}{8}\left(1-\sin^2 i+\frac{5}{8}\sin^4 i\right)e^2+\frac{1}{16}\sin^2 i\left(14-15\sin^2 i\right)\left(1-\frac{5}{2}e^2\right)\cos(2\omega)\right)\sqrt{1-e^2}$$

$$+ \frac{1}{4}\left\{3\left(3-\frac{15}{2}\sin^2 i+\frac{47}{8}\sin^4 i+\left(\frac{3}{2}-5\sin^2 i+\frac{117}{6}\sin^4 i\right)e^2-\frac{1}{8}\left(1+5\sin^2 i\right.\right.\right.$$

$$\left.- \frac{101}{8}\sin^4 i\right)e^4\right)+\frac{e^2}{8}\sin^2 i\left(70-123\sin^2 i+\left(56-66\sin^2 i\right)e^2\right)\cos(2\omega)$$

$$\left.\left.+ \frac{27}{128}e^4\sin^4 i\cos(4\omega)\right\}\frac{1}{\sqrt{1-e^2}}\right]$$

(A.12)

$$\left(\dot{h}\right)_{J_3} = (\dot{e})_{J_3}\cos\omega-e\sin\omega\,(\dot{\omega})_{J_3}$$

$$= -\frac{3}{8}nJ_3\left(\frac{R_e}{p}\right)^3\frac{1}{\sin i}\left[-1-4e^2+35e^2\cos^2 i+6\cos^2 i+5e^2\cos^2(\omega)\right.$$

(A.13)

$$\left.- 41e^2\cos^2(\omega)\cos^2 i+40e^2\cos^2(\omega)\cos^4 i-35e^2\cos^4 i-5\cos^4 i\right]$$

$$\left(\dot{k}\right)_{J_3} = (\dot{e})_{J_3}\sin\omega+e\cos\omega\,(\dot{\omega})_{J_3}$$

$$= -\frac{3}{8}nJ_3\left(\frac{R_e}{p}\right)^3\frac{1}{\sin i}\cos(\omega)\sin(\omega)\left(5-41\cos^2 i+40\cos^4 i\right)e^2$$

(A.14)

$$\left(\dot{u}'\right)_{J_3} = (\dot{\omega})_{J_3}+\left(\dot{M}\right)_{J_3}$$

$$= -\frac{3}{8}nJ_3\left(\frac{R_e}{p}\right)^3\frac{\sin\omega}{e\sin i}\left[1-\sqrt{1-e^2}+4\sqrt{1-e^2}e^2+4e^2+\cos^2 i\left(-6+6\sqrt{1-e^2}\right.\right.$$

$$\left.\left.- 35e^2-24e^2\sqrt{1-e^2}\right)+\cos^4 i\left(35e^2+5-5\sqrt{1-e^2}+20\sqrt{1-e^2}e^2\right)\right]$$

(A.15)

A.2 Short period

In addition to the long term contributions to the changes of the orbital elements there are also short period variations depending on the position of the satellite on its orbit, i.e., basically on the true anomaly f. Like the long term contributions they are given in terms of Keplerian orbital elements according to Flury (1991), Klinkrad (1983), Liu & Alford (1979). The same transformations have been applied as for the secular and long periodic contributions.

$$\Delta a = + J_2 a \left(\frac{R_e}{a}\right)^2 \left[\left(\frac{a}{r}\right)^3 \left(1 - \frac{3}{2}\sin^2 i + \frac{3}{2}\sin^2 i \cos(2\omega + 2\theta)\right) - \left(1 - \frac{3}{2}\sin^2 i\right)\left(1 - e^2\right)^{-3/2}\right]$$
(A.16)

$$\Delta i = + \frac{3}{8} J_2 \left(\frac{R_e}{p}\right)^2 \sin(2i)\left[e\cos(2\omega + \theta) + \cos(2\omega + 2\theta) + \frac{e}{3}\cos(2\omega + 3\theta)\right]$$
(A.17)

$$\Delta\Omega = - \frac{3}{2} J_2 \left(\frac{R_e}{p}\right)^2 \cos i \left[\theta - M + e\sin\theta - \frac{e}{2}\sin(2\omega + \theta) - \frac{1}{2}\sin(2\omega + 2\theta)\right.$$
(A.18)

$$\left. - \frac{e}{6}\sin(2\omega + 3\theta)\right]$$
(A.19)

$$\Delta h = (\Delta e)_{\text{finite}}\cos\omega - e\sin\omega\,(\Delta\omega)_{\text{finite}} + (\Delta h)_0$$
(A.20)

$$\Delta k = (\Delta e)_{\text{finite}}\sin\omega + e\cos\omega\,(\Delta\omega)_{\text{finite}} + (\Delta k)_0$$
(A.21)

$$\Delta u' = (\Delta\omega)_{\text{finite}} + (\Delta M)_{\text{finite}} + (\Delta u')_0$$
(A.22)

with

$$(\Delta e)_{\text{finite}} = \frac{1}{2} J_2 \left(\frac{R_e}{p}\right)^2 \left(1 - \frac{3}{2}\sin^2 i\right)\left[\frac{3}{2}e + 3\left(1 + \frac{e^2}{4}\right)\cos\theta + \frac{3}{2}e\cos(2\theta)\frac{e^2}{4}\cos(3\theta)\right]$$

$$+ \frac{3}{8} J_2 \left(\frac{R_e}{p}\right)^2 \sin^2 i \left[\left(1 + \frac{11}{4}e^2\right)\cos(2\omega + \theta) + \frac{e^2}{4}\cos(2\omega - f) + 5e\cos(2\omega + 2\theta)\right.$$

$$\left. + \frac{1}{3}\left(7 + \frac{17}{4}e^2\right)\cos(2\omega + 3\theta) + \frac{3}{2}e\cos(2\omega + 4\theta) + \frac{e^2}{4}\cos(2\omega + 5\theta) + \frac{3}{2}e\cos(2\omega)\right]$$

(A.23)

$$(\Delta\omega)_{\text{finite}} = \frac{3}{4} J_2 \left(\frac{R_e}{p}\right)^2 \left[\left(4 - 5\sin^2 i\right)\left(\theta - M + e\sin\theta\right) - \frac{3}{4}\sin^2 i \sin(2\omega)\right]$$

$$+ \frac{3}{2} J_2 \left(\frac{R_e}{p}\right)^2 \left(1 - \frac{3}{2}\sin^2 i\right)\left[\frac{e}{4}\sin\theta + \frac{1}{2}\sin(2\theta) + \frac{1}{12}e\sin(3\theta)\right.$$

$$- \frac{e}{2}\left(1 - \frac{15}{8}\sin^2 i\right)\sin(2\omega + \theta) - \frac{e^2}{16}\sin^2 i \sin(2\omega - f)$$

$$- \frac{1}{2}\left(1 - \frac{5}{2}\sin^2 i\right)\sin(2\omega + 2\theta) - \frac{e}{6}\left(1 - \frac{19}{8}\sin^2 i\right)\sin(2\omega + 3\theta)$$

$$\left. + \frac{3}{8}\sin^2 i \sin(2\omega + 4\theta) + \frac{e}{16}\sin^2 i \sin(2\omega + 5\theta)\right]$$
(A.24)

$$(\Delta M)_{\text{finite}} = -\frac{3}{2}J_2\left(\frac{R_e}{p}\right)^2 \sqrt{1-e^2}\left[\left(1-\frac{3}{2}\sin^2 i\right)\left(-\frac{e}{4}\sin\theta + \frac{1}{2}\sin(2\theta) + \frac{e}{12}\sin(3\theta)\right)\right.$$

$$+ \frac{1}{2}\sin^2 i\left(-\frac{5}{8}e\sin(2\omega+\theta) - \frac{e}{8}\sin(2\omega-\theta) - \frac{7}{168}e\sin(2\omega+3\theta)\right. \tag{A.25}$$

$$\left.\left. + \frac{3}{4}\sin(2\omega+4\theta) + \frac{e}{8}\sin(2\omega+5\theta)\right) - \frac{3}{8}\sin^2 i\sin(2\omega)\right]$$

$$(\Delta h)_0 = \frac{1}{4e}J_2\left(\frac{R_e}{p}\right)^2\left[\left(1-3\cos^2 i\right)\left(-1+\left(1-e^2\right)^{3/2}\right)\cos\omega\right.$$

$$+ \frac{e}{2}\sin\omega\left(12\left(1-3\cos^2 i\right)\sin\theta + 6\left(1-\cos^2 i\right)\sin(2\omega+\theta)\right. \tag{A.26}$$

$$\left.\left. - 14\left(1-\cos^2 i\right)\sin(2\omega+3\theta)\right)\right]$$

$$(\Delta k)_0 = -\frac{1}{4e}J_2\left(\frac{R_e}{p}\right)^2\left[\left(1-3\cos^2 i\right)\left(1-\left(1-e^2\right)^{3/2}\right)\sin\omega\right.$$

$$+ \frac{e}{2}\cos\omega\left(12\left(1-3\cos^2 i\right)\sin\theta + 6\left(1-\cos^2 i\right)\sin(2\omega+\theta)\right. \tag{A.27}$$

$$\left.\left. - 14\left(1-\cos^2 i\right)\sin(2\omega+3\theta)\right)\right]$$

$$(\Delta u')_0 = -\frac{1}{8e}J_2\left(\frac{R_e}{p}\right)^2\left(1-\sqrt{1-e^2}\right)$$

$$\left[\left(6-18\cos^2 i\right)\sin\theta - \left(1-\cos^2 i\right)\left(3\sin(2\omega+\theta) + 7\sin(2\omega+3\theta)\right)\right] \tag{A.28}$$

To evaluate these expressions, the mean local radius r and the true anomaly θ can be determined according to equations (5.21), (5.24) and (5.29) using the following low-eccentricity approximation for E according to Flury (1991) p. 80:

$$E = M + \left(e + \frac{e^3}{8}\right)\sin M + \frac{e^2}{2}\sin(2M) + \frac{3}{8}e^3\sin(3M) + O(e^4) \tag{A.29}$$

In contrary to the Kepler equation (5.28) this formula gives a numerically less expensive estimation, which is sufficient for the current purpose.

Acknowledgments

List of acronyms

AGN	**A**ctive **G**alactic **N**uclei
AIP	**A**strophysical **I**nstitute **P**otsdam
ARF	**A**ncillary **R**esponse **F**ile
CXRB	**C**osmic **X**-**R**ay **B**ackground
DUO	**D**ark **U**niverse **O**bservatory
EPIC	**E**uropean **P**hoton **I**maging **C**amera
eROSITA	**e**xtended **RO**entgen **S**urvey with an **I**maging **T**elescope **A**rray
FFT	**F**ast **F**ourier **T**ransformation
FITS	**F**lexible **I**mage **T**ransport **S**ystem
FOV	**F**ield **O**f **V**iew
FSC	**F**aint **S**ource **C**atalog
FWHM	**F**ull **W**idth at **H**alf **M**aximum
GSL	**G**NU **S**cientific **L**ibrary
HDU	**H**eader and **D**ata **U**nit
HEAdas	**H**igh **E**nergy **A**stronomy **d**ata **a**nalysis **s**ystem
HEASARC	**H**igh **E**nergy **A**strophysics **S**cience **A**rchive **R**esearch **C**enter
HEAsoft	**H**igh **E**nergy **A**stronomy **s**oftware
H.E.S.S.	**H**igh **E**nergy **S**tereoscopic **S**ystem
IAAT	**I**nstitute for **A**stronomy and **A**strophysics **T**übingen
IDL	**I**nteractive **D**ata **L**anguage
ISDC	**I**NTEGRAL **S**cience **D**ata **C**entre
ISIS	**I**nteractive **S**pectral **I**nterpretation **S**ystem
MAGIC	**M**ajor **A**tmospheric **G**amma-Ray **I**maging **C**erenkov
MPE	**M**ax-**P**lanck-Institut für **E**xtraterrestrische Physik
NRTA	**N**ear **R**eal **T**ime data **A**nalysis
PHA	**P**ulse **H**eight **A**mplitude
PIL	**P**arameter **I**nterface **L**ibrary
PSD	**P**ower **S**pectral **D**ensity
PSF	**P**oint **S**pread **F**unction
RASS	**R**OSAT **A**ll-**S**ky **S**urvey
rms	**r**oot **m**ean **s**quare
ROSAT	**RO**entgen **SAT**ellite
RMF	**R**edistribution **M**atrix **F**ile
RXTE	**R**ossi **X**-ray **T**iming **E**xplorer
SASS	**S**cience **A**nalysis **S**oftware **S**ystem
TLE	**T**wo **L**ine **E**lement
XMM-Newton	**X**-ray **M**ulti-**M**irror Mission **Newton**

List of Figures

List of Tables